Heat transfer and interfacial flow physics of microgravity flow boiling in single-side-heated rectangular channel with subcooled inlet conditions – Experiments onboard the International Space Station

Issam Mudawar[a,*], V.S. Devahdhanush[a], Steven J. Darges[a],

Mohammad M. Hasan[b], Henry K. Nahra[b], R. Balasubramaniam[c], Jeffrey R. Mackey[d]

[a] Purdue University Boiling and Two-Phase Flow Laboratory (PU-BTPFL), School of Mechanical Engineering, Purdue University, 585 Purdue Mall, West Lafayette, IN 47907, USA

[b] NASA Glenn Research Center, 21000 Brookpark Road, Cleveland, OH 44135, USA

[c] Case Western Reserve University, 10900 Euclid Ave., Cleveland, OH 44106, USA

[d] HX5, LLC 3000 Aerospace Parkway, Brookpark, OH 44142, USA

Abstract – This study is the culmination of a long-term collaborative effort between researchers from the Purdue University Boiling and Two-Phase Flow Laboratory (PU-BTPFL) and the NASA Glenn Research Center to investigate gravitational effects on flow boiling and flow condensation. The science and design concepts for this large-scale effort were initiated in 2011 and included several studies detailing various aspects of two-phase fluid physics in both Earth gravity and microgravity, culminating in construction of the large-scale experimental facility named "Flow Boiling and Condensation Experiment (FBCE)". The experiment was launched to the International Space Station (ISS) in August 2021. Following the successful installation of FBCE, equipped with the Flow Boiling Module (FBM), onboard the ISS and completion of several safety checks, flow boiling experiments were performed for five months from February 2022 until July 2022. This resulted in a large flow boiling database covering broad ranges of operating parameters and heating configurations spanning several research objectives. This study investigates microgravity flow boiling of n-perfluorohexane with subcooled inlet in a single-side-heated rectangular channel of dimensions 114.6-mm heated length, 2.5-mm heated width, and 5.0-mm height. Key operating parameters investigated are mass velocity (199.90 – 3200.13 kg/m^{2}s), inlet subcooling (0.10 – 45.76°C), and inlet pressure (113.30 – 164.29 kPa). Images and image sequences acquired via high-speed-video are presented to elucidate the interfacial flow physics. To analyze and explain the effects of various parameters in microgravity, heat transfer results are presented as flow boiling curves, streamwise profiles of wall temperature and heat transfer coefficient, and parametric trends of local and averaged heat transfer coefficient. Mass velocity and inlet subcooling significantly influenced most of the aforementioned aspects of flow boiling, whereas effects of inlet pressure were comparatively insignificant. Although the data and observed flow physics might be different, the parametric effects and trends in microgravity are similar to vertical upflow in Earth gravity. Some cases, especially low mass velocities, high heat fluxes, and large degrees of inlet subcooling, experienced temporally anomalous flow behaviors caused by

two-phase flow instabilities manifesting as flow reversals and resulted in deviations in overall trends. Severe thermodynamic non-equilibrium is observed throughout the channel. Overall, FBCE's ISS experiments were successful for subcooled inlet with single-sided heating of rectangular channel, and the collected data well established the various effects on flow boiling physics in highly controlled long-term microgravity conditions.

Keywords: flow boiling; two-phase heat transfer coefficient; high-speed photography; subcooled; microgravity; single-sided heating; International Space Station

* Author to whom correspondence should be addressed; Tel. (765) 494-5705; Fax (765) 494-0539; E-mail: *mudawar@ecn.purdue.edu;* Website: *https://engineering.purdue.edu/BTPFL*

Nomenclature

A	area
A_c	cross-sectional area
Co	confinement number
D_h	hydraulic diameter
G	mass velocity
g	gravitational acceleration
g_e	gravitational acceleration on Earth
μg_e	microgravity
H	height of channel's cross section
H_{tc}	conduction distance through heating strip
h	enthalpy; heat transfer coefficient
$\overline{h}$	average heat transfer coefficient
h_{fg}	latent heat of vaporization
k	thermal conductivity
L_d	upstream development length
L_e	downstream exit length
L_h	heated length
$\dot{m}$	mass flow rate
N_z	number of streamwise measurement locations
P_h	heated perimeter
p	pressure
q''	heat flux
q''_{CHF}	critical heat flux

q''_{ONB}	heat flux corresponding to ONB
q''_{ONBD}	heat flux corresponding to ONBD
T	temperature
$\overline{T}$	average temperature
ΔT_{sub}	fluid subcooling, $\Delta T_{sub} = T_{sat} - T_f$
t	time
W	width of channel's cross section
x_e	thermodynamic equilibrium quality
z	streamwise coordinate

Greek symbols

ρ	density
σ	surface tension

Subscripts

a	denotes wall 1 or 2 (= 1 or 2)
f	liquid; bulk fluid
g	vapor
h	heated
in	inlet to channel heated section
out	outlet of channel heated section
s	solid
sat	saturation
sp	single-phase
sub	subcooling
tc	thermocouple in heating strip
w	wall
wa	wall 1 or 2 (= $w1$ or $w2$)
$xe=0$	corresponding to the location where $x_e = 0$
z	local (along streamwise direction)

Acronyms

BHM	Bulk Heater Module
CHF	Critical Heat Flux
DC	Direct Current
FBCE	Flow Boiling and Condensation Experiment

FBM	Flow Boiling Module
FDB	Fully Developed Boiling
FIR	Fluid Integrated Rack
FSML	Fluids System Module – Lower
FSMU	Fluids System Module – Upper
GRC	NASA's Glenn Research Center
ISS	International Space Station
ITCS	ISS Thermal Control System
MST	Mission Sequence Testing
nPFH	n-Perfluorohexane
NVG	Net Vapor Generation
ONB	Onset of Nucleate Boiling
ONBD	Onset of Nucleate Boiling Degradation
PDB	Partially Developed Boiling
RDAQM1	Remote Data Acquisition Module 1
RDAQM2	Remote Data Acquisition Module 2
RTD	Resistance Temperature Detector
TMA	Test Module Assembly
VES	Vacuum Exhaust System

1. Introduction

1.1 Two-phase Flow and Heat Transfer in Space and Aircraft Applications

Thermal management is essential for the safe and reliable operation of any system generating heat. Several space and aircraft agencies around the world, including NASA, are both pursuing numerous manned and unmanned space missions, which are meant for significantly longer distances and durations, and developing more advanced aircraft. These new developments are significantly more powerful than the existing systems and have greater weight restrictions for increased performance and efficiency. Presently, thermal management of most systems and components used in these applications are based on forced liquid convection. With the new developments comes the need for more advanced thermal management systems that augment heat dissipation rates, while making the system more compact and lightweight. Two-phase schemes utilizing boiling and condensation are prime contenders for these applications, due to their ability to dissipate large amounts of heat while keeping the system at low temperatures, due to very high heat transfer coefficients an order or more in magnitude over single-phase schemes.

Over the past few decades, researchers at the Purdue University Boiling and Two-Phase Flow Laboratory (PU-BTPFL) and many other groups around the world have investigated and advanced the frontiers of this field by implementing phase transition in a variety of schemes including boiling in capillary flows [1], pool boiling [2], flow boiling in macro-channels [3,4], micro-channels [5,6], and annuli [7], jet impingement [8,9] and sprays [10]. The choice of boiling schemes for applications are based on their many inherent advantages, while also considering their limitations. Of these schemes, the prime choice for space and aircraft applications is channel flow boiling that depends on flow inertia to flush the produced vapor out of the heated section and replenish the walls with fresh liquid, while requiring a relatively low pumping power. Moreover, channel flow boiling is relatively less complex to implement and has the potential to cool multiple devices in series in a fully closed flow loop.

More specifically, a recent NASA report [11] recommends boiling schemes for the safe operation of high-power-density energy conversion equipment, avionics, Rankine-power-cycle-based Fission Power Systems (FPS), and onboard life support systems.

1.2 Gravitational Field Effects on Two-phase Flow and Heat Transfer

The range of gravitational accelerations and body-force-induced acceleration (>1 g_e) that are important for studying two-phase flow and heat transfer in space and aircraft applications is shown in Fig. 1, with several specific examples. While most two-phase flow and heat transfer physics are well understood in Earth gravity, these understandings are limited and not well established in other gravitational environments. The significantly different gravitational fields impact the flow boiling physics to a large extent, rendering the various existing design tools, which were developed using Earth-gravity data, unreliable in predicting the flow regime, heat transfer performance, *etc.*

Researchers have made several efforts to study the effects of gravity (especially reduced gravity) via six primary experimental avenues: (i) Earth-gravity experiments conducted at different flow orientations and (ii) microgravity experiments using drop towers, (iii) sounding/suborbital/ballistic rockets, (iv) parabolic flights, (v) space shuttles/recoverable satellites, and (vi) onboard the International Space Station (ISS) [12].

1.2.1 Boiling Experiments at Different Orientations in Earth Gravity

The first option is the most cost effective and is performed by conducting several experiments in Earth gravity with the heated surface or flow channel placed at different orientations. This results in the gravitational field's components to be different for each orientation, which can then be isolated, and the effects of gravity assessed. Based on such data,

criteria have been proposed for operation in a gravity independent regime for both flow boiling [13,14] and flow condensation [15], meaning conventional design tools would be expected to well predict the two-phase heat transfer and flow physics independent of the gravitational field orientation. Although this type of experiments provides a preliminary assessment, the main drawback is that the gravitational field is not completely eliminated and hence is not a true capture of reduced gravity conditions.

1.2.2 Boiling Experiments in Short Microgravity Periods

Most microgravity (μg_e) experiments have been conducted using drop towers, parabolic flights, and sounding/suborbital/ballistic rockets, to obtain very short periods of microgravity ranging from a few seconds to a few minutes. Among these, most studies are on pool boiling and comparatively fewer on flow boiling. Some notable pool boiling studies in this category include:

(i) the parabolic-flight experiments of Oka *et al*. [16] for n-pentane on a titanium foil, Oka *et al*. [17] for n-pentane, R-113, and water on a glass plate plated with a transparent indium oxide film, Kim *et al.* [18] for FC-72 over a microscale heater array, and Ohta [19] for water and ethanol on a transparent sapphire glass plate,

(ii) the sounding-rocket experiments of Ohta *et al*. [20] for ethanol on a transparent sapphire glass plate and Souza *et al.* [21] for n-pentane on a downward-facing copper disc, and

(iii) the drop-tower experiments of Xue *et al.* [22] for FC-72 on a 1-cm^2 silicon chip, Wang *et al*. [23] for FC-72 on a 2-cm^2 silicon chip, and Yang *et al.* [24] for HFE-7500 and water on a metal-ceramic rectangular plate heater.

In 1993, Misawa [25] performed both drop-tower and parabolic-flight experiments of flow boiling of R-113 and reported the earlier transitions of flow patterns in μg_e than $1g_e$, which diminished at high flow qualities. Heat transfer performance was degraded in μg_e due to weaker bubble agitation reducing turbulence effects. To the contrary, the parabolic flight experiments of Baltis *et al.* [26] showed significantly enhanced heat transfer in μg_e, particularly near the tube entrance, and this was attributed to larger bubbles increasing mixing and turbulence. Higher flow rates overshadowed gravitational effects, leading to a convergence in heat transfer rates for all gravities. Saito *et al*. [27] performed parabolic-flight experiments of flow boiling of water over a horizontal heated rod in a square channel. They observed bubble detachment to significantly decrease in μg_e, resulting in vapor to surround the rod downstream; this observation was more pronounced at low flow rates and high heat fluxes, meaning high Boiling numbers. Even though the flow regimes were significantly different, the differences in heat transfer coefficient were only minor.

In addition to pool boiling, Ohta [19] also performed parabolic-flight experiments of flow boiling of R-113 through a glass tube coated with a thin resistive gold film. For low-quality bubbly flow boiling, they observed nucleate boiling heat transfer to be consistent between $1g_e$ and μg_e environments at both low and high mass velocities. For moderate-quality flow boiling resulting in the annular flow regime, nucleate boiling was suppressed, and heat transfer deteriorated in μg_e. At sufficiently high heat fluxes, nucleate boiling was observed within the annular liquid film, suppressing the effects of gravity. For high-quality annular flows, the dominant shear forces lessened the effects of gravity even at low heat fluxes. Flow boiling experiments in μg_e also saw increased vapor production resulting in larger bubble diameters and transition to annular flow at lower qualities. Critical Heat Flux (CHF) manifesting as dryout at high qualities was similar to Earth gravity. The drop-tower experiments of Ma and Chung [28] for flow boiling of FC-72 over a platinum wire revealed that, at low flow rates, μg_e produced significantly lower CHF values (q''_{CHF}) than $1g_e$. At sufficiently high flow rates, flow inertia suppressed the effects of gravity. Flow visualization revealed similar trends where, at low flow rates, bubble behavior was drastically different in μg_e than $1g_e$. Higher surface temperatures resulted in significant bubble coalescence in μg_e, whereas bubbles typically departed the wire in $1g_e$.

In 2005, Zhang *et al*. [29] performed parabolic-flight experiments of flow boiling of FC-72 in a rectangular channel, with a focus on investigating vapor production and flow behavior within the channel leading to CHF. As heat fluxes neared q''_{CHF}, in μg_e, a wavy vapor layer developed along the wall with little to no bubble detachment occurring. This vapor layer became thinner upon increasing either inlet subcooling or flow rate, due to higher subcooling promoting condensation at the liquid-vapor interface and higher flow rates increasing the drag force. At low flow rates, q''_{CHF} in μg_e was significantly lower than $1g_e$ horizontal flow, where buoyancy aided bubble detachment from the heated wall. At high flow rates, both the flow patterns and q''_{CHF} in μg_e and $1g_e$ converged to become similar. Later in 2015, Konishi *et al*. [30,31] performed parabolic-flight experiments of flow boiling of FC-72 in a rectangular channel with two opposite walls heated. Except for the lowest heat flux, which produced bubbly flow all along the heated section of the channel, a wavy vapor layer developed at both heated walls for all operating conditions. Heat transfer performance degraded in μg_e. The average thickness of the vapor layer increased upon increasing heat flux or decreasing mass velocity, meaning larger Boiling numbers. Close to CHF, the two vapor layers grew thicker and completely merged at the channel downstream.

In 2008, Luciani *et al*. [32] performed parabolic-flight experiments of flow boiling of HFE-7100 in a mini-channel and used inverse heat conduction techniques coupled with experimental data to provide local heat transfer values. In μg_e, vapor structures filled the width of the mini-

channel and heat transfer coefficient was locally higher. On the other hand, in hypergravity, a classical bubble structure was observed. Later in 2013, Brutin *et al.* [33] performed parabolic-flight experiments of vertical upflow boiling of HFE-7100 in a mini-channel, focusing on local void fraction and frictional pressure drop measurements. Bubbles grew much quicker in μg_e than in hypergravity (1.8 g_e in their study), typically resulting in bubbles of relatively smaller diameter in 1.8 g_e and big slugs in μg_e. The larger bubble growth and larger bubble departure diameters in μg_e resulted in thinner films, which increased heat transfer performance, and smaller effective liquid cross-section, which lowered frictional pressure drop.

In 2014, Narcy *et al*. [34] performed parabolic-flight experiments of flow boiling of HFE-7100 in a sapphire tube. For subcooled flow boiling corresponding to bubbly flow, at low flow rates, larger bubbles were observed in μg_e. The heat transfer coefficient here was lower in μg_e due to less frequent bubble nucleation and detachment. Increasing the flow rate caused the flow regimes in both μg_e and $1g_e$ to become similar. Increasing the quality caused flow to transition to slug and eventually annular; these transitions occurred at lower qualities in μg_e than $1g_e$. Within the annular flow regime, μg_e produced thinner liquid films, in spite of which, heat transfer coefficients were similar in both μg_e and $1g_e$ due to the dominance of shear forces.

In 2018, Zhang *et al*. [35] performed drop-tower experiments of flow boiling of FC-72 for a fixed inlet velocity and five heat fluxes. This was followed by the drop-tower and Earth-gravity experiments (at three orientations of 0°, 135°, and 315°) of Liu *et al*. [36] in 2020 for flow boiling of FC-72 in a rectangular channel for, once again, five specific cases of operating conditions. q''_{CHF} in μg_e was found to lie between the q''_{CHF} for 135° and 315° orientations in $1g_e$, which were proposed as the lower and upper bounds of q''_{CHF} in μg_e.

In 2019, Lebon *et al*. [37] performed parabolic-flight experiments of vertical upflow and downflow boiling of HFE-7100, during which, data was recorded continuously for g ranging from $-1.8g_e$ to $1.8g_e$. μg_e caused a decrease in slip velocity, less frequent bubble detachment, and less turbulent mixing, which all led to reduced bubbly-flow heat transfer compared to the other gravity levels. An exception to this general observation was an operating condition having nucleate boiling in μg_e and single-phase flow at other gravity levels, which was attributed to the rapid growth of thermal boundary layer in μg_e, resulting in increased heat transfer and bubble incipience. Later in 2020, Iceri *et al*. [38] performed parabolic-flight experiments of flow boiling of FC-72 and compared data obtained at different phases of the parabolas. Bubbles in μg_e were fewer, larger, and more circular compared to vertical upflow in $1g_e$ and hypergravity, which was attributed to the dominance of surface tension, particularly at low flow rates. In the annular flow regime, μg_e produced the thickest liquid film and lowest heat transfer coefficients.

Overall, although these techniques of establishing short durations of μg_e prove to be cost effective and yield some μg_e data, they suffer from inherent issues. Drop towers create a high quality of μg_e , but the μg_e period is too short to effectively reach steady state for most experiments [39]. Parabolic flights and sounding rockets create relatively longer μg_e durations compared to drop towers, but typically produce small fluctuations in the established μg_e level (termed *g-jitter*), degrading the μg_e quality [40]. g-jitter has also shown to artificially enhance heat transfer in μg_e by continuously deforming bubble shape provoking flow around the bubble [41].

1.2.3 Boiling Experiments in Long Microgravity Periods

The most accurate and highest quality μg_e data can be collected by performing experiments on long periods of stable μg_e, such as recoverable satellites or the International Space Station (ISS). Some barriers which inhibit these types of experiments are the high risk of failure, very high cost, long time commitment, and size, weight, and power constraints. To the best of the authors' knowledge, all boiling experiments in long μg_e periods have been for pool boiling, except for the present study and another concurrent effort led by the Japanese Aerospace eXploration Agency (JAXA), which are focused on flow boiling. Some prominent pool boiling studies include both Lee *et al.* [42] and Merte [43] for R-113 on a semi-transparent gold film sputtered over a rectangular quartz plate onboard a NASA space shuttle, Zhao *et al.* [44] for R-113 on a thin platinum wire onboard a Chinese recoverable satellite, Zhao *et al.* [45] for FC-72 on a flat plate onboard another recoverable satellite, Raj *et al.* [41] for nPFH onboard the ISS as part of the Microheater Array Boiling Experiment (MABE), and Dhir and Warrier *et al*. [46,47] for nPFH onboard the ISS as part of the Nucleate Pool Boiling eXperiment (NPBX).

Researchers in collaboration with JAXA have outlined several research objectives in [48] for flow boiling experiments of nPFH through copper and transparent glass heated tubes of 4-mm inner diameters. Recent articles from 2021 report the estimation of heat loss for their ISS experimental system to accurately determine the inlet conditions for both single-phase [49] and two-phase inlet [50].

More recently, in 2022, researchers working with the European Space Agency (ESA) have outlined six objectives for a multiscale boiling investigation to be conducted onboard the ISS, including the (i) observation of contact line behavior, (ii) observation of bubble growth, (iii) assessment of the effects of an electric field, (iv) shear flow, (v) binary mixtures, all with respect to single bubbles, and finally (vi) bubble interaction effects [51].

1.3 Objectives of Study

The present study is the culmination of a long-term collaborative effort between researchers at the Purdue University Boiling and Two-Phase Flow Laboratory (PU-BTPFL) and the NASA Glenn Research Center (GRC) to study gravitational effects on flow boiling and condensation. Development of the "Flow Boiling and Condensation Experiment (FBCE)," which is actually the name of the experimental facility, largest and most complex fluid physics initiative ever developed for NASA research, was initiated in 2011 with an ultimate goal of being installed onboard the International Space Station (ISS) and collecting long-term microgravity data. The team has published several studies as part of FBCE in prior years, which reported the results of flow boiling experiments conducted both at different flow orientations in Earth gravity [14,52–56] and onboard an aircraft performing parabolic maneuvers to establish short durations of microgravity [29–31]. Scientific findings and technical knowhow from these preliminary experiments enabled the team to build a final experimental system destined for the ISS, and its safe operating procedure. Pre-launch experiments (termed Mission Sequence Testing, MST) were conducted using this system in the vertical upflow orientation in Earth gravity, and the results were recently reported in [57–59]. Using large consolidated databases containing datapoints from all FBCE experiments, new correlations were developed for both subcooled flow boiling heat transfer coefficient [60] and CHF [61] applicable to large ranges of operating parameters, gravitational fields, and heating configurations.

The FBCE system fitted with the Flow Boiling Module (FBM) was launched to the ISS in August 2021 and later installed onboard and several safety checks conducted. After being deemed successful, flow boiling experiments were conducted for about six months from February 2022 until July 2022, which resulted in a large flow boiling database covering broad operating-parameter ranges and heating configurations with focus on several research objectives. It is noteworthy that the experimental matrix was almost full factorial, and the operating parameters were finely incremented throughout the ranges to be thorough.

This study presents experimental heat transfer and flow visualization results of flow boiling in microgravity with subcooled inlet conditions and single-sided heating of rectangular channel. Images and image sequences from high-speed-video flow visualization are presented and the two-phase flow physics discussed. Heat transfer results are presented as flow boiling curves, streamwise profiles of wall temperature and heat transfer coefficient, and parametric trends of local and averaged heat transfer coefficient. The effects of various parameters (mass velocity, inlet subcooling, and inlet pressure) are discussed. Also presented are examples of anomalous flow boiling situations which resulted in deviations in parametric trends.

2. Experimental Methods

2.1 Two-Phase Flow Loop

A schematic of the closed two-phase flow loop used in this ISS study is illustrated in Fig. 2, with all primary components indicated. The flow loop conditions the working fluid, n-Perfluorohexane (nPFH, C_6F_{14}), to that desired at the inlet of the test module, FBM. nPFH, a fluorocarbon, is chosen for these experiments due to its remarkable thermophysical properties making it an excellent candidate for thermal management in space missions [62]. A magnetically coupled positive-displacement internal gear pump moves the subcooled liquid through the loop. For safety reasons, two relief valves are provided in parallel across the upstream and downstream of the pump to let liquid pass from pump downstream (high pressure end) to pump upstream (low pressure end) in case the pressure differential exceeds the preset cracking pressures. One valve cracks open at 199.95 kPa (29.00 psid) and the other at 206.84 kPa (30.00 psid), the latter serving as a backup in case the former fails. A Coriolis flow meter downstream of the pump measures the flow rate and this signal serves as feedback to a flow controller which maintains the desired set flow rate by adjusting the rotation speed of the pump head. A filter then removes any possible impurities from the liquid. A preheater (termed the Bulk Heater Module, BHM) inputs heat to the subcooled liquid to increase its temperature and even produce vapor (when necessary) based on the desired inlet temperature and quality to the FBM. The preheater is equipped with a set of heaters powered by direct current (DC) to generate heat and instrumented with thermocouples and Resistance Temperature Detectors (RTDs) to provide feedback to shut the heaters down in case of two scenarios: (i) when the heating surface exceeds 130°C or (ii) the fluid temperature at the preheater outlet exceeds 100°C. Subcooled liquid with a desired degree of subcooling enters the FBM, wherein it receives a set amount of heat and exits the FBM as either a subcooled liquid or two-phase mixture. A fluid-to-water stainless-steel tube-in-tube heat exchanger with a spiral-finned inner tube serves as condenser, removes heat from the fluid, and returns it to a subcooled liquid state of minimum temperature within the fluid loop. The secondary fluid to this heat exchanger is cooling water from the ISS; this ancillary open water loop within FBCE is equipped with its own flow meter, valves, flow controller, RTDs, and pressure transducers. A static mixer situated downstream of the condenser continuously mixes the fluid without any moving parts and condenses any possible vapor bubbles entrained in the subcooled liquid, ensuring thermodynamic uniformity before it reaches the pump. This reduces the possibility of cavitation and resulting pump head wear.

Connected to the main flow loop at a T-junction immediately downstream of the static mixer is an accumulator, which maintains a desired set reference pressure point in the loop and helps reduce two-phase flow instabilities in the loop and within the FBM [63,64]. The accumulator holds the majority of working fluid on one side of stainless-steel bellows and on the other side is

pressurized air, whose pressure is controlled by combination of an air pump and a vent valve. A relief valve is provided right next to the vent valve for safety reasons, and cracks open when the pressure differential exceeds 137.90 kPa (20.00 psig).

The section of the flow loop between the accumulator's T-junction and the pump is split into two parallel paths, with a system of two shut-off valves and one check valve routing flow through only one path at a time. One path is without any additional components and is used during regular experimentation. The other path contains a degassing contactor, which removes non-condensable gases from the working fluid and increases both the accuracy and reliability of the collected two-phase data. Internally, the contactor contains a specialized semi-permeable membrane, with fluid flow on one side and vacuum applied on the other side.

Most valves are solenoid actuated to enable remote experimentation on the ISS.

2.2 Practical Construction of Experimental System

The actual layout of main modules of the FBCE on the Optics Bench of the Fluid Integrated Rack (FIR) is illustrated in Fig. 3, along with the ISS provided hardware. There are six primary FBCE modules: Bulk Heater Module (BHM), Fluids System Module – Upper (FSMU), Fluids System Module – Lower (FSML), Remote Data Acquisition Module 1 (RDAQM1), Remote Data Acquisition Module (RDAQM2), and Test Module Assembly (TMA). For the experiments reported in this study, the FBM was installed as the TMA. Before launching to the ISS, all the two-phase flow loop components already discussed in section 2.1 are segregated and packaged into these modular boxes. After launch and delivery to the ISS, astronauts assemble them together using other instrumentation. After assembly, the Optics Bench is rotated to the vertical upward orientation inside the Fluid Integrated Rack (FIR). The FIR contains three essential systems: Space Acceleration Measurement System (SAMS), Confocal Control Unit (CCU), and Image Processing Storage Unit – Camera Link (IPSU-CL). Photos of the FIR are included in Fig. 4, with the various auxiliary systems and components identified, including the Environmental Control System (ECS) and Electrical Power Control Unit (EPCU). Shown at the bottom of Fig. 4 is a photograph of the FBCE integrated into the FIR.

CAD renderings and photographs of the FSMU and FSML are shown in Fig. 5. The FSMU (shown at the top) contains the degassing contactor, gear pump, flow meter, mass flow controller, and filter. The vacuum capability required for the degassing contactor is provided by the ISS Vacuum Exhaust System (VES). The FSML (shown at the bottom) contains the condenser, static mixer, and accumulator. Cooling water required for the condenser is provided by the ISS Thermal Control System (ITCS) through the FIR's Water Interface Panel (WIP). nPFH from the TMA (FBM in the present study) enters FSML, FSMU, and BHM in series before entering the TMA

again. Fig. 6 illustrates the nPFH, water, air, and vacuum connections between the FBCE modules and the ITCS and VES. The internal placements of the various primary components within the FBCE modules are also schematically shown.

A CAD rendering and photographs of the BHM are included at the top of Fig. 7. The BHM contains three 120 V primary heaters and three 28 V booster heaters, which can be operated at any time, with backup heaters available. The bottom of Fig. 7 shows photographs of the packaged RDAQM1 and RDAQM2. The RDAQM1 contains UEI data cubes that are utilized for thermocouple signal conditioning. The RDAQM2 contains both UEI data cube and custom-sensor-supply printed circuit board for signal conditioning of other sensor signals and power distribution.

2.3 Flow Boiling Module

Schematics of the overall construction of the experimental system's principal component, the FBM, is illustrated in Fig. 8, and key dimensions included in Table 1. The FBM is constructed from three transparent polycarbonate plates held together, Fig. 8(a); the top and bottom plates are 25.15-mm thick, and the middle plate is 5.0-mm thick. The flow channel is formed within the middle plate by milling a 5.0-mm deep and 2.5-mm wide rectangular slot, which is then further milled on either side of the channel to house two oxygen-free copper heating strips of dimensions 114.6-mm length, 15.5-mm width, and 1.04-mm thickness (see Fig. 8(b)). The strips are wider than the channel width to effectively embed them within the polycarbonate plates and seal using O-rings. The three polycarbonate plates are finally sandwiched between two 13.72-mm-thick aluminum 7075 support plates to prevent both buckling of the FBM plates and fluid leaks by spreading the bolting stresses uniformly across the FBM. All solid-solid interfaces within the FBM are leak-proofed by using O-rings made of synthetic rubber.

Flow enters and exits the FBM at 90° angles to the flow channel, which can be axially demarcated into three sections: an upstream development length of L_d = 327.7 mm, a middle heated length of L_h = 114.6 mm, and a downstream exit length of L_e = 60.7 mm (see Fig. 8(a)). The development length serves to have the flow become hydrodynamically fully developed before it reaches the start of the heated section. Affixed close to the inlet of the development length is a 12.19-mm-thick aluminum 5052 honeycomb insert, which straightens out the flow streamlines and breaks down any large eddies. Overall, the development and exit lengths along with the honeycomb insert isolate the heated section from any swirl effects produced by the 90° flow entry and exit.

As shown in Figs. 8(b) and 8(c), on one side of the heating strips are affixed a set of six thick-film resistive heaters in series and the other flat side constitutes the fluid heating surfaces.

Each resistive heater is of dimensions 16.4-mm length, 4.5-mm width, and 0.56-mm thickness, and consists of an aluminum oxide substrate with a 188-Ω resistive layer stretched between two solder pads on its underside. For a uniform heat flux distribution along the strips, all chosen heaters have very close electrical resistances, are wired in parallel, and powered by DC. The heaters are soldered to the copper strip to form a solder layer of 96% tin and 4% gold composition, after which, the thickness of copper between the heaters and the fluid heating surface is 0.56 mm. A small 0.9-mm separation is provided between two neighboring heaters to enable thermocouple access to the heating strip. A maximum power of 175 W can be independently supplied to each strip. This heated wall design allows for fast temperature response and reliable and accurate CHF measurement [29,30].

Fig. 9 shows CAD renderings and photographs of the FBM. The CAD rendering at the top shows all components within the FBM box including the camera system and the photo in the middle shows the final assembled FBM.

2.4 Camera System and Flow Visualization

Analysis of the interfacial physics of flow boiling is possible by flow visualization using high-speed video photography of all heat flux increments from a minimum until (and including) CHF. This is made possible by the transparency of the polycarbonate plates allowing for excellent visual access to within the FBM's heated section. All three plates were further vapor polished to minimize vignetting effects produced by the opaque copper strips and O-rings.

The primary component of the high-speed video camera is a Complementary Metal Oxide Semiconductor (CMOS) sensor, each pixel of which is a square of size 5.5 μm × 5.5 μm. The CMOS sensor has a fill factor of 100%, *i.e.*, the pixels are arranged with no physical distance between them. The camera system was subject to spatial resolution tests conducted using the Ronchi ruling (sinusoidal intensity grating) and a spatial resolution of at least ~90 μm was achieved, *i.e.*, the camera was able to read ~180 μm using the line-pair-per-mm criteria at 50% dynamic range, which is equivalent to ~90 μm spatial resolution per Rayleigh criteria.

The high-speed video camera is pointed at one of the transparent channel walls representing the channel height of H = 5.0 mm, while the opposite channel wall is backlit with blue light emitting diodes (LEDs) in tandem with a light-shaping diffuser fitted with an intermediate Teflon sheet, which is necessary due to the extremely short light transmission distance. This arrangement can be seen in the top CAD rendering included in Fig. 9. The camera, fitted with a F#0.95-25 mm lens, captures photographs of resolution 2040×164 pixels at a high frame rate of 2000 frames per second and low shutter speed of 10 μs. For all steady-state heat flux increments prior to CHF, images are recorded for the latest 1.0-s period before the heat flux is incremented, whereas for the

heat flux increment corresponding to CHF, the latest 7.0-s period before heater shutdown is recorded to analyze the flow transience around CHF. It is noted that the captured images included in this paper have been post-processed to make the flow features distinct, but without introducing any artificialities. The heat produced by continuous camera operation is removed through a dedicated cold plate, which receives cooling water from the ITCS, and this water loop is also equipped with its own mass flow controller, valves, *etc*. (see Fig. 6).

Besides the high-speed camera system, an additional analog camera of a typical 30 frames/s frame rate is included within the FBM and directed at the heated section; this is used for live flow monitoring during experiments.

2.5 Instrumentation and Measurement Accuracy

The FBM is equipped with five absolute pressure transducers (one each near the inlet and outlet, and three at intermediary locations within the development length as shown in Fig. 2) to measure local absolute pressures. For this study focusing on the FBM's heated section, the pressures reported as p_{in} and p_{out} correspond to measurements made by the fourth and fifth pressure transducer from the FBM inlet, respectively. The FBM is also equipped with two type-E thermocouples extending into the flow used to measure the inlet and outlet fluid temperatures. As shown in Fig. 8(c), each heating strip houses two sets of seven type-E thermocouples each to measure local strip temperatures. The tips of these thermocouples are placed in shallow hemispherical indentations made into the strip, such that the copper thickness between the thermocouple tip and the fluid heating surface is 0.48 mm. One set of these thermocouples is used for data acquisition and software reset of the FBM heater power level when any local temperature exceeds 122°C, usually an aftermath of CHF occurrence. The other set is part of a hardware safety circuitry and is used to provide feedback to a relay that shuts down the FBM heaters in case the software reset fails at 122°C and any local temperature exceeds 132°C.

Besides the FBM, the entire flow loop is equipped with a multitude of absolute pressure transducers, thermocouples, and RTDs, to measure and monitor local pressures and temperatures at important locations (some are indicated in Fig. 2).

RDAQM2 internally measures the voltages and currents to each FBM copper strip, which are used to calculate the power input to each wall. The Coriolis flow meter measures the mass flow rate of nPFH in the range of 0-60 g/s.

The output signals from all sensors are collected and fed to both RDAQM1 and RDAQM2 for continuous temporal measurement and recording at a higher sampling frequency of 5 Hz during active experiments and a lower frequency of 1 Hz whenever the experimental system is turned on (termed 'housekeeping' data). As already mentioned, RDAQM1 is used for thermocouple data

and RDAQM2 for other sensors. An in-house FBCE flight software is used to monitor and control both the DAQs and all other instruments, including solenoid valve actuation.

Table 2 contains the maximum uncertainties in the measurements of important parameters.

2.6 Remarks on Experiment Choice

2.6.1 Significance of Forces Acting on Fluid

The hydraulic diameter of the FBM's rectangular channel is D_h = 3.33 mm, and the confinement number is calculated as

$$Co = \frac{1}{D_h}\sqrt{\frac{\sigma}{\left(\rho_f - \rho_g\right)g}}\,. \tag{1}$$

For the prior Earth-gravity MST experiments, $g = g_e$, and Co = 0.195 – 0.216 [57]. Several threshold criteria for dominance of macroscale effects over microscale effects (*i.e.*, dominance of gravitational forces over surface tension forces) are available in the literature (Co < 0.5 by Kew and Cornwell [65], Co < 0.79 by Brauner and Ullmann [66], Co < 0.57 by Li and Wang [67], and Co < 0.3-0.4 by Ong and Thome [68]; originally proposed values for other dimensionless groups converted to corresponding Co values in [68]). This confirms that, when the FBM is operated in the vertical upflow orientation in Earth gravity, gravitational forces are more significant than surface tension. However, the same cannot be said for the present ISS experiments, as $Co \rightarrow \infty$. In μg_e, flow inertia and surface tension dictate the flow physics within the channel.

2.6.2 Single-Sided Heating of Rectangular Channel

Single-sided heating, *i.e.*, heating just one wall of the rectangular channel, is analyzed in this first study resulting from the FBCE ISS experiments. When only one wall is heated, the produced bubble boundary and vapor layers are undisturbed by vapor produced at other walls, and their evolution will completely depend on the operating conditions and the fact that body forces are negligible. Parametric trends on both heat transfer and flow physics in μg_e can be analyzed to verify if they align with those already established on Earth. In fact, the initial studies leading up to FBCE [69–71] focused on single-sided heating. Later, when the μg_e and g_e data are compared, the effects of body forces both parallel and perpendicular to the heated wall can be easily isolated.

2.6.3 Subcooled Inlet Conditions

The inlet fluid state for flow boiling can be either subcooled liquid or saturated two-phase mixture, and this dictates the flow pattern development and heat transfer physics. Practically, subcooled inlet is preferred for thermal management applications because subcooled flow boiling offers better heat transfer performance and q''_{CHF} and reduced pressure drop than saturated flow

boiling. These are due to the utilization of both sensible and latent modes of heat transfer and the condensing capability of the subcooled bulk fluid, both of which improves upon increasing the degree of inlet subcooling. It is noted that due to thermodynamic non-equilibrium, the fluid might be subcooled, but still exist as a two-phase mixture.

Only subcooled-inlet flow boiling of nPFH in a rectangular channel with single-sided heating is considered in this study. The experiments reported here are loosely termed as highly subcooled inlet for roughly $\Delta T_{sub,in} > 10^{\circ}\text{C}$ and near-saturated inlet for roughly $0 < \Delta T_{sub,in} \leq 10^{\circ}\text{C}$.

2.7 Experiment Procedure

All experiments were performed with the FBCE system onboard the ISS and with operators remotely controlling from the Telescience Center (TSC) at NASA GRC. After the astronauts installed the FBCE system on the FIR, the experiments were remotely executed from the TSC at GRC. Both sensor-measured and photography data were transmitted back to the personnel at GRC. The entire FBM testing took a period of ~5 months and, during this period, the operating procedure was tweaked several times to address several unexpected system behaviors, which were observed and deemed insignificant during the MST experiments conducted at GRC [57,59].

The nPFH is degassed for a few hours before the start of testing each day and for whole days whenever decided to be necessary. Degassing is essential on the ISS because the system is exposed to air at ambient pressure, and there is possibility of air leaking into the system (at sub-atmospheric system states) and dissolving in nPFH.

The predetermined FBM inlet conditions (mass velocity, inlet pressure, and inlet subcooling) for each test run (boiling curve) are set within the software, and the flow loop is allowed to reach them and become steady. DC power is supplied to one of the two heating strips for single-sided heating (and both for double-sided heating) at a minimum value and is incremented in steps to predetermined levels at regular intervals of 120 – 180 s, which were deemed sufficient to reach steady state for flow boiling from the MST [57,59] and prior FBM studies [29,30]. The first 12 increments are set based on an estimated q''_{CHF}, the initial increments are finer to capture the Onset of Nucleate Boiling (ONB), after which the increments are made coarser because temperatures do not vary much during nucleate boiling; finally, the increments are made finer once again to accurately capture CHF. In case CHF is not attained by the 12th increment, more automated small increments are allowed. Although CHF is defined as the heat flux which leads to an unsteady and uncontrollable rise in surface temperature, for safety reasons, CHF for these experiments is designated to occur at the heat flux which prompts at least one local strip temperature to exceed 122°C. As soon as any of the strip data thermocouples detects this temperature exceedance, the FBCE software executes a software reset of the FBM heaters,

bringing down the heater power to a minimum (If this fails, as soon as the strip safety-circuitry thermocouples detect a temperature exceeding 132°C, the heaters are completely shut down; fortunately, this scenario was not encountered in this series of tests). These precautions are done for two reasons: (i) to prevent any irreversible damage to the FBM, especially thermal deformation or warping of the polycarbonate plates and (ii) to avoid the breakdown of nPFH and formation of toxic perfluororisobutene (PFiB). Both continuous temporal data from all sensors and high-speed images for all heat flux increments are recorded. Since the actual value of CHF, q''_{CHF}, could lie anywhere between the last heat flux increment that reached steady state and the heat flux increment that resulted in one of the thermocouples reaching 122°C, the average of these two heat fluxes is reported as q''_{CHF} in this study.

The above procedure is repeated for all FBM inlet conditions predetermined in the test matrix.

2.8 Temporal Records for a Representative Boiling Curve

For a representative set of operating conditions, temporal variations of fluid inlet (T_{in}), fluid outlet (T_{out}), and heating-strip (T_{tc}) temperatures are shown in Fig. 10(a) for wall heat flux, q''_w, ranging from a minimum to q''_{CHF}. The temperatures correspond to the left axis and the wall heat flux to the right axis. At time $t = 0$ s, q''_w is increased from a minimum value to a certain steady level, and at $t = 120$ s, q''_w is increased again. The strip temperatures are initially equal to the fluid temperature and make two large jumps during the first two heating periods; for single-phase flow, a waiting period of 120 s in inadequate to reach steady state within this time. As soon as q''_w is increased for the third time at $t = 240$ s, T_{tc} initially increases, reaching a local peak and then drops; this is referred to as a *transient temperature overshoot* or the *incipient boiling superheat* due to the required superheat for bubble incipience being higher than that to sustain boiling. Let t_1 and t_2 denote the time instants at the end of the second and third heat flux increments. At these time instants, high-speed photos were recorded, which are shown in Fig. 10(b) for the entire heated length (left wall is heated). The flow is upwards, and any vapor bubbles produced within the channels are barely seen due to their small sizes. For clarity, enlarged half-channel-width images are included for three locations of this channel, *viz*., at the inlet, middle, and outlet. At t_1, none of the images show any vapor bubbles. But at t_2, although bubbles are not seen near the channel inlet, smaller bubbles are seen halfway along the channel and bigger bubbles are seen near the channel outlet. This is a clear indication of the third heat flux increment corresponding to ONB, q''_{ONB}, and it activates cavities starting someplace between the channel inlet and middle. All q''_w increments after the second are characterized by nucleate boiling and reach steady state. For the final increment, at $t \approx 1390$ s, the strip temperatures sharply spike upwards and $T_{tc1,5}$ reaches the

122°C maximum operating temperature, and the heaters are powered down. In addition, note how all prior increments have a concave-downward-shaped temperature profile, whereas the last increment does not; this behavior is seen for the majority of test cases in this study. These are clear indications of CHF behavior.

Overall, these temporal records corroborate that typically (i) all heat flux increments between ONB and CHF, characterized by boiling, attain steady state and (ii) the 122° strip temperature escalation is caused by CHF.

2.9 Data Processing and Experimental Ranges

Data processing procedure for the present ISS experiments is very similar to the Earth-gravity MST experiments reported in [57]. The raw temporal data are examined to identify all heat flux increments that reached steady state. Steady state datapoints are obtained by averaging the latest 20 s of temporal datapoints of each steady state period. All thermophysical properties of nPFH are obtained from NIST-REFPROP [72].

At the FBM inlet, the fluid is in a subcooled liquid state, and the corresponding fluid enthalpy is directly determined from the FBM inlet fluid temperature, T_{in}, and pressure, p_{in}, as

$$h_{in} = h\big|_{T_{in}, p_{in}}. \tag{2}$$

At the FBM outlet, the fluid can contain some vapor, and the fluid enthalpy is calculated from an energy balance over the FBM as

$$h_{out} = h_{in} + \frac{q''_w P_h L_h}{\dot{m}}, \tag{3}$$

where q''_w is wall heat flux, $\dot{m}$ mass flow rate, and P_h heated perimeter equal to channel width, W, for single-sided heating. As already detailed in [57], the FBM was carefully designed to minimize heat loss. The copper strips are fully encased within the polycarbonate plates except for (i) the strip surface in contact with the nPFH and (ii) the thin and deep slots in the polycarbonate plate where the thermocouples and heater leads are taken out, where the heating strips are in contact with quiescent air. Since both the polycarbonate plates and air have low thermal conductivity, and the heat transfer coefficient on the nPFH side is large, almost all heat generated within the electric heaters enters the nPFH. An extensive heat loss estimation was performed by Konishi *et al*. [73] for a similar test module geometry. The older module was different from the present FBM in two main aspects: (i) only one heating strip rather than two and (ii) a comparatively shorter heating length. For both single- and two-phase flows, heat losses amounted to a maximum of 0.2% of power input. This 0.2% is within the maximum heater-power-measurement uncertainty of 0.3% (see Table 2) and hence considered negligible. So, q''_w is directly calculated as the FBM heater power divided by the total surface area of heating the nPFH.

Thermodynamic equilibrium qualities at both the FBM inlet and outlet are determined as

$$x_e = \frac{h - h_f\big|_p}{h_{fg}\big|_p}, \tag{4}$$

where $h = h_{in}$ or h_{out} is the actual fluid enthalpy at the FBM inlet/outlet, and both h_f, the saturated liquid enthalpy, and h_{fg}, the latent heat of vaporization, are evaluated at the measured inlet/outlet pressure.

Per Fig. 8(c), local wall temperatures are designated as $T_{wa,z}$, where wa is the heated wall ($w1$ or $w2$) and z the streamwise measurement location (1 upstream through 7 downstream). Each local wall temperature, T_w, is calculated from the corresponding measured strip temperature, T_{tc}, by assuming a uniform heat flux and one-dimensional heat conduction through distance, H_{tc} (= 0.48 mm) within pure copper of thermal conductivity, k_s, as

$$T_w = T_{tc} - \frac{q''_w H_{tc}}{k_s}, \tag{5}$$

Given the short conduction distance and high thermal conductivity of copper, the copper conduction resistance between the two locations is minuscule, and T_w is found to be lower than T_{tc} by a maximum of just 0.68°C.

Both saturation temperature, $T_{sat,z}$, and thermodynamic equilibrium quality, $x_{e,z}$, at these locations are determined by linear interpolation between values at the inlet and outlet. Heated single-phase length is estimated as

$$L_{h,sp} = \frac{GA_c}{q''_w P_h}\left(h_f\big|_{p_{in}} - h_{in}\right), \tag{6}$$

and saturation temperature at the end of $L_{h,sp}$ (*i.e.*, at location where $x_e = 0$) is estimated by linear interpolation as

$$T_{sat,xe=0} = T_{sat}\big|_{p_{in}} + \left(T_{sat}\big|_{p_{out}} - T_{sat}\big|_{p_{in}}\right)\frac{L_{h,sp}}{L_h}. \tag{7}$$

The fluid temperature at the streamwise locations is estimated based on the local fluid state as

$$T_{f,z} = \begin{cases} T_{in} + \left(T_{sat,xe=0} - T_{in}\right)\dfrac{z}{L_{h,sp}}, & x_{e,z} < 0 \\ T_{sat,z}, & 0 \le x_{e,z} \le 1 \end{cases}. \tag{8}$$

Local heat transfer coefficient at any location is defined as

$$h_{a,z} = \frac{q''_{wa}}{T_{wa,z} - T_{f,z}}, \tag{9}$$

from which, averaged heat transfer coefficient for the entire heated wall is determined as

$$\overline{h} = \frac{\sum_{N_z} h_{a,z} A_{h,z}}{A_h} = \frac{\sum_{N_z} h_{a,z} L_{h,z}}{L_h}, \tag{10}$$

where N_z = 7 is the number of streamwise measurement locations, $A_{h,z}$ and $L_{h,z}$ are the heated surface area and length of each unit cell represented by the measurement, respectively, and A_h and L_h are the total heated surface area and total heated length, respectively. Averaged wall temperature, $\overline{T_w}$, is also determined in a similar fashion.

From the measurement uncertainties reported in Table 2, uncertainty propagation is analyzed and the maximum uncertainty in important calculated parameters is estimated using the root-mean-square method. By assuming a very conservative 1% uncertainty in length measurements, the maximum uncertainty in q''_w is 1.45%. For the majority of the present database, the minimum value of $(T_{wa,z} - T_{f,z})$ is ~7°C, which results in a maximum uncertainty in h_z of 10.21%.

A summary of key parameters of the ISS steady-state database is included in Table 3 for subcooled inlet with single-sided heating, *i.e.*, the results reported in this paper.

A summary of all ISS experiments considered in this paper are reported in Table 4. The actual experimental reference numbers (Expt.#) are included to enable the heat transfer community to cross-reference the reported results with the experimental database, which will be openly made available on the NASA repository in the future; the latter three digits correspond to the actual predetermined test number, while the first digit (for a four-digit number) represents the trial/repetition number. The experiment reference numbers are included in the figures presenting experimental results. The reported parametric values are averages of the steady-state values at all heat increments throughout the entirety of each test run.

3. Flow Visualization Results and Discussion

This section presents flow visualization images capturing the FBM's heated length. Two types of images are presented (i) images capturing the evolution of the average flow pattern in the FBM for increasing heat fluxes along the boiling curve, from q''_{ONB} to q''_{CHF}, and (ii) time sequential images capturing the transient flow characteristics. A variety of operating conditions are selected to provide a thorough investigation of the parametric effects of mass velocity, inlet subcooling, and inlet pressure on flow patterns in microgravity. These observations shed light on the underlying heat transfer mechanisms and help understand the experimental heat transfer results reported in section 4. Accompanying each set of images for the selected test runs, are the averaged steady-state operating conditions throughout the boiling curve.

A schematic representation of the single-sided heating configurations is shown in Fig. 11, and all flow visualization images in this paper conform to this format. Flow enters from the bottom end of the channel at the given inlet conditions. Any one of the two walls is heated as heating either wall is expected not to influence boiling behavior in μg_e.

3.1 Flow Patterns Along the Boiling Curve

3.1.1 Flow Patterns for Fixed Moderate Mass Velocity and High Inlet Pressure – Effects of Inlet Subcooling and Heat Flux

Fig. 12 depicts sets of images recorded at different heat fluxes along the boiling curve for experiments with a fixed mass velocity of G = 799.96 – 803.13 kg/m^{2}s and a variety of inlet subcoolings. In Fig. 12(a), $\Delta T_{sub,in}$ = 2.11°C, meaning fluid enters the heated length with an inlet temperature 2.11°C less than the saturation temperature. Even at the lowest heat flux of q''_w = 12.92% q''_{CHF}, discrete bubbles are seen along the entire heated wall. Bubbles are noticeably larger in the downstream section of the channel's heated length, due to thermal boundary layer evolution and coalescence of nearby bubbles. Subsequent increases in heat flux result in a thicker and denser bubble layer along the heated wall. At 44.12% q''_{CHF}, bubble coalescence creates a fairly continuous vapor layer along the heated wall. The liquid-vapor interface is wavy, with crests and troughs respectively corresponding to large vapor patches sliding along the heated wall and zones in between vapor patches allowing liquid contact with the heated wall (termed *wetting fronts*). Due to the wall shear of the moving wetting fronts, a thin liquid sublayer develops along the heated wall beneath the thick vapor layer and bubble nucleation is still observed within this sublayer. By 73.59% q''_{CHF}, the liquid sublayer is completely vaporized, and wetting fronts become the primary source of cooling for the heated wall. The size of the vapor patches, and consequently the distance between wetting fronts, continues to grow as heat flux is increased, advancing the most downstream wetting front further upstream. At 100% q''_{CHF}, wetting fronts are incapable of meeting the cooling requirements of the heated wall and are completely extinguished, escalating strip temperatures to 122°C as vapor entirely blankets the heated wall.

In Fig. 12(b), fluid enters the heated length with a slightly higher subcooling of $\Delta T_{sub,in}$ = 6.06°C. At this subcooling, a single-phase liquid length occupies the upstream portion of the channel at 17.04% q''_{CHF}. Downstream, after sufficient wall superheat is achieved and the near-wall liquid layer exceeds the saturation temperature, ONB occurs (this is the expected mechanism of ONB although near-wall liquid temperature measurements are not made in these experiments). In the ensuing heat increment of 32.63% q''_{CHF}, ONB occurs further upstream, and more prominent bubble coalescence, owed to the higher wall heat flux activating more nucleation sites, results in larger bubbles downstream. Bubbles detach from the heated wall, a common characteristic of net vapor generation (NVG) being achieved and transition to the fully developed boiling (FDB) regime [7,74]. The development of a wavy vapor layer becomes clear at 54.17% q''_{CHF}. As seen in Fig. 12(a), increasing the heat flux results in the growth of vapor patches, advancing wetting fronts further upstream until CHF. However, at 100% q''_{CHF}, unlike Fig. 12(a), wetting fronts are still

present in the upstream region enabling nucleate boiling. However, CHF occurs once enough wetting fronts are evaporated and heat dissipation in the downstream portion of the channel is insufficient, causing strip thermocouples to exceed 122°C.

As subcooling is further increased, its effect becomes increasingly more noticeable, as seen in Figs. 12(c-g). In Fig. 12(c), $\Delta T_{sub,in} = 9.58$°C, a rather significant upstream single-phase length exists until 33.05% q''_{CHF} when compared to Figs. 12(a) and (b). The higher degree of subcooling requires a larger amount of heat to raise the local fluid temperature to the saturation temperature. In the same vein, bubble growth and detachment are impeded by the subcooled liquid condensing vapor at the liquid-vapor interface, delaying transition to the FDB regime until the channel downstream at 46.81% q''_{CHF}. Contrary to the differences seen early in the boiling curve, the flow patterns approaching CHF are similar to those seen in Figs. 12(a) and (b). At 23.46% q''_{CHF} in Fig. 12(d), $\Delta T_{sub,in} = 15.20$°C, only tiny bubbles are present along heated wall, visible as dark specs on the left wall. Generated bubbles briefly slide along the wall but are quickly condensed by the subcooled bulk liquid. This mechanism dominates until 59.12% q''_{CHF}, when the bubble layer grows appreciably along the channel. At 70.03% q''_{CHF}, a wavy vapor layer forms downstream, while the effects of subcooling remain prominent upstream. Further increasing the heat flux develops the vapor layer further upstream and thickens it along the channel, eventually culminating in CHF. At $\Delta T_{sub,in} = 19.84$°C, shown in Fig. 12(e), no bubbles are visible at 22.25% q''_{CHF} despite the temporal strip-temperature records indicating ONB occurred. Similar to the previous subfigure, the dominant role of condensation suppresses bubble growth immediately at the heated wall such that bubbles are not easily visible. However, by 55.43% q''_{CHF}, a bubble layer grows axially along the heated wall. Approaching CHF, starting at 83.59% q''_{CHF}, a wavy vapor layer exists in the channel. Unlike previous subfigures, large vapor patches no longer occupy the entire cross section of the channel downstream, albeit with select peaks touching the opposite wall. Fig. 12(f) shows images for $\Delta T_{sub,in} = 29.76$°C displaying similar flow behavior and characteristics as Fig. 12(e). At low and high heat fluxes, large inlet subcooling respectively suppresses bubble growth and reduces the mean vapor layer thickness. Images for the highest subcooling of $\Delta T_{sub,in} = 39.28$°C are presented in Fig. 12(g). Note that the right wall is heated as opposed to the left. Similar overarching trends of condensation dominance early on in the boiling curve and the formation of a wavy vapor layer as CHF is approached are present, as seen in previous subfigures. However, significantly smaller vapor structures exist, and several wetting fronts remain along the heated wall at 100% q''_{CHF}. The large inlet subcooling preserves wetting fronts in the downstream section of the channel even as strip temperatures reach 122°C.

3.1.2 Flow Patterns for Fixed High Inlet Subcooling and High Inlet Pressure – Effects of Mass Velocity and Heat Flux

Fig. 13 shows images recorded at increasing heat fluxes along the boiling curve for a high inlet subcooling of $\Delta T_{sub,in}$ = 28.44 – 29.76°C and different mass velocities. Fig. 13(a) displays images for the lowest mass velocity of G = 201.45 kg/m^{2}s. At 22.81% q''_{CHF}, an initial upstream single-phase liquid length precedes ONB, after which, the high degree of subcooling prevents significant bubble growth along the channel. Increasing the heat flux further grows the thermal boundary layer and activates additional nucleation sites promoting bubble coalescence and growth. At 57.51% q''_{CHF}, bubbles periodically grow to fill the channel's entire cross section. In between large bubbles, nucleation sites exist at which bubbles form, grow slightly, and condense back to liquid. In the following image corresponding to 68.23% q''_{CHF}, the vapor structures in the channel more closely resemble a wavy vapor layer where wetting fronts are present along the heated wall, allowing liquid access. Even at a high degree of inlet subcooling, vapor patches are able to grow large enough to reach the opposite wall. This is due to the relatively low mass velocity permitting the bulk fluid to accumulate sufficient heat, reducing the effects of subcooling downstream. Vapor patches continue to grow, and downstream wetting fronts shift further upstream with increasing heat flux.

Fig. 13(b) shows images for a higher mass velocity of G = 402.07 kg/m^{2}s. At 15.52% q''_{CHF}, temporal strip-temperature records indicate ONB occurred, however, bubble nucleation at the wall is not clear. Bubble nucleation is faintly visible along the heated wall at the following increment, q''_w = 23.48% q''_{CHF}, as the thermal boundary layer thickens and promotes bubble growth. As the thermal boundary layer thickens, the condensing potential of the subcooled liquid becomes weaker at larger distances from the wall, leading to effective positive evaporation and bubble growth. At 56.60% q''_{CHF}, increased bubble coalescence results in larger bubbles sliding along the heated wall. Similar to the previous subfigure, at 57.51% q''_{CHF}, bubbles occasionally coalesce and grow to the size of the channel's cross section. The large bubbles convect out of the channel and are followed by a section of liquid containing many smaller bubbles along the wall. Increasing the heat flux towards CHF results in growth of the wavy vapor layer, however, at this elevated flow rate, significantly less vapor is present in the channel than observed in Fig. 13(a), specifically near CHF. Notice at 94.28% q''_{CHF}, outlet quality is unusually high (as reported within the figure) due to outlet pressure fluctuations varying the local saturation temperature. Similar results were observed during Earth-gravity experiments [57]. Fig. 13(c) shows a set of images for G = 801.60 kg/m^{2}s, also shown in Fig. 12(f). For this case, nucleation does not become clearly visible until 37.33% q''_{CHF}. Subsequent increases in heat flux advance the ONB location further upstream and thicken the vapor layer. At 81.57% q''_{CHF}, the wavy vapor layer develops and

remains in the channel until CHF. In both Figs. 13(d) and (e), respectively corresponding to mass velocities of G = 1599.92 and 2400.00 kg/m^{2}s, vapor layers appear much thinner than those observed at lower G. This is due to the increased shear stresses thinning the vapor layer. Also evident in Fig. 13(e) depicting the combination of high subcooling and flow rate, is the distinct single-phase liquid length upstream, even at CHF. For this case, CHF occurs downstream where a sufficiently large vapor patch locally prevents cooling, causing strip temperatures to reach 122°C.

3.1.3 Flow Patterns for Fixed Low Inlet Subcooling and High Inlet Pressure – Effects of Mass Velocity and Heat Flux

Fig. 14 shows images recorded along the boiling curve at different mass velocities with a lower inlet subcooling of $\Delta T_{sub,in}$ = 2.93 – 4.54°C. Fig. 14(a) shows images for the lowest mass velocity of G = 200.05 kg/m^{2}s. At 32.46% q''_{CHF}, ONB occurs near the upstream edge of the heated wall. The bubble layer grows in the flow direction as the combination of low mass velocity and low subcooling is favorable for developing the thermal boundary layer and promoting bubble growth. In the downstream section of the channel, bubbles grow large and detach from the heated wall. The bubble layer becomes thicker and bubble size increases with increasing heat flux. At 63.66% q''_{CHF}, large vapor patches constitute a wavy vapor layer with nucleation sites occurring in the liquid sublayer between the vapor and heated wall. This is still observed at 74.39% q''_{CHF}, where a secondary vapor layer forms beneath the most downstream vapor structure. This phenomenon is suppressed at 85.46% q''_{CHF}, and a fairly continuous vapor layer occupies the channel as any remaining wetting fronts are pushed upstream. Regardless of the majority of the channel being occupied by vapor at both 85.46% and 96.35% q''_{CHF}, CHF is prevented by heat conducting axially upstream to available wetting fronts, wherein nucleate boiling persists, and the periodic voyage of wetting fronts further downstream. At 100% q''_{CHF}, no wetting fronts remain on the heated wall and the heat transfer mechanism transitions to film boiling, where phase change occurs as evaporation of the liquid-vapor interface away from the heated wall.

At a mass velocity of G = 399.95 kg/m^{2}s, depicted in Fig. 14(b), bubble nucleation is relatively mild at ONB, q''_w = 11.65% q''_{CHF}. However, due to the low degree of subcooling, further increases in heat flux rapidly grow the bubble layer and by 32.53% q''_{CHF}, large bubbles detach from the heated wall in the downstream part of the channel. At 51.17% q''_{CHF}, large vapor patches along the wall start to form the continuous wavy vapor layer seen at higher heat fluxes. Wetting fronts are brought upstream with increasing heat flux and are only observed near the upstream edge of the heated length at 100% q''_{CHF}. Fig. 14(c) shows flow visualization for a mass velocity of G = 799.70 kg/m^{2}s. ONB is first recorded at 14.39% q''_{CHF}, and the number of activated cavities grows with ensuing increases in heat flux. Increased flow inertia and shear forces contain

the bubbles mostly to the near-wall region, resulting in a thinner, denser bubble layer than seen at lower flow rates. Bubble coalescence eventually leads to formation of the wavy vapor layer at 44.40% q''_{CHF}. Approaching CHF, the vapor layer grows considerably in the downstream region, restricting access to the heated wall. Similar results are seen in Figs. 14(d) and (e), for G = 1599.94 and 2400.00 kg/m^{2}s, respectively. Bubble nucleation becomes increasingly suppressed in the bubbly flow regime, and vapor layers are thinner compared to lower flow rates. The most notable difference is the increased complexity of downstream vapor structures. The downstream region appears relatively dark and more textured than those seen at lower flow rates, indicating liquid presence within the vapor patch caused by turbulent mixing at higher flow rates. The addition of liquid in the downstream vapor layer aids in cooling the heated wall and delays CHF.

3.1.4 Flow Patterns for Fixed Low Inlet Subcooling and Low Inlet Pressure – Effects of Inlet Pressure

Fig. 15 also shows results for a relatively low subcooling, $\Delta T_{sub,in}$ = 3.52 – 6.43°C, but at a lower pressure of p_{in} = 130.43 – 133.98 kPa, compared to p_{in} = 150.73 – 152.88 kPa in Fig. 14. The inlet subcooling range at the lower pressure is slightly higher due to difficulties in maintaining a single-phase liquid inlet. This is most pronounced in Fig. 15(a) featuring the lowest mass velocity of G = 199.97 kg/m^{2}s, and highest subcooling of $\Delta T_{sub,in}$ = 6.43°C. Comparing this image to its corresponding flow rate in Fig. 14(a), smaller bubbles are featured early on in the boiling curve, and shorter vapor patches exist approaching CHF. However, these differences are characteristics of increased subcooling and may not be attributed exclusively to the lower pressure. Less differences are noticeable between the flow patterns experienced at higher mass velocities for lower pressure, Figs. 15(b)-(e), and higher pressure, Figs. 14(b)-(e). Little differences are observed in the flow patterns along the boiling curve between the two figures, respectively resulting in similar q''_{CHF} for similar flow rates.

Overall, for the tested operating conditions, the effects of varying inlet pressure on observed flow physics are less significant compared to the influences of flow inertia and subcooling.

3.2 Flow Visualization Image Sequences

3.2.1 Flow Visualization Image Sequences for Fixed Moderate Mass Velocity – Effects of Inlet Subcooling and Heat Flux

Sequential flow images for an intermediate mass velocity of G = 799.96 – 801.75 kg/m^{2}s are presented in Fig. 16. The time elapsed between successive images is selected to capture key flow characteristics and is mentioned below each set of images. Fig. 16(a) shows image sequences

at a low inlet subcooling of $\Delta T_{sub,in}$ = 2.11°C. Beginning with the images recorded at 67.30% q''_{CHF}, the initial image shows ONB at the upstream edge of the heated wall leading into a continuous wavy vapor layer that grows along the channel length. However, boiling is still observed downstream within wetting fronts. As time progresses, the wetting front initially just halfway along the channel slides along the heated wall in the flow direction. Boiling within wetting fronts is assumed to be the primary source of cooling for the heated wall. As the wetting front advects out of the channel, new wetting fronts form upstream. At 91.97% q''_{CHF}, the wavy vapor layer immediately develops at the upstream edge of the channel and grows in the streamwise direction with periodic wetting fronts along the heated wall. Similar to the lower heat flux, wetting fronts move along the heated wall, exiting the channel and being replaced by wetting fronts upstream. As intense boiling occurs within wetting fronts, they accelerate along the heated wall, evident by the lengthening of vapor patches with time, as downstream wetting fronts separate themselves from those upstream.

Fig. 16(b) depicts images for an intermediate subcooling of $\Delta T_{sub,in}$ = 9.58°C. In both sets of images, a singular lengthy vapor structure is shown exiting the channel. These are followed by shorter waves of vapor and wetting fronts to cool the heated wall. As the distinct waves of vapor pass, they are replaced by another surge of vapor blanketing the heated wall downstream. Eventually, another elongated vapor structure forms, and moves through the channel. The cycle repeats more frequently at the higher heat flux, which shows images with shorter time increments. At the higher heat flux of 86.01% q''_{CHF}, the wavy vapor layer initiates farther upstream and the vapor layers grow thicker downstream than at 64.09% q''_{CHF}.

Flow sequences with a high degree of subcooling, $\Delta T_{sub,in}$ = 34.62°C with the right wall heated, are shown in Fig. 16(c). Note that images at 68.71% q''_{CHF} feature a relatively coarse temporal resolution of 9 ms, while images of 85.80% q''_{CHF} have a finer resolution of 2.5 ms. At 68.71% q''_{CHF}, a clear upstream single-phase length exists, after which, ONB occurs, and individual bubbles form along the wall. Bubbles do not detach from the wall, and some bubbles condense as they slide downstream, due to the high degree of subcooling. Following the downstream vapor layer in time, the elongated vapor patch convects out of the channel as shorter vapor patches move downstream. In a periodic manner, these are followed by another relatively long continuous wave of vapor. The flow patterns observed at 85.80% q''_{CHF} are more consistent than those at the lower heat flux. Compared to 68.71% q''_{CHF}, ONB occurs further upstream, and less condensation occurs as bubbles produced upstream continuously grow into the wavy vapor layer. Patches of vapor grow in an alternating fashion of thicker more pronounced waves and thinner vapor patches (thinner meaning smaller perpendicular to the heated wall). In the channel

downstream, consecutive vapor patches merge together as seen from the vapor exiting the channel in the images early on in the sequence and again towards the end of the sequence.

3.2.2 Flow Visualization Image Sequences for Fixed High Inlet Subcooling – Effects of Mass Velocity and Heat Flux

Time sequential images for a high degree of subcooling, $\Delta T_{sub,in}$ = 28.44 – 29.76°C, at different mass velocities are shown in Fig. 17. At a low G = 201.45 kg/m^{2}s, shown in Fig. 17(a), ONB occurs near the upstream edge of the heated wall regardless of the high degree of subcooling. At both heat fluxes, once the vapor layer begins developing, it quickly grows to the cross-section of the channel. Increasing the heat flux accelerates the growth rate and produces a larger, more continuous vapor layer. At the lower heat flux of 68.23% q''_{CHF}, relatively large time steps capture the consistent movement and growth of the vapor patches, and the acceleration of wetting fronts along the wall. At 95.76% q''_{CHF}, a smaller time step captures a period of relatively steady flow, further discussed in section 3.3. Here, the most downstream wetting front is shown accelerating along the channel, perturbing the shape of the vapor layer. The vapor patch immediately upstream of this wetting front rapidly grows as boiling ensues, and the vapor blanket downstream continuously grows as it drifts along the heated wall. Fig. 17(b) depicts image sequences at an intermediate mass velocity of G = 801.60 kg/m^{2}s, where the increased flow inertia yields significantly smaller vapor structures in the channel. Comparing the left sets of images in Figs. 16(c) and 17(b), the flow conditions are quite similar except that the heated wall is different. In 17(b), bubbles are visible right from the upstream edge, whereas in Fig. 16(c), they are visible only from a quarter of the flow length. This difference is most probably an artifact of imaging due to the camera being more focused at the left wall, but it could also be attributed to differences in nucleation characteristics of the two heated walls. At 69.78% q''_{CHF}, a periodic flow pattern is observed, wherein, the vapor produced downstream coalesces and blankets the heated wall. Boiling upstream accelerates the flow and pushes the elongated blanket out of the channel. The flow pattern now resembles the typical periodic wavy vapor layer, in which patches of vapor are separated by distinct wetting fronts. This pattern persists until another smooth continuous vapor patch occupies the downstream portion of the channel in the final images of the sequence. Different flow patterns are observed at 91.33% q''_{CHF}, where consistent vapor production causes relatively uniform vapor patches to accelerate sliding along the wall downstream.

Image sequences for a high mass velocity of G = 2399.97 kg/m^{2}s with the right wall heated, shown in Fig. 17(c), are drastically different than the lower mass velocities. At 76.51% q''_{CHF}, a few bubbles are observed on the heated wall in the downstream portion of the channel. Bubbles condense a few milliseconds later due to the bulk fluid's high degree of subcooling, and single-

phase liquid occupies the vast majority of the channel. Increasing heat flux to 95.25% q''_{CHF}, vapor patches move quickly along the heated wall and exit the channel before growing significantly into the bulk fluid. This is a result of high inertia maintaining the subcooling of the bulk liquid, promoting condensation at the liquid-vapor interface, and shear stresses thinning the vapor layer.

3.3 Temporally Anomalous Flow Patterns for Certain Operating Conditions

Some cases experienced anomalous flow patterns caused by appreciable instabilities manifesting as flow reversal, which were mostly prominent in cases with high subcooling, low flow rate, and high heat flux. An example of this is shown in Fig. 18(a), which examines the identical case shown in Fig. 17(a), with G = 201.45 kg/m^{2}s, $\Delta T_{sub,in}$ = 29.06°C, and q''_w = 95.76% q''_{CHF}, but with 10 ms between consecutive images. The period depicted shows flow proceeding as normal with a wavy vapor layer traveling along the heated wall. This is followed by flow stagnation and reversal, where liquid re-enters the channel from the outlet. The surge of liquid flushes away most of the vapor in the channel and destroys the continuous vapor layer. Normal flow resumes, and typical vapor structures are observed in the channel just before the instability manifests again. The cycle restarts once flow reversal begins again at the end of the shown period.

Fig. 18(b) contains a flow sequence during the same experiment as Fig. 18(a), but at a reduced heat flux of 57.51% q''_{CHF}. Instability at this heat flux is relatively mild and manifests as temporary flow stagnation, with no severe flow reversal disrupting the formation of vapor structures. Similarly, Fig. 18(c) shows a sequence of images at high subcooling with an elevated mass velocity of G = 1599.92 kg/m^{2}s. Even at a high heat flux of 95.88% q''_{CHF}, the severity of flow reversal is relatively minor. Flow proceeds forward prior to flow reversal stagnating vapor near the channel's outlet. Flow inertia is able to prevent the reversing liquid from propagating further upstream and interfering with vapor production. After sufficient time, typical flow resumes, and vapor exits the channel.

The severity of the instability's effect on flow pattern increases with increasing heat flux and decreasing mass velocity (meaning increasing Boiling number), but the trend of frequency is not as clear. In some cases, the frequency of backflow is non-uniform, or the time period of flow reversal is greater than 1 s and cannot be determined in the 1 s of video recorded for each heat increment.

4. Heat Transfer Results and Discussion

In this section, heat transfer results in terms of flow boiling curves, streamwise profiles of both wall temperature and heat transfer coefficient, and trends of both local and average heat transfer coefficients, are reported and discussed.

4.1 Flow Boiling Curves

Boiling curves accurately depict the overall heat transfer performance of two-phase thermal management systems with boiling. All flow boiling curves included in this study are plotted as the average wall heat flux, q''_w, versus the average wall superheat defined as average wall temperature minus inlet saturation temperature, $\overline{T}_w - T_{sat,in}$.

Boiling curves trace the evolution of wall superheat as wall heat flux in increased. The various changes in slope indicate the different transition points between flow boiling regimes. Consider either of the two boiling curves shown in Fig. 19(a). Starting from the lowest heat flux, the second and seventh datapoints are clearly transition points due to changes in the slope, with the second typically representing the Onset of Nucleate Boiling (ONB; although not entirely correct in this case, as will be discussed below) and the seventh Onset of Nucleate Boiling Degradation (ONBD). Note that, as already mentioned, this study focusses on the nucleate boiling heat transfer regime, which lies in between ONB and CHF. Although during data processing (detailed in section 2), only heat flux increments with two-phase flow within the channel are extracted, an ONB-like point is seen in Fig. 19(a). This is due to the curves being representative of averaged values along the channel length and not a single streamwise location. Had these been local curves, the region between datapoints 1 and 2 would have represented pure liquid forced convection all along the channel. The same region for the averaged curves in Fig. 19(a) indicates a larger contribution of sensible heat over latent heat to overall heat transfer. For instance, consider a case where ONB occurs near the channel exit with single-phase convection upstream of it and partially developed boiling (PDB) downstream of it; sensible heat would contribute the most to overall heat transfer in the channel. The ONB-like point in Fig. 19(a) is in fact where latent heat starts overshadowing the effects of forced convection to overall heat transfer.

Past the ONB-like point, the curve's slope increases, and the curve once again becomes almost linear; this region corresponds to nucleate boiling, where large increases in heat flux result in small wall temperature increases. This benefit ends at the point of ONBD, which is defined as the heat flux until which the slope of the boiling curve is linear and large and after which the slope is significantly reduced (note that some studies, particularly on saturated flow boiling, have defined ONBD as *dryout incipience*) [9,75]. Between the ONBD and CHF points lie the Nucleate Boiling Degradation (NBD) region [60], where small increases in heat flux produce much larger wall temperature increases due to intermittent wall insulation and reduced liquid access to the heated wall. This is seen in the form of wetting fronts in the flow visualization images reported in section 3. The curve is terminated at CHF, where nucleate boiling is significantly degraded, and the boiling regime transitions to film boiling due to complete extinguishment of wetting fronts. This

is typically associated with increases in wall temperatures due to phase change occurring at the liquid-vapor interface of a vapor film, which insulates the heated walls. Note that in these experiments, wall heating is terminated at CHF (*viz*., 122°C measured by any of the wall thermocouples); film boiling is therefore never encountered in the experiments.

4.1.1 Symmetry of Flow Boiling and Repeatability of Experiments

Since the FBM comprises two separate heated walls, the heat transfer symmetry of the present set of experiments can be deduced from the boiling curves shown in Fig. 19(a) for a representative case. For identical operating conditions, either wall 1 (left) or wall 2 (right) was heated, and the resulting data analyzed. Overall, the two boiling curves overlap, with similar curvatures and transition points. Note the slightly different heat flux increments used for the two cases. This results in q''_{CHF} being slightly different, with wall 1 yielding a larger value than wall 2 purely due to a large CHF isolation error for wall 1's experiment (*i.e*., the heat flux increments for wall 1 were coarser when CHF incurred). These aspects suggest flow boiling is indeed symmetrical about the central plane separating the two heated walls with negligible bias be it due to the gravitational field (as expected due to negligible body forces in microgravity) or preferential bubble production at each wall (both copper strips were treated in the same manner during construction). Due to practical limitations associated with the two heater power controllers (one for each wall) and the high-speed camera being slightly more focused at wall 1 rather than 2, most single-sided-heating experiments were conducted by heating wall 1 and fewer by heating wall 2.

Repeatability of the present experiments is shown in Fig. 19(b) for a representative case. For the same set of operating conditions, experiments were repeated by heating the same wall (left, 1) on two days with an interval of two months (expt.# 2135 and 3135 were respectively performed on March 14, 2022, and May 16, 2022, with several other cases between them). The boiling curves almost perfectly overlap until the ONBD point, beyond which the curves deviate, albeit insignificantly. q''_{CHF} is almost the same, with the slight difference attributed to slight differences in heat flux increments leading up to CHF. This proves the present set of experiments are indeed repeatable on different days and the heated wall did not significantly change its boiling characteristics over two months of experimentation.

4.1.2 Mass Velocity Effects

The effects of mass velocity are shown in the boiling curves in Fig. 20 for six different sets of operating conditions (on the left and right columns are low and high inlet pressures, respectively, and from the top to bottom row is increasing inlet subcooling). On each plot are shown boiling curves for mass velocities from $G \approx 200$ to a maximum of 3200 kg/m^{2}s. In the first row left plot,

all curves perfectly overlap until ONBD. The heat flux at which ONBD occurs monotonically increases as mass velocity is increased, which leads to higher q''_{CHF} at higher G. These are due to higher G being able to sustain nucleate boiling for longer time by effectively removing the produced vapor from the channel. Due to the absence of significant body forces in microgravity, flow inertia plays the most important role in supplying the heated walls with fresh liquid for nucleate boiling. It can also be seen that q''_{CHF} is not augmented at the same rate as G is increased. For example, in the second row left plot, increasing G from 200 to 3200 kg/m^{2}s, a 1500% increase, augments q''_{CHF} by only 207.53% from 12.61 to 38.78 W/cm^2. An inference of these results is that practical thermal management systems should be optimized by weighing the q''_{CHF} augmentation to both the much higher pumping power and larger flow loop components required for higher flow rates.

These trends are similar for all six sets of operating conditions. The main difference is some high G curves have a different behavior prior to the ONB-like point, with a lower wall superheat at similar heat fluxes. This is noticeable in both ~15°C subcooling plots in the second row of Fig. 20; especially observe the curves for $G \approx$ 2400 and 3200 kg/m^{2}s. At high degrees of inlet subcooling (~30°C), as shown in the bottom row of Fig. 20, the nucleate boiling portions of the curves are also slightly different. As G is increased, the curves are seen to entirely shift towards the left, meaning wall superheat is lower for similar heat fluxes. This is probably due to mass velocities playing a larger role in determining the local subcooling at ~30°C (where subcooling plays a larger role on overall heat transfer) as opposed to 4°C (where the fluid is already very close to saturation at the inlet and becomes fully saturated shortly after entering the channel's heated section).

An anomalous feature is the curves for $G \approx$ 400 kg/m^{2}s at 30°C inlet subcooling showing a zig-zag pattern at higher heat fluxes. Also interesting in Fig. 20 are the curves for $G \approx$ 200 and 800 kg/m^{2}s at 30°C inlet subcooling showing sudden step changes in the wall superheat range of ~12-25°C. Both of these features are due to significant flow reversals at these operating conditions resulting in significant wall temperature oscillations (refer to section 3.3 for a discussion based on flow visualization). Since the plotted datapoints are obtained by averaging only 20 s of temporal data after the system enters a quasi-steady state, T_w fluctuations create a bias in the averaged T_w data. However, barring these fluctuations, the boiling curves do show the same overall trends. Analysis of these two-phase flow instabilities is outside the scope of this study and will possibly be addressed in the future.

4.1.3 Inlet Pressure Effects

The effects of inlet pressure are seen in the boiling curves shown in Fig. 20. For all operating conditions, there are no significant differences in the heat transfer performance when p_{in} is varied. Note that the two inlet pressures tested in this study are fairly close to each other to induce any significant thermophysical property variations, however the saturation temperature differs by ~7°C. Also note that, in section 3.1.4 comparing Figs. 14 and 15, it is already discussed that p_{in} does not play a major role in deciding the flow patterns.

4.1.4 Subcooled Inlet Conditions – Inlet Subcooling Effects

The effects of inlet subcooling are shown in the boiling curves in Fig. 21(a), (b), and (c) for three mass velocities of $G \approx 200$, 800, and 2400 kg/m^{2}s, respectively. In each plot, inlet subcooling is varied in the range of $\Delta T_{sub,in} \approx 45 - 2$°C (the actual obtained subcooling values are slightly different than the desired values). In Fig. 21 (a), for the lowest G, the boiling curves prior to ONBD are almost on top of one another with the curves slightly moving towards the left as $\Delta T_{sub,in}$ is increased. Higher $\Delta T_{sub,in}$ causes most of the channel length to undergo locally subcooled flow boiling, rather than saturated flow boiling.

q''_{ONBD} and hence q''_{CHF} are larger at higher inlet degrees of subcooling due to the enhanced capability of the fluid to condense the produced vapor back to liquid as well as absorb heat to raise its temperature. The former results in smaller vapor structures and more opportunities for liquid contact with the heated wall. Note that, some boiling curves in Fig. 21, especially the ones at high mass velocities and high inlet subcoolings, were terminated prior to reaching CHF, for two reasons: (i) q''_{CHF} was much larger than the power capabilities of the experimental system connected to the ISS and (ii) the experiments were prematurely terminated to safeguard the system from severe flow instabilities.

These trends are also observed in Figs. 21 (b) and (c) and thus the effects of $\Delta T_{sub,in}$ are similar at all mass velocities. An interesting aspect of high G that distinguishes Fig. 21(c) from Figs. 21(a) and 21(b) is the much broader region between local ONB observance and latent heat significance over sensible heat, *i.e.*, the negative values on the horizontal axis. This could be due to the combinations of higher G and higher $\Delta T_{sub,in}$ resulting in longer lengths of single-phase liquid convection and PDB, and much shorter or even no FDB region [57,74]. Note that PDB has bubble nucleation, but the heat transfer performance is closer to single-phase convection, whereas FDB has much larger void fraction increases and latent heat significantly dominates over sensible heat transfer with a performance similar to pure saturated boiling. This combination of operating conditions offers the strongest condensation effects, quickly collapsing any nucleated bubbles and deferring NVG to higher heat fluxes.

One effective way to significantly augment the upper limit of cooling (CHF) of the thermal management system is to increase the inlet subcooling. From the literature [7], it is known that increase inlet subcooling also yields reduced pressure drop and pumping power requirements due to them being lower for subcooled flow boiling compared to saturated flow boiling with a significant void fraction. An inference is the energy cost for establishing higher degrees of inlet subcooling as well as system instabilities need to be considered during practical system design. An optimized combination of increasing both the flow rate and the inlet subcooling could be utilized to augment the system's cooling capability.

4.2 Local Wall Temperature

Streamwise profiles of local wall temperature ($T_{w,z}$) are shown in Fig. 22 for eight representative sets of operating conditions. The plots on the left correspond to highly subcooled inlet (~30°C) and those on the right to near-saturated inlet (~4°C); respectively arranged from the top to bottom are combinations of low mass velocity (G) and low inlet pressure (p_{in}), moderate G and low p_{in}, high G and low p_{in}, and high G and high p_{in}. Included in each plot are steady-state $T_{w,z}$ profiles at six heat fluxes ranging between ONB and CHF, noted as percentages of q''_{CHF}.

In all the plots, at each of the seven streamwise locations, T_w monotonically increases with increasing heat flux. There are slight exceptions (for example, see the left plot in row 1; the first location does not show a monotonic trend) which could be due to slight flow instabilities in the 20-s averaging period producing atypical average T_w datapoints. The T_w profiles are almost flat at lower heat fluxes indicating an isothermal wall. As heat flux increases, the T_w profiles become more curved with a concave-downward shape consisting of lower T_w near the inlet and outlet and higher T_w in the middle. T_w is lowest near the inlet due to the fluid's highest degree of subcooling amongst all locations and thermal entrance effects. T_w increases thereafter due to (i) higher fluid temperatures resulting from the fluid's eventual heat gain, (ii) reduced thermal boundary layer development effects, and (iii) formation of a wavy vapor layer atop the heating wall. In the absence of significant body forces, the bulk fluid accelerates solely due to increased void fraction increasing the specific volume. This acceleration is relatively small when compared to vertical upflow in Earth gravity, where buoyancy aids flow acceleration. Acceleration causes the local flow velocity to increase downstream, resulting in enhanced convective heat transfer, increased turbulence, and quicker removal of vapor from the channel, which all contribute to a reduction in local T_w. In fact, the peak T_w signifies the location where acceleration starts to dominate over the development effects. As seen in Fig. 10(a) and prior studies [30,31,57], the T_w maxima close to CHF indicates the location where CHF first manifests. Both the highly subcooled and near-saturated plots in Fig. 22 show, for low G and low p_{in}, T_w peaks near the exit between measurement

locations 5 and 6 (see Fig. 8(c)), whereas for all other operating conditions, T_w peaks around the middle of the channel between measurement locations 3 and 5. This is attributed to low G increasing the fluid's residence time within the channel, meaning the fluid has absorbed much heat leading to high void fractions and CHF manifestation downstream. Between highly subcooled and near-saturated inlet in Fig. 22, particularly at high G (rows 3 and 4), T_w peaks sharply for highly subcooled inlet and is relatively rather flat and blunt for near-saturated inlet; also, the T_w minima at the upstream end are lower for highly subcooled inlet. This is attributed to the fluid being close to or at the saturation temperature for the majority of the heated length for near-saturated inlet, whereas for highly subcooled inlet, the fluid temperature is minimum at the inlet and gradually increases downstream.

A practical design aspect of the FBM contributing to the lower T_w at the ends of the heated wall is the slightly extended heat transfer surface area covered by the end resistors leading to reduced local heat fluxes at the ends compared to the almost uniform heat flux maintained for the majority of the heated length.

4.3 Local Heat Transfer Coefficient

4.3.1 Streamwise Local Heat Transfer Coefficient Profiles

Streamwise profiles of local heat transfer coefficient (h_z) are shown in Fig. 23 for the same eight representative sets of operating conditions as Fig. 22 with the layouts of both these figures similar to each other.

For highly subcooled inlet (left column), the h profiles are almost flat at lower heat fluxes meaning a uniform heat transfer performance along the heated length. This is due to the large condensation effects of the bulk fluid sustaining liquid convection and subcooled PDB regimes (see Fig. 13 for flow visualization images for highly subcooled inlet). At higher heat fluxes, the profiles are curved with a concave-upward shape with a decrease near the entrance, almost constant at the middle, and an increase near the exit. The reasons for the upstream decrease and downstream increase are identical to the discussion for T_w profiles in section 4.2; the upstream decrease is due to thermal boundary layer and bubble boundary layer effects and the upstream increase is due to flow acceleration effects. For high G (row 3), the first two upstream locations have h monotonically increasing with increasing heat flux. Generally, as heat flux is increased, h first increases until a certain heat flux, where it faces nucleate boiling degradation, after which it decreases with heat flux. The first increase is due to increased contribution of latent heat transfer and flow acceleration effects. The latter decrease is due to the formation of thick vapor layer along the heated wall and extinguishment of wetting fronts. Even though the overall h profiles at high heat fluxes are degraded, flow acceleration effects still enhance heat transfer downstream.

The profiles for near-saturated inlet (right column in Fig. 23) follow similar trends. The h profiles close to CHF are much more degraded than highly subcooled inlet; see how for low G (row 1), the 95.04% q''_{CHF} profile lies below all other profiles downstream of the third streamwise location. Even though high G is more effective in removing the produced vapor from the channel, the higher G plots (rows 2-4) show similar degraded h profiles at high heat flux percentages (but the actual heat flux values are much larger). Relatively, the h values are higher for near-saturated inlet due to the fluid being near or at saturation, meaning a reduced temperature difference between the fluid and the wall for similar heat fluxes.

4.3.2 Local Heat Transfer Coefficient Variations with Local Thermodynamic Equilibrium Quality

Variations of local heat transfer coefficient (h_z) with local thermodynamic equilibrium quality (x_e) are shown in Fig. 24, which maintains the same layout and representative sets of operating conditions as Fig. 22 and 23. Due to x_e being significantly affected by the choice of operating conditions ($\Delta T_{sub,in}$, G, p_{in}), the horizontal axis limits of each plot are different. Note that x_e is the thermodynamic equilibrium quality estimated from measured parameters and not the measured flow quality, x. $x \approx x_e$ is only for near-saturated or saturated conditions at the inlet. Most other conditions have a negative x_e throughout the channel, despite a positive x due to large thermodynamic non-equilibrium at any cross-section. These mean it is possible to have entirely different x, flow patterns, heat transfer mechanisms, and h_z for the same x_e.

For highly subcooled inlet (left column in Fig. 24), the curves are rather flat at lower x_e and h_z almost increases with increasing heat flux, both aspects due to the dominant nucleate boiling regime. Above a certain x_e, the h_z curves are still flat, but almost independent of heat flux (*i.e.*, they overlap in this region), beyond which, h_z increases with increasing x_e, both due to the dominant convective boiling regime (*i.e.*, liquid film evaporation regime). The flat curves at high heat fluxes and high x_e are the result of combined effects of convective boiling and degradation due to intermitted dryout patches, the former enhancing h_z and the latter degrading h_z.

For near-saturated inlet (right column in Fig. 24), the effects of nucleate boiling dominance at lower x_e and convective boiling dominance at higher x_e still hold, but the other effects already discussed (upstream decrease due to thermal entrance effects, downstream increase due to acceleration effects, and both possibly due to the extended surface area served by the end resistors) are also important factors in deciding the trends. Note that practical experimental difficulties in maintaining x_e constant for near-saturated inlet with high G (rows 3 and 4) along with the small x_e increase along the channel complicate interpreting any trends of h_z versus heat flux.

4.4 Average Heat Transfer Coefficient

Variations of average heat transfer coefficient ($\bar{h}$) with wall heat flux are shown in Fig. 25 for six different representative sets of operating conditions. Respectively shown on the left and right columns are plots for low and high inlet pressures, and from the top to bottom row are ~30°C, 15°C, and 4°C inlet subcoolings. Included in each plot are curves for three different mass velocities of $G \approx 200$, 800, and 2400 kg/m^{2}s. For all three inlet subcoolings, upon comparing the plots in the left and right columns, it can be seen that inlet pressure does not have a significant effect on the heat transfer coefficient or its parametric trends.

For highly subcooled 30°C inlet (row 1 in Fig. 25), the $\bar{h}$ curves are characterized by three different regions: (i) an almost linear and broad increasing region at lower heat fluxes, (ii) a peak at some intermediate heat flux, and (iii) a decrease until a minimum at q''_{CHF}. The initial $\bar{h}$ increase is due to effective nucleate boiling and the increased contribution of latent heat to overall heat transfer. As expected, the curves overlap in this region. The $\bar{h}$ peak corresponds to ONBD, after which nucleate boiling becomes less effective due to reduced access of liquid to the heated wall. Finally, $\bar{h}$ sharply decreases to a minimum at CHF due to transition to film boiling with severely poor heat transfer performance. These trends also apply to near-saturated inlet (row 3), with the following differences: (i) the initial increasing region is slightly less linear and narrow and (ii) a much broader region post the $\bar{h}$ peak. These are both due to the near-saturated fluid offering almost no condensation of produced vapor, leading to the attainment of ONBD at lower heat fluxes.

The peak $\bar{h}$ value itself follows different trends at different inlet subcoolings. For highly subcooled inlet (rows 1 and 2), the peak $\bar{h}$ value increases with increasing G, and the highest peak $\bar{h}$ is obtained for the highest G = 2400 kg/m^{2}s, whereas for near-saturated inlet (row 3), both G = 800 and 2400 kg/m^{2}s yield the same highest peak $\bar{h}$ value, albeit at different heat fluxes. Between the highly subcooled and near-saturated inlets, the latter yields higher $\bar{h}$ values than the former due to nucleate boiling reducing the temperature difference between the saturated fluid and wall. On the contrary, for highly subcooled inlet, the bulk fluid temperature is much lower than saturation, but the wall temperature needs to be a certain amount larger than saturation to sustain nucleate boiling; this large difference between T_w and T_f leads to lower $\bar{h}$. Despite the lower $\bar{h}$ values, highly subcooled inlet does offer a significantly higher cooling limit (q''_{CHF}) while keeping system temperatures under a safe low threshold.

Overall, although their values might be different, the parametric trends of the various heat transfer parameters are very similar in a microgravity environment as already established for vertical upflow in Earth gravity [57].

5. Conclusions

This study explored microgravity flow boiling of nPFH in a rectangular channel with single-sided heating for subcooled inlet conditions. The experiments were conducted for ~5 months onboard the International Space Station (ISS) using NASA's Flow Boiling and Condensation Experiment (FBCE) equipped with the Flow Boiling Module (FBM). High-speed-video flow visualization of the FBM's heated section was done for all operating conditions, and the resulting images and image sequences were presented to explain the flow patterns and temporally evolving interfacial features. Heat transfer results were presented in terms of flow boiling curves, streamwise profiles of wall temperature and heat transfer coefficient, and parametric trends of local and averaged heat transfer coefficients.

The effects of various parameters including mass velocity, inlet subcooling, and inlet pressure, on the heat transfer and flow physics of flow boiling in microgravity were clearly established throughout the broad ranges of operating conditions. Key observations are summarized in Table 5, which presents the typical parametric effects on several aspects considered in this study, including the interfacial flow physics, local wall temperature, both local and average heat transfer coefficients, ONBD, and CHF. Mass velocity and inlet subcooling significantly influenced most aspects, whereas inlet pressure had the least significant effect. Albeit the actual values of heat transfer parameters and observed flow physics might be different, the parametric trends are similar for flow boiling in microgravity as for vertical upflow boiling in Earth gravity.

Some experimental cases experienced temporally anomalous behaviors caused by two-phase flow instabilities manifesting as flow reversals and resulted in deviations in parametric trends. These were more prominent at low mass velocities, high heat fluxes, and large degrees of inlet subcooling. Severe thermodynamic non-equilibrium was also observed throughout the channel.

Overall, FBCE's ISS experiments were highly successful for subcooled inlet with single-sided heating of the rectangular channel, and the collected data well established the various effects on flow boiling physics in highly controlled long-term microgravity conditions.

CRediT author contribution statement – **I. Mudawar**: Conceptualization, Methodology, Supervision, Writing – review and editing, Funding acquisition. **V.S. Devahdhanush**: Methodology, Software, Formal analysis, Investigation, Data curation, Writing – original draft, Writing – review and editing. **S.J. Darges**: Formal analysis, Investigation, Writing – original draft. **M.M. Hasan**: Conceptualization, Investigation, Writing – review and editing. **H.K. Nahra**: Investigation, Writing – review and editing. **R. Balasubramaniam**: Investigation, Writing – review and editing. **J.R. Mackey**: Investigation, Imaging.

Declaration of Competing Interest – None. The authors declare that they have no known

competing financial interests or personal relationships that could have appeared to influence the work reported in this paper.

Acknowledgement – The authors are appreciative of the support of the National Aeronautics and Space Administration (NASA) under grant no. 80NSSC22K0328. The authors are also thankful to the FBCE personnel at NASA Glenn Research Center, Cleveland, Ohio, especially Nancy Hall (FBCE Project Manager), Rochelle May and Phillip Gonia (Software Engineering), Mark Sorrells (Assembly, Integration and Test Lead), Jesse DeFiebre (Fluids Lead), Monica Guzik (FBCE Chief Engineer), and ZIN FCF Mission Operations Team, for their dedicated technical assistance and successful completion of ISS testing.

References

[1] T.J. LaClair, I. Mudawar, Thermal transients in a capillary evaporator prior to the initiation of boiling, Int. J. Heat Mass Transf. 43 (21) (2000) 3937–3952, doi: 10.1016/S0017-9310(00)00042-9.

[2] I. Mudawar, T.M. Anderson, Parametric investigation into the effects of pressure, subcooling, surface augmentation and choice of coolant on pool boiling in the design of cooling systems for high-power-density electronic chips, J. Electron. Packag. 112 (4) (1990) 375–382, doi: 10.1115/1.2904392.

[3] C.O. Gersey, I. Mudawar, Effects of heater length and orientation on the trigger mechanism for near-saturated flow boiling critical heat flux-II. Critical heat flux model, Int. J. Heat Mass Transf. 38 (4) (1995) 643–654, doi: 10.1016/0017-9310(94)00194-Z.

[4] V.S. Devahdhanush, Y. Lei, Z. Chen, I. Mudawar, Assessing advantages and disadvantages of macro- and micro-channel flow boiling for high-heat-flux thermal management using computational and theoretical/empirical methods, Int. J. Heat Mass Transf. 169 (2021) 120787, doi: 10.1016/j.ijheatmasstransfer.2020.120787.

[5] S. Lee, V.S. Devahdhanush, I. Mudawar, Pressure drop characteristics of large length-to-diameter two-phase micro-channel heat sinks, Int. J. Heat Mass Transf. 115 (2017) 1258–1275, doi: 10.1016/j.ijheatmasstransfer.2017.08.104.

[6] S. Mukherjee, I. Mudawar, Pumpless loop for narrow channel and micro-channel boiling, J. Electron. Packag. 125 (3) (2003) 431–441, doi: 10.1115/1.1602708.

[7] V.S. Devahdhanush, S. Lee, I. Mudawar, Consolidated theoretical/empirical predictive method for subcooled flow boiling in annuli with reference to thermal management of ultra-fast electric vehicle charging cables, Int. J. Heat Mass Transf. 175 (2021) 121224, doi: 10.1016/j.ijheatmasstransfer.2021.121224.

[8] M.E. Johns, I. Mudawar, An ultra-high power two-phase jet-impingement avionic clamshell module, J. Electron. Packag. 118 (4) (1996) 264–270, doi: 10.1115/1.2792162.

[9] V.S. Devahdhanush, I. Mudawar, Critical heat flux of confined round single jet and jet array impingement boiling, Int. J. Heat Mass Transf. 169 (2021) 120857, doi: 10.1016/j.ijheatmasstransfer.2020.120857.

[10] J.R. Rybicki, I. Mudawar, Single-phase and two-phase cooling characteristics of upward-facing and downward-facing sprays, Int. J. Heat Mass Transf. 49 (1–2) (2006) 5–16, doi:

10.1016/j.ijheatmasstransfer.2005.07.040.

[11] F.P. Chiaramonte, J. McQuillen, H.K. Nahra, P. Manoharan, H. Vanhala, B.J. Motil, J. Kim, V. Carey, W.G. Anderson, J. Plawsky, L. Carter, A. Jackson, 2019 NASA division of space and life and phyiscal sciences research and applications fluid physics workshop report, Cleveland, OH, USA, 2020.

[12] J. Straub, Boiling heat transfer and bubble dynamics in microgravity, Adv. Heat Transf. 35 (2001) 57–172, doi: 10.1016/S0065-2717(01)80020-4.

[13] H. Zhang, I. Mudawar, M.M. Hasan, A method for assessing the importance of body force on flow boiling CHF, J. Heat Transfer 126 (2) (2004) 161–168, doi: 10.1115/1.1651532.

[14] C. Konishi, I. Mudawar, M.M. Hasan, Criteria for negating the influence of gravity on flow boiling critical heat flux with two-phase inlet conditions, Int. J. Heat Mass Transf. 65 (2013) 203–218, doi: 10.1016/j.ijheatmasstransfer.2013.05.070.

[15] L.E. O'Neill, I. Park, C.R. Kharangate, V.S. Devahdhanush, V. Ganesan, I. Mudawar, Assessment of body force effects in flow condensation, part II: Criteria for negating influence of gravity, Int. J. Heat Mass Transf. 106 (2017) 313–328, doi: 10.1016/j.ijheatmasstransfer.2016.07.019.

[16] T. Oka, Y. Aba, K. Tanaka, Y.H. Mori, A. Nagashima, Observational study of pool boiling under microgravity, JSME Int. Journal. Ser. 2, Fluids Eng. Heat Transf. Power, Combust. Thermophys. Prop. 35 (2) (1992) 280–286, doi: 10.1299/jsmeb1988.35.2_280.

[17] T. Oka, Y. Abe, Y.H. Mori, A. Nagashima, Pool boiling of n-pentane, CFC-113, and water under reduced gravity: Parabolic flight experiments with a transparent heater, J. Heat Transfer 117 (2) (1995) 408–417, doi: 10.1115/1.2822537.

[18] J. Kim, J.F. Benton, D. Wisniewski, Pool boiling heat transfer on small heaters: Effect of gravity and subcooling, Int. J. Heat Mass Transf. 45 (19) (2002) 3919–3932, doi: 10.1016/S0017-9310(02)00108-4.

[19] H. Ohta, Experiments on microgravity boiling heat transfer by using transparent heaters, Nucl. Eng. Des. 175 (1–2) (1997) 167–180, doi: 10.1016/S0029-5493(97)00172-6.

[20] H. Ohta, K. Kawasaki, S. Okada, H. Azuma, S. Yoda, T. Nakamura, On the heat transfer mechanisms in microgravity nucleate boiling, Adv. Sp. Res. 24 (10) (1999) 1325–1330, doi: 10.1016/S0273-1177(99)00741-3.

[21] R.R. Souza, J.C. Passos, E.M. Cardoso, Confined and unconfined nucleate boiling under terrestrial and microgravity conditions, Appl. Therm. Eng. 51 (1–2) (2013) 1290–1296, doi: 10.1016/j.applthermaleng.2012.09.035.

[22] Y.F. Xue, J.F. Zhao, J.J. Wei, J. Li, D. Guo, S.X. Wan, Experimental study of nucleate pool boiling of FC-72 on smooth surface under microgravity, Microgravity Sci. Technol. 23 (2011) 75–85, doi: 10.1007/s12217-011-9274-5.

[23] X. Wang, Y. Zhang, B. Qi, J. Zhao, J. Wei, Experimental study of the heater size effect on subcooled pool boiling heat transfer of FC-72 in microgravity, Exp. Therm. Fluid Sci. 76 (2016) 275–286, doi: 10.1016/j.expthermflusci.2016.03.031.

[24] Y. Yang, X. Chen, Y. Huang, G. Li, Experimental study on pool boiling of distilled water and HFE7500 fluid under microgravity, Acta Astronaut. 143 (2018) 362–371, doi: 10.1016/j.actaastro.2017.11.011.

[25] M. Misawa, An experimental and analytical investigation of flow boiling heat transfer under

microgravity conditions, Ph.D. thesis, University of Florida, FL, USA, 1993.

[26] C. Baltis, G.P. Celata, M. Cumo, L. Saraceno, G. Zummo, Gravity influence on heat transfer rate in flow boiling, Microgravity Sci. Technol. 24 (3) (2012) 203–213, doi: 10.1007/s12217-012-9298-5.

[27] M. Saito, N. Yamaoka, K. Miyazaki, M. Kinoshita, Y. Abe, Boiling two-phase flow under microgravity, Nucl. Eng. Des. 146 (1–3) (1994) 451–461, doi: 10.1016/0029-5493(94)90350-6.

[28] Y. Ma, J.N. Chung, An experimental study of critical heat flux (CHF) in microgravity forced-convection boiling, Int. J. Multiph. Flow 27 (10) (2001) 1753–1767, doi: 10.1016/S0301-9322(01)00031-3.

[29] H. Zhang, I. Mudawar, M.M. Hasan, Flow boiling CHF in microgravity, Int. J. Heat Mass Transf. 48 (15) (2005) 3107–3118, doi: 10.1016/j.ijheatmasstransfer.2005.02.015.

[30] C. Konishi, H. Lee, I. Mudawar, M.M. Hasan, H.K. Nahra, N.R. Hall, J.D. Wagner, R.L. May, J.R. Mackey, Flow boiling in microgravity: Part 1 – Interfacial behavior and experimental heat transfer results, Int. J. Heat Mass Transf. 81 (2015) 705–720, doi: 10.1016/j.ijheatmasstransfer.2014.10.049.

[31] C. Konishi, H. Lee, I. Mudawar, M.M. Hasan, H.K. Nahra, N.R. Hall, J.D. Wagner, R.L. May, J.R. Mackey, Flow boiling in microgravity: Part 2 – Critical heat flux interfacial behavior, experimental data, and model, Int. J. Heat Mass Transf. 81 (2015) 721–736, doi: 10.1016/j.ijheatmasstransfer.2014.10.052.

[32] S. Luciani, D. Brutin, C. Le Niliot, O. Rahli, L. Tadrist, Flow boiling in minichannels under normal, hyper-, and microgravity: Local heat transfer analysis using inverse methods, J. Heat Transfer 130 (10) (2008) 1–13, doi: 10.1115/1.2953306.

[33] D. Brutin, V.S. Ajaev, L. Tadrist, Pressure drop and void fraction during flow boiling in rectangular minichannels in weightlessness, Appl. Therm. Eng. 51 (1–2) (2013) 1317–1327, doi: 10.1016/j.applthermaleng.2012.11.017.

[34] M. Narcy, E. de Malmazet, C. Colin, Flow boiling in tube under normal gravity and microgravity conditions, Int. J. Multiph. Flow 60 (2014) 50–63, doi: 10.1016/j.ijmultiphaseflow.2013.11.011.

[35] Y. Zhang, B. Liu, J. Zhao, Y. Deng, J. Wei, Experimental study of subcooled flow boiling heat transfer on a smooth surface in short-term microgravity, Microgravity Sci. Technol. 30 (6) (2018) 793–805, doi: 10.1007/s12217-018-9629-2.

[36] B. Liu, B. Yuan, P. Xu, J. Zhao, Y. Zhang, J. Wei, Y. Yang, Q. Cao, A method for approximating the CHF of subcooled flow boiling in microgravity by ground tests, Int. J. Multiph. Flow 122 (2020) 103161, doi: 10.1016/j.ijmultiphaseflow.2019.103161.

[37] M.T. Lebon, C.F. Hammer, J. Kim, Gravity effects on subcooled flow boiling heat transfer, Int. J. Heat Mass Transf. 128 (2019) 700–714, doi: 10.1016/j.ijheatmasstransfer.2018.09.011.

[38] D.M. Iceri, G. Zummo, L. Saraceno, G. Ribatski, Convective boiling heat transfer under microgravity and hypergravity conditions, Int. J. Heat Mass Transf. 153 (2020) 119614, doi: 10.1016/j.ijheatmasstransfer.2020.119614.

[39] C. Konishi, I. Mudawar, Review of flow boiling and critical heat flux in microgravity, Int. J. Heat Mass Transf. 80 (2015) 469–493, doi: 10.1016/j.ijheatmasstransfer.2014.09.017.

[40] P. Di Marco, W. Grassi, Pool boiling in microgravity: Assessed results and open issues, in: Proc. 3rd Eur. Therm. Conf., Heidelberg, Germany, 2000, pp. 81–90.

[41] R. Raj, J. Kim, J. McQuillen, Pool boiling heat transfer on the International Space Station: Experimental results and model verification, J. Heat Transfer 134 (10) (2012), doi: 10.1115/1.4006846.

[42] H.S. Lee, H. Merte, F. Chiaramonte, Pool boiling curve in microgravity, J. Thermophys. Heat Transf. 11 (2) (1997) 216–222, doi: 10.2514/2.6225.

[43] H. Merte, Momentum effects in steady nucleate pool boiling during microgravity, Ann. N. Y. Acad. Sci. 1027 (2004) 196–216, doi: 10.1196/annals.1324.018.

[44] J.F. Zhao, G. Liu, S.X. Wan, N. Yan, Bubble dynamics in nucleate pool boiling on thin wires in microgravity, Microgravity Sci. Technol. 20 (2) (2008) 81–89, doi: 10.1007/s12217-008-9010-y.

[45] J.F. Zhao, J. Li, N. Yan, S.F. Wang, Bubble behavior and heat transfer in quasi-steady pool boiling in microgravity, Microgravity Sci. Technol. 21 (S1) (2009) 175–183, doi: 10.1007/s12217-009-9151-7.

[46] V.K. Dhir, G.R. Warrier, E. Aktinol, D. Chao, J. Eggers, W. Sheredy, W. Booth, Nucleate pool boiling experiments (NPBX) on the International Space Station, Microgravity Sci. Technol. 24 (5) (2012) 307–325, doi: 10.1007/s12217-012-9315-8.

[47] G.R. Warrier, V.K. Dhir, D.F. Chao, Nucleate pool boiling experiment (NPBX) in microgravity: International Space Station, Int. J. Heat Mass Transf. 83 (2015) 781–798, doi: 10.1016/j.ijheatmasstransfer.2014.12.054.

[48] H. Ohta, H. Asano, O. Kawanami, K. Suzuki, R. Imai, Y. Shinmoto, S. Matsumoto, T. Kurimoto, H. Takaoka, K. Fujii, M. Sakamoto, K. Sawada, H. Kawasaki, A. Okamoto, K. Kogure, T. Oka, K. Usuku, T. Tomobe, M. Takayanagi, Development of boiling and two-phase flow experiments on board ISS (Research objectives and concept of experimental setup), Int. J. Microgravity Sci. Appl. 33 (1) (2016) 330101, doi: 10.15011/ijmsa.33.330102.

[49] K. Inoue, H. Ohta, Y. Toyoshima, H. Asano, O. Kawanami, R. Imai, K. Suzuki, Y. Shinmoto, S. Matsumoto, Heat loss analysis of flow boiling experiments onboard International Space Station with unclear thermal environmental conditions (1st Report: Subcooled liquid flow conditions at test section inlet), Microgravity Sci. Technol. 33 (2) (2021) 28, doi: 10.1007/s12217-021-09869-5.

[50] K. Inoue, H. Ohta, H. Asano, O. Kawanami, R. Imai, K. Suzuki, Y. Shinmoto, T. Kurimoto, S. Matsumoto, Heat loss analysis of flow boiling experiments onboard International Space Station with unclear thermal environmental conditions (2nd Report: Liquid-vapor two-phase flow conditions at test section inlet), Microgravity Sci. Technol. 33 (5) (2021) 57, doi: 10.1007/s12217-021-09902-7.

[51] A. Sielaff, D. Mangini, O. Kabov, M.Q. Raza, A.I. Garivalis, M. Zupančič, S. Dehaeck, S. Evgenidis, C. Jacobs, D. Van Hoof, O. Oikonomidou, X. Zabulis, P. Karamaounas, A. Bender, F. Ronshin, M. Schinnerl, J. Sebilleau, C. Colin, P. Di Marco, T. Karapantsios, I. Golobič, A. Rednikov, P. Colinet, P. Stephan, L. Tadrist, The multiscale boiling investigation on-board the International Space Station: An overview, Appl. Therm. Eng. 205 (2022) 117932, doi: 10.1016/j.applthermaleng.2021.117932.

[52] C.R. Kharangate, L.E. O'Neill, I. Mudawar, M.M. Hasan, H.K. Nahra, R. Balasubramaniam, N.R. Hall, A.M. Macner, J.R. Mackey, Flow boiling and critical heat

flux in horizontal channel with one-sided and double-sided heating, Int. J. Heat Mass Transf. 90 (2015) 323–338, doi: 10.1016/j.ijheatmasstransfer.2015.06.073.

[53] C.R. Kharangate, I. Mudawar, M.M. Hasan, Experimental and theoretical study of critical heat flux in vertical upflow with inlet vapor void, Int. J. Heat Mass Transf. 55 (1–3) (2012) 360–374, doi: 10.1016/j.ijheatmasstransfer.2011.09.028.

[54] C.R. Kharangate, L.E. O'Neill, I. Mudawar, M.M. Hasan, H.K. Nahra, R. Balasubramaniam, N.R. Hall, A.M. Macner, J.R. Mackey, Effects of subcooling and two-phase inlet on flow boiling heat transfer and critical heat flux in a horizontal channel with one-sided and double-sided heating, Int. J. Heat Mass Transf. 91 (2015) 1187–1205, doi: 10.1016/j.ijheatmasstransfer.2015.08.059.

[55] C.R. Kharangate, L.E. O'Neill, I. Mudawar, Effects of two-phase inlet quality, mass velocity, flow orientation, and heating perimeter on flow boiling in a rectangular channel: Part 2 – CHF experimental results and model, Int. J. Heat Mass Transf. 103 (2016) 1280–1296, doi: 10.1016/j.ijheatmasstransfer.2016.05.059.

[56] C.R. Kharangate, L.E. O'Neill, I. Mudawar, L.E. O'Neill, I. Mudawar, L.E. O'Neill, I. Mudawar, Effects of two-phase inlet quality, mass velocity, flow orientation, and heating perimeter on flow boiling in a rectangular channel: Part 1 – Two-phase flow and heat transfer results, Int. J. Heat Mass Transf. 103 (2016) 1261–1279, doi: 10.1016/j.ijheatmasstransfer.2016.05.060.

[57] V.S. Devahdhanush, I. Mudawar, H.K. Nahra, R. Balasubramaniam, M.M. Hasan, J.R. Mackey, Experimental heat transfer results and flow visualization of vertical upflow boiling in Earth gravity with subcooled inlet conditions – In preparation for experiments onboard the International Space Station, Int. J. Heat Mass Transf. 188 (2022) 122603, doi: 10.1016/j.ijheatmasstransfer.2022.122603.

[58] S.J. Darges, V.S. Devahdhanush, I. Mudawar, H.K. Nahra, R. Balasubramaniam, M.M. Hasan, J.R. Mackey, Experimental results and interfacial lift-off model predictions of critical heat flux for flow boiling with subcooled inlet conditions – In preparation for experiments onboard the International Space Station, Int. J. Heat Mass Transf. 183 (2022) 122241, doi: 10.1016/j.ijheatmasstransfer.2021.122241.

[59] V.S. Devahdhanush, S.J. Darges, I. Mudawar, H.K. Nahra, R. Balasubramaniam, M.M. Hasan, J.R. Mackey, Flow visualization, heat transfer, and critical heat flux of flow boiling in Earth gravity with saturated liquid-vapor mixture inlet conditions – In preparation for experiments onboard the International Space Station, Int. J. Heat Mass Transf. 192 (2022) 122890, doi: 10.1016/j.ijheatmasstransfer.2022.122890.

[60] V.S. Devahdhanush, I. Mudawar, Subcooled flow boiling heat transfer in a partially-heated rectangular channel at different orientations in Earth gravity, Int. J. Heat Mass Transf. 195 (2022) 123200, doi: 10.1016/j.ijheatmasstransfer.2022.123200.

[61] S.J. Darges, V.S. Devahdhanush, I. Mudawar, Assessment and development of flow boiling critical heat flux correlations for partially heated rectangular channels in different gravitational environments, Int. J. Heat Mass Transf. 196 (2022) 123291, doi: 10.1016/j.ijheatmasstransfer.2022.123291.

[62] W.A. Arnold, T.G. Hartman, J. McQuillen, Chemical characterization and thermal stressing studies of perfluorohexane fluids for space-based applications, J. Spacecr. Rockets 44 (1) (2007) 94–102, doi: 10.2514/1.22537.

[63] S. Lee, V.S. Devahdhanush, I. Mudawar, Experimental and analytical investigation of flow loop induced instabilities in micro-channel heat sinks, Int. J. Heat Mass Transf. 140 (2019)

303–330, doi: 10.1016/j.ijheatmasstransfer.2019.05.077.

[64] J. Lee, V.S. Devahdhanush, S.J. Darges, I. Mudawar, Effects of flow loop compressible volume position on system instabilities during flow boiling in micro-channel heat sinks, Int. J. Heat Mass Transf. 198 (2022) 123394, doi: 10.1016/j.ijheatmasstransfer.2022.123394.

[65] P.A. Kew, K. Cornwell, Correlations for the prediction of boiling heat transfer in small-diameter channels, Appl. Therm. Eng. 17 (8–10) (1997) 705–715, doi: 10.1016/S1359-4311(96)00071-3.

[66] N. Brauner, A. Ullmann, The Prediction of Flow Boiling Maps in Minichannels, 4th Japanese-European Two-Phase Flow Group Meeting, Kyoto, Japan, 2006.

[67] J.M. Li, B.X. Wang, Size effect on two-phase regime for condensation in micro/mini tubes, Heat Transf. - Asian Res. 32 (1) (2003) 65–71, doi: 10.1002/htj.10076.

[68] C.L. Ong, J.R. Thome, Macro-to-microchannel transition in two-phase flow: Part 1 – Two-phase flow patterns and film thickness measurements, Exp. Therm. Fluid Sci. 35 (1) (2011) 37–47, doi: 10.1016/j.expthermflusci.2010.08.004.

[69] H. Zhang, I. Mudawar, M.M. Hasan, Assessment of dimensionless CHF correlations for subcooled flow boiling in microgravity and Earth gravity, Int. J. Heat Mass Transf. 50 (23–24) (2007) 4568–4580, doi: 10.1016/j.ijheatmasstransfer.2007.03.030.

[70] H. Zhang, I. Mudawar, M.M. Hasan, CHF model for subcooled flow boiling in Earth gravity and microgravity, Int. J. Heat Mass Transf. 50 (19–20) (2007) 4039–4051, doi: 10.1016/j.ijheatmasstransfer.2007.01.029.

[71] H. Zhang, I. Mudawar, M.M. Hasan, Experimental and theoretical study of orientation effects on flow boiling CHF, Int. J. Heat Mass Transf. 45 (22) (2002) 4463–4477, doi: 10.1016/S0017-9310(02)00152-7.

[72] E.W. Lemmon, I.H. Bell, M.L. Huber, M.O. McLinden, NIST Standard Reference Database 23: Reference Fluid Thermodynamic and Transport Properties-REFPROP, Version 10, NIST, Gaithersburg, MD, USA, 2018.

[73] C. Konishi, I. Mudawar, M.M. Hasan, Investigation of localized dryout versus CHF in saturated flow boiling, Int. J. Heat Mass Transf. 67 (2013) 131–146, doi: 10.1016/j.ijheatmasstransfer.2013.07.082.

[74] V.S. Devahdhanush, S. Lee, I. Mudawar, Experimental investigation of subcooled flow boiling in annuli with reference to thermal management of ultra-fast electric vehicle charging cables, Int. J. Heat Mass Transf. 172 (2021) 121176, doi: 10.1016/j.ijheatmasstransfer.2021.121176.

[75] V.S. Devahdhanush, I. Mudawar, Review of critical heat flux (CHF) in jet impingement boiling, Int. J. Heat Mass Transf. 169 (2021) 120893, doi: 10.1016/j.ijheatmasstransfer.2020.120893.

Table 1 Key dimensions of test module (FBM).

Upstream development length, L_d	327.7 mm
Heated length, L_h	114.6 mm
Downstream exit length, L_e	60.7 mm

Thermocouple locations (7) from heated section start, z_{tc}	5.4, 22.7, 40.0, 57.3, 74.6, 91.9, 109.2 mm
Channel height (unheated), H	5.0 mm
Channel width (heated), W	2.5 mm

Table 2 Maximum measurement uncertainties.

Measured Parameters	**Maximum Uncertainty**
Temperature (thermocouples)	±0.5°C
Temperature (RTDs)	±0.5°C
Pressure	±0.7 kPa
FBM heater power	±0.3% reading
BHM (preheater) power	±0.6% reading
Mass flow rate	±0.6% reading

Table 3 Summary of key parameters of ISS steady-state database for subcooled inlet with single-sided heating.

	Single-Sided Heating
Mass velocity, G	199.90 – 3200.13 kg/m^{2}s
Mass flow rate, $\dot{m}$	2.50 – 40.00 g/s
Inlet pressure, p_{in}	113.30 – 164.29 kPa
Inlet temperature, T_{in}	23.11 – 70.96˚C
Inlet subcooling, $\Delta T_{sub,in}$	+0.10 – 45.76˚C
Inlet quality, $x_{e,in}$	-0.610 – -0.001
Wall heat flux, q''_w	2.03 – 56.46 W/cm^2
Outlet pressure, p_{out}	114.13 – 159.86 kPa
Outlet temperature, T_{out}	23.16 – 70.61˚C
Outlet subcooling, $\Delta T_{sub,out}$	0.30 – 44.87˚C
Outlet quality, $x_{e,out}$	-0.593 – 0.149

Table 4 Summary of ISS experiments for subcooled inlet with single-sided heating.

Experiment Reference Number (Expt.#)	G **[kg/m^{2}s]**	p_{in} **[kPa]**	$\Delta T_{sub,in}$ **[˚C]**
4112	199.97	131.20	6.43
2113	399.92	132.53	4.39
2114	799.94	133.98	3.52

2115	1599.94	131.39	3.84
2116	2399.99	130.43	4.24
2117	2813.57	131.36	4.27
3118	200.03	150.73	2.93
2119	399.95	151.07	3.69
4120	799.70	152.17	2.97
2121	1599.93	152.88	4.21
2122	2400.00	151.81	4.54
2123	2645.57	152.29	4.30
4124	200.17	131.03	14.66
2125	400.77	130.93	15.05
2126	800.05	130.10	14.73
3127	1599.92	129.21	14.60
2128	2399.99	128.12	13.64
2129	3199.97	124.21	13.08
3130	200.34	147.80	13.97
2131	399.95	148.41	13.16
3132	800.15	149.60	15.20
2133	1599.93	151.33	15.12
2134	2399.82	148.79	14.75
3135	3199.97	147.38	14.24
2136	201.47	131.35	29.19
2137	401.93	134.10	30.74
3138	801.67	130.20	29.11
2139	1599.90	129.23	29.13
2140	2399.98	125.21	27.09
2141	3199.97	124.85	27.90
2142	201.45	148.94	29.06
2143	402.07	146.42	29.73
2144	801.60	151.32	29.76
2145	1599.92	150.45	29.72
3146	2399.97	147.83	28.44
2147	3199.84	146.89	26.99
228	202.66	147.65	42.45
231	199.98	146.01	23.92
232	200.93	147.34	19.76
2233	199.98	147.72	8.69
234	199.95	147.91	7.44
3235	199.98	147.38	7.25
236	199.97	155.31	0.31
237	800.94	148.61	45.64

238	803.13	149.24	39.28
2239	801.75	147.40	34.62
240	800.49	149.30	24.41
241	800.10	149.27	19.84
242	800.01	149.93	9.58
243	799.99	149.74	7.72
244	799.96	150.35	6.06
245	799.96	153.98	2.11
246	2400.03	147.28	44.95
247	2399.99	148.39	39.46
248	2399.99	148.54	34.28
249	2399.98	149.66	25.05
250	2400.00	148.99	19.74
251	2399.98	150.48	10.24
252	2399.99	151.05	7.95
2253	2399.99	151.64	6.08
254	2400.00	157.65	2.48
262	319.93	150.13	2.20
263	480.01	151.28	2.17
264	639.93	151.30	2.53
265	1280.11	154.62	2.86
2266	1599.93	156.47	1.95
267	2080.01	155.70	3.02
2268	2695.96	158.11	3.34

Table 5 Summary of key observations from the present ISS microgravity experiments for subcooled inlet with single-sided heating.

(a) Typical effects of mass velocity on various aspects.

Aspect	**Low Mass Velocity**	**High Mass Velocity**
Interfacial flow physics	The bubble boundary and vapor layers are thicker. Vapor structures are larger. Flow regime transitions occur further upstream and at lower heat fluxes. At CHF with high subcooling, a continuous wavy vapor layer completely insulates the wall with no wetting fronts. At CHF with low subcooling, a continuous vapor layer of longer wavelength almost	The bubble boundary and vapor layers are thinner. Vapor structures are smaller. Flow regime transitions occur further downstream and at higher heat fluxes. At CHF with high subcooling, a distinct single-phase region exists upstream. At CHF for low subcooling, a vapor layer of smaller wavelength exists along the heated wall with reduced wetting

	fills the entire channel, completely insulating the heated wall.	fronts and highly turbulent interfacial structures downstream.
Local wall temperature	For similar heat fluxes, T_w is higher all along the channel. But for similar heat flux percentages, no notable differences in $T_{w,z}$ profiles. Closer to CHF, T_w is maximum at a short distance upstream of the exit.	For similar heat fluxes, T_w is lower all along the channel. But for similar heat flux percentages, no notable differences in $T_{w,z}$ profiles. Closer to CHF, T_w is maximum at around the middle of the channel.
Local heat transfer coefficient	Lower h. At high heat flux percentages, the entire streamwise h profile is severely degraded.	Higher h. At high heat flux percentages, h profile degradation is limited to the channel middle and exit.
Average heat transfer coefficient	$\bar{h}$ peaks at smaller heat flux. For highly subcooled inlet, the peak $\bar{h}$ is lower.	$\bar{h}$ peaks at larger heat flux. For highly subcooled inlet, the peak $\bar{h}$ is higher.
ONBD and CHF	Manifests at smaller heat fluxes.	Manifests at larger heat fluxes.

(b) Typical effects of inlet subcooling on various aspects.

Aspect	**Highly Subcooled Inlet (High Inlet Subcooling)**	**Near-Saturated Inlet (Low Inlet Subcooling)**
Interfacial flow physics	The bubble boundary and vapor layers are thinner. Flow regime transitions occur further downstream and at higher heat fluxes. At lower heat fluxes, bubbles are tiny and barely visible. At high heat fluxes close to CHF, the vapor layer has some peaks barely touching the opposite wall. At CHF, wetting fronts are still present.	The bubble boundary and vapor layers are thicker. Flow regime transitions occur further upstream and at lower heat fluxes. At lower heat fluxes, bubbles are larger and coalesce. At high heat fluxes closer to CHF, the vapor layer almost completely occupies the channel's cross section. At CHF, wetting fronts are extinguished.
Local wall temperature	For similar heat fluxes, T_w is lower all along the channel. For similar heat flux percentages, T_w is lower only at the upstream end.	For similar heat fluxes, T_w is higher all along the channel. For similar heat flux percentages, T_w is higher only at the upstream end.
Local heat transfer coefficient	h is lower. At high heat flux percentages, the upstream part of streamwise h profile is not degraded.	h is higher. At high heat flux percentages, the entire streamwise h profile is severely degraded.
Average heat transfer coefficient	As heat flux is increased, $\bar{h}$ initially increases almost linearly over a broader heat flux before reaching a maximum. $\bar{h}$ peaks at larger heat flux. Peak $\bar{h}$ is lower.	As heat flux is increased, $\bar{h}$ initially increases in a less linear manner over a narrower heat flux before reaching a maximum. $\bar{h}$ peaks at smaller heat flux. Peak $\bar{h}$ is higher.

ONBD and CHF	Manifests at larger heat fluxes. Difference in heat flux between ONBD and CHF is smaller.	Manifests at smaller heat fluxes. Difference in heat flux between ONBD and CHF is larger.

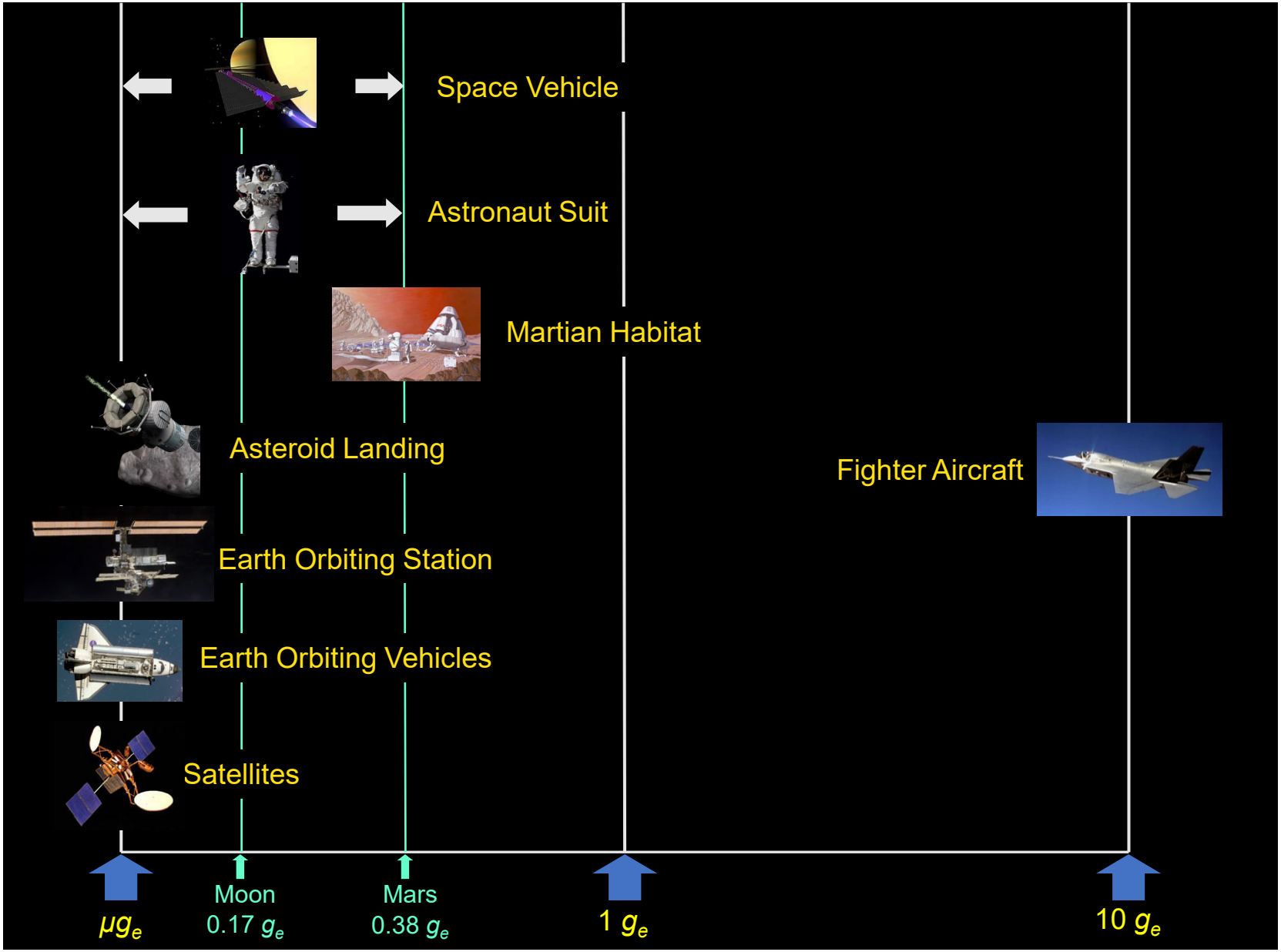

Fig. 1 Range of gravities important to study of two-phase flow and heat transfer in space and aircraft applications.

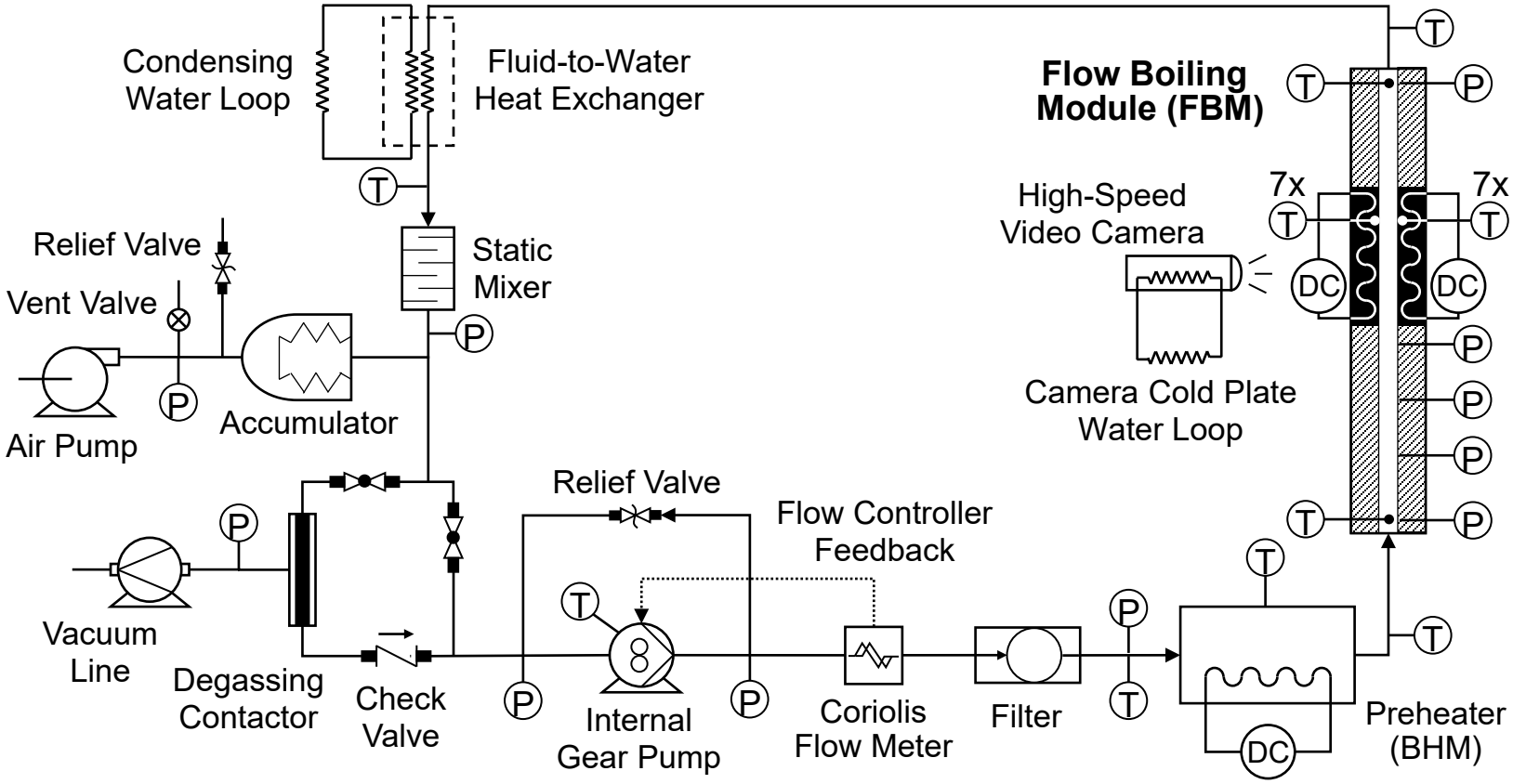

Fig. 2 Schematic diagram of two-phase flow loop for flow boiling experiments.

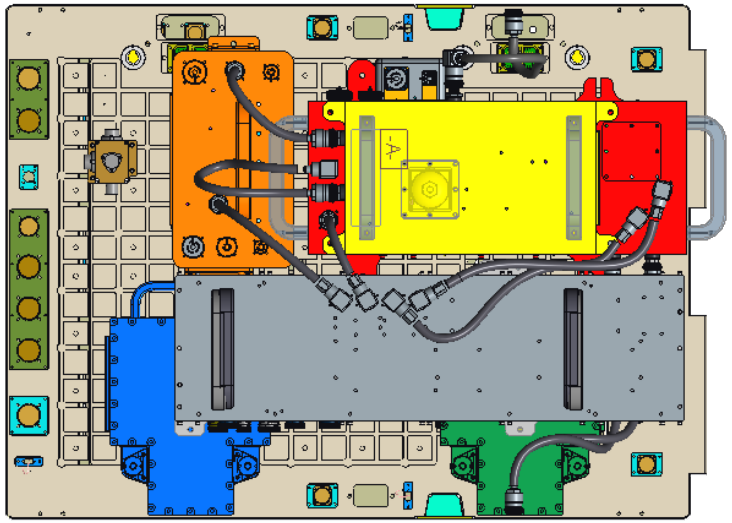

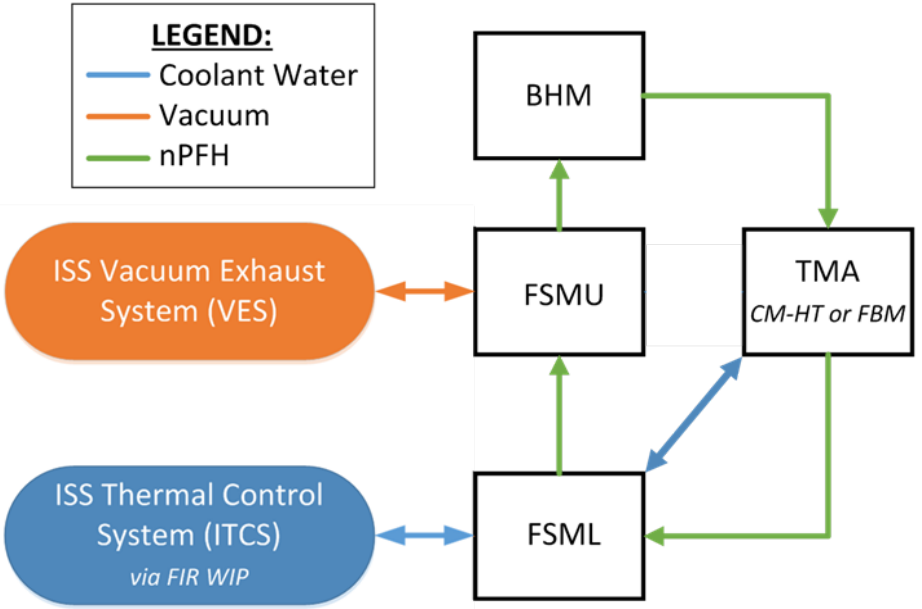

FBCE Modules:

BHM – Bulk Heater Module

FSMU – Fluids System Module - Upper

FSML – Fluids System Module - Lower

RDAQM 1 – Remote Data Acquisition Module 1

RDAQM 2 – Remote Data Acquisition Module 2

TMA – Test Module Assembly (1 of 2 installed):

FBM – Flow Boiling Module

CM-HT – Condensation Module - Heat Transfer

ISS Fluid Integrated Rack (FIR) Provided Hardware:

- SAMS – Space Acceleration Measurement System
- CCU – Confocal Control Unit (on back of rack)
- IPSU-CL – Imaging Processing Storage Unit – Camera Link (on back of rack)

Fig. 3 Layout of main modules of the Flow Boiling and Condensation Experiment (FBCE) on the Optics Bench of the Fluid Integrated Rack (FIR), and ISS provided hardware. The Optics Bench is rotated to vertical upward orientation inside the FIR during the tests.

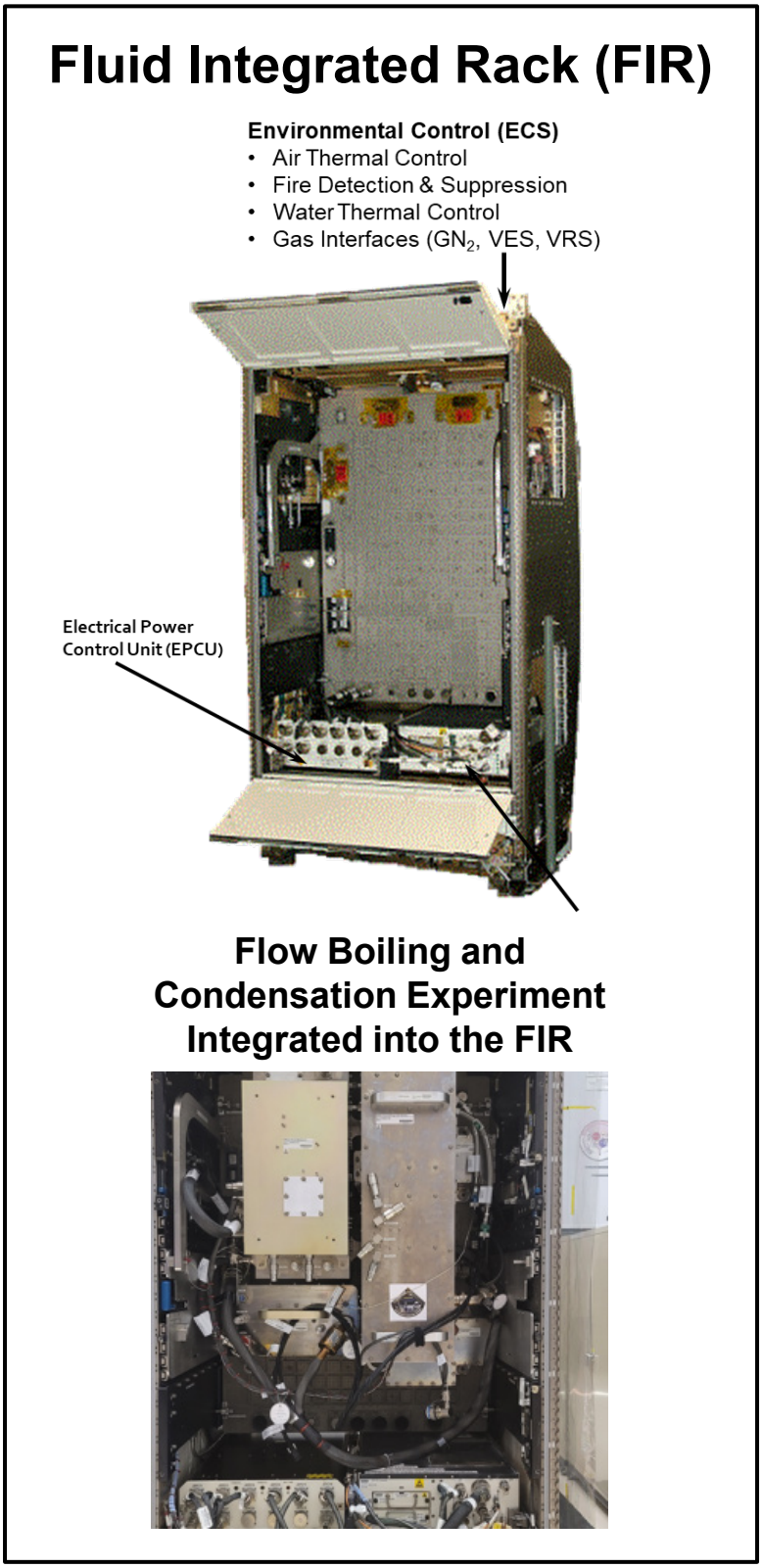

Fig. 4 Fluid Integrated Rack (FIR) and integration of FBCE into it.

Fluid System - Upper

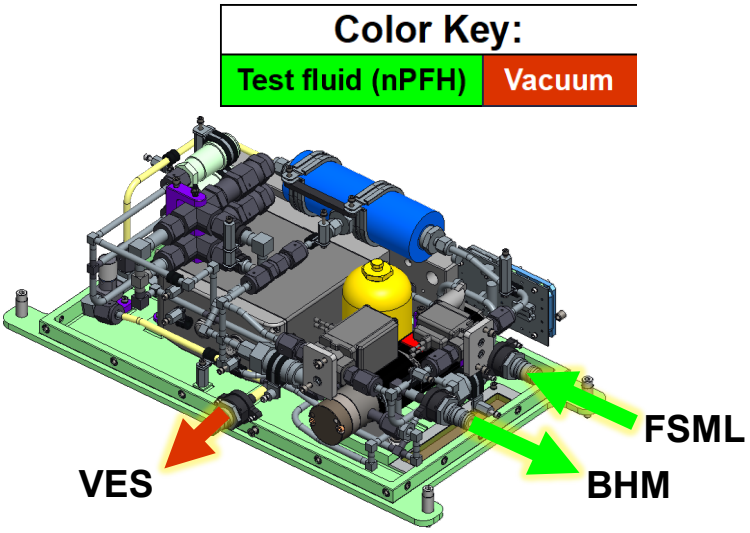

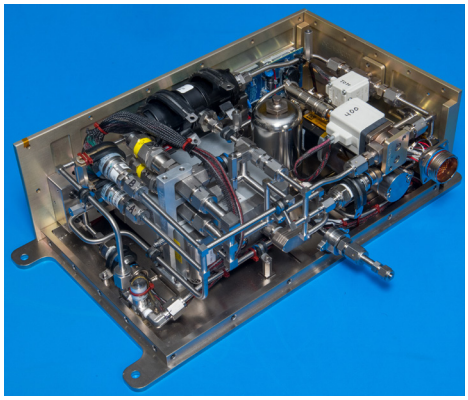

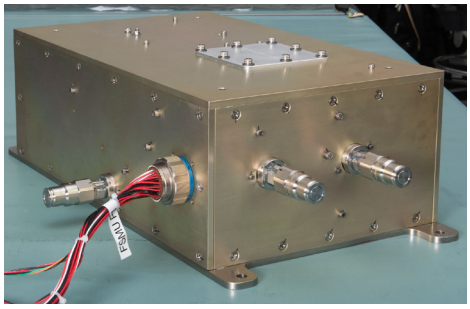

- Mass flow controller drives gear pump to provide flow throughout closed loop system
- Multiple controls prevent over-pressurization
- Degassing contactor removes dissolved gases from test fluid when membrane is exposed to vacuum

Fluid System - Lower

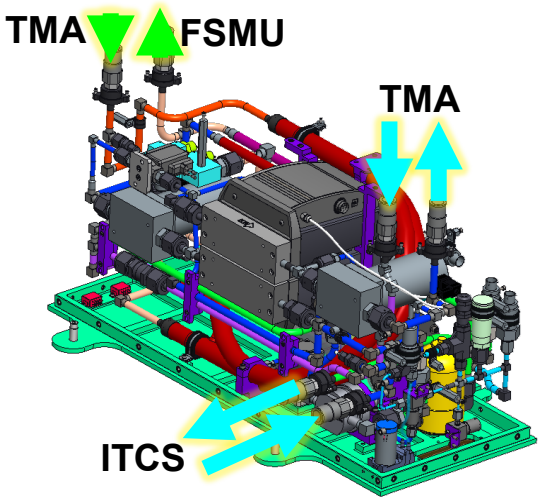

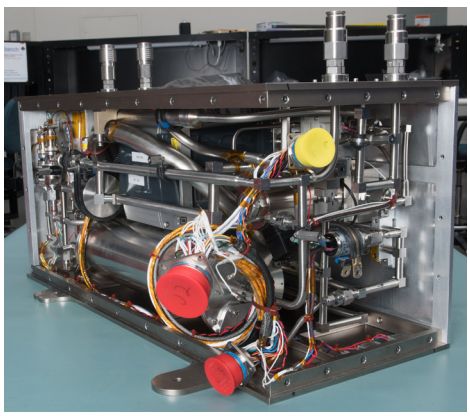

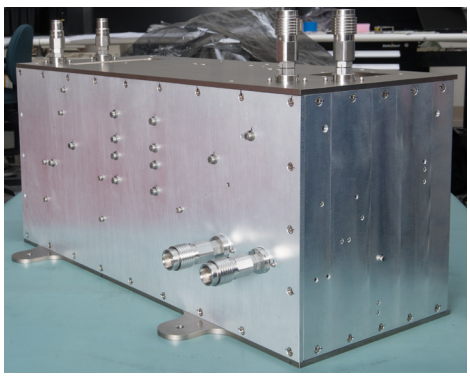

- Provides primary cooling for test fluid exiting test section, and test section itself
- System pressure set by pressurizing or venting air-side of bellows accumulator

Fig. 5 CAD renderings and photographs of Fluid System Upper and Lower modules.

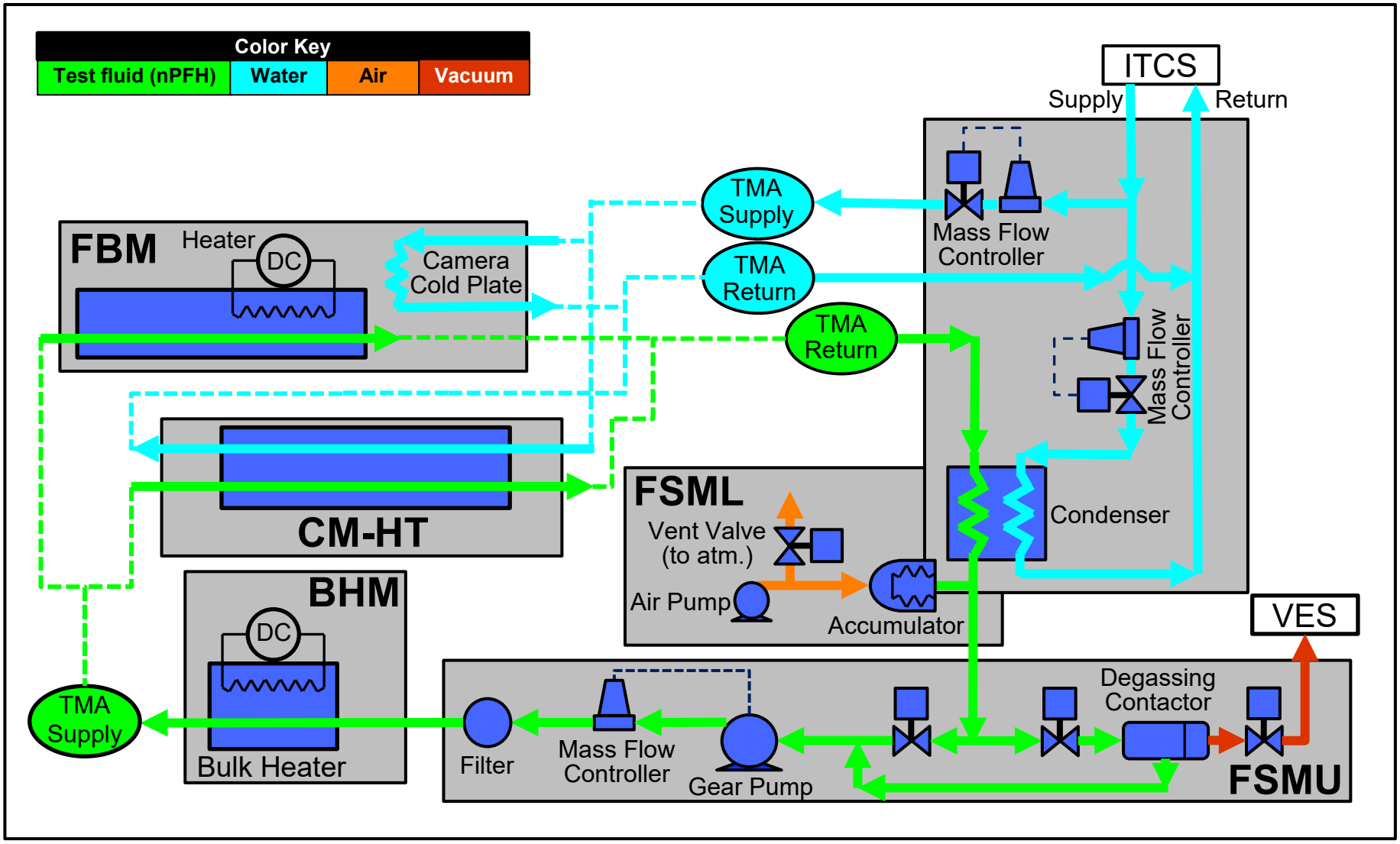

Fig. 6 Test fluid (nPFH), water, air, and vacuum connections between FBCE modules and the ISS Thermal Control System (ITCS) and ISS Vacuum Exhaust System (VES).

Bulk Heater Module (BHM)

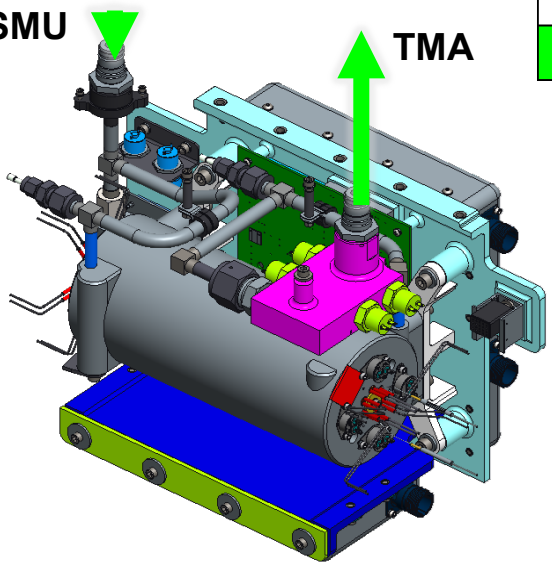

Color Key:
Test fluid (nPFH)

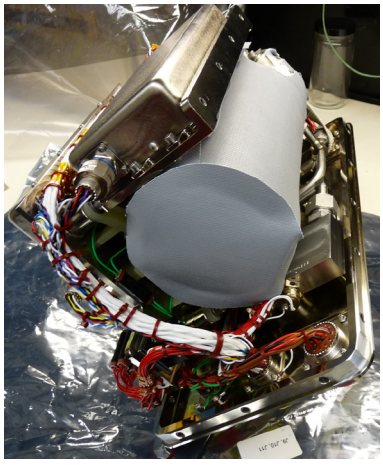

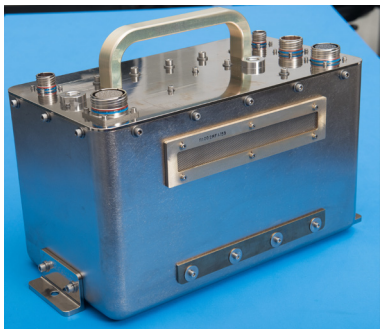

- Primary source of heating to condition test fluid to required test section inlet conditions
- Three 120V primary heaters and three 28V booster heaters can be operated at any time, with backup heaters available

Remote Data Acquisition Module 1 (RDAQM1)

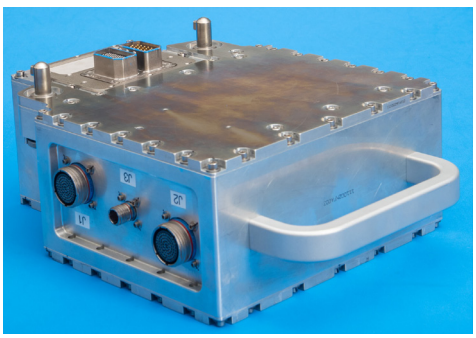

UEI Data Cubes
(Thermocouple Signal Conditioning)

Remote Data Acquisition Module 2 (RDAQM2)

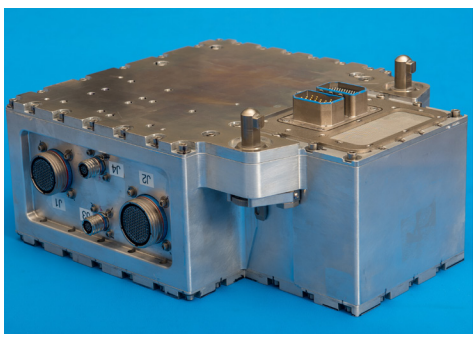

UEI Data Cube and Custom Sensor Supply Printed Circuit Board
(Signal Conditioning and Power Distribution)

Fig. 7 Bulk Heater Module and Remote Data Acquisition Modules 1 and 2.

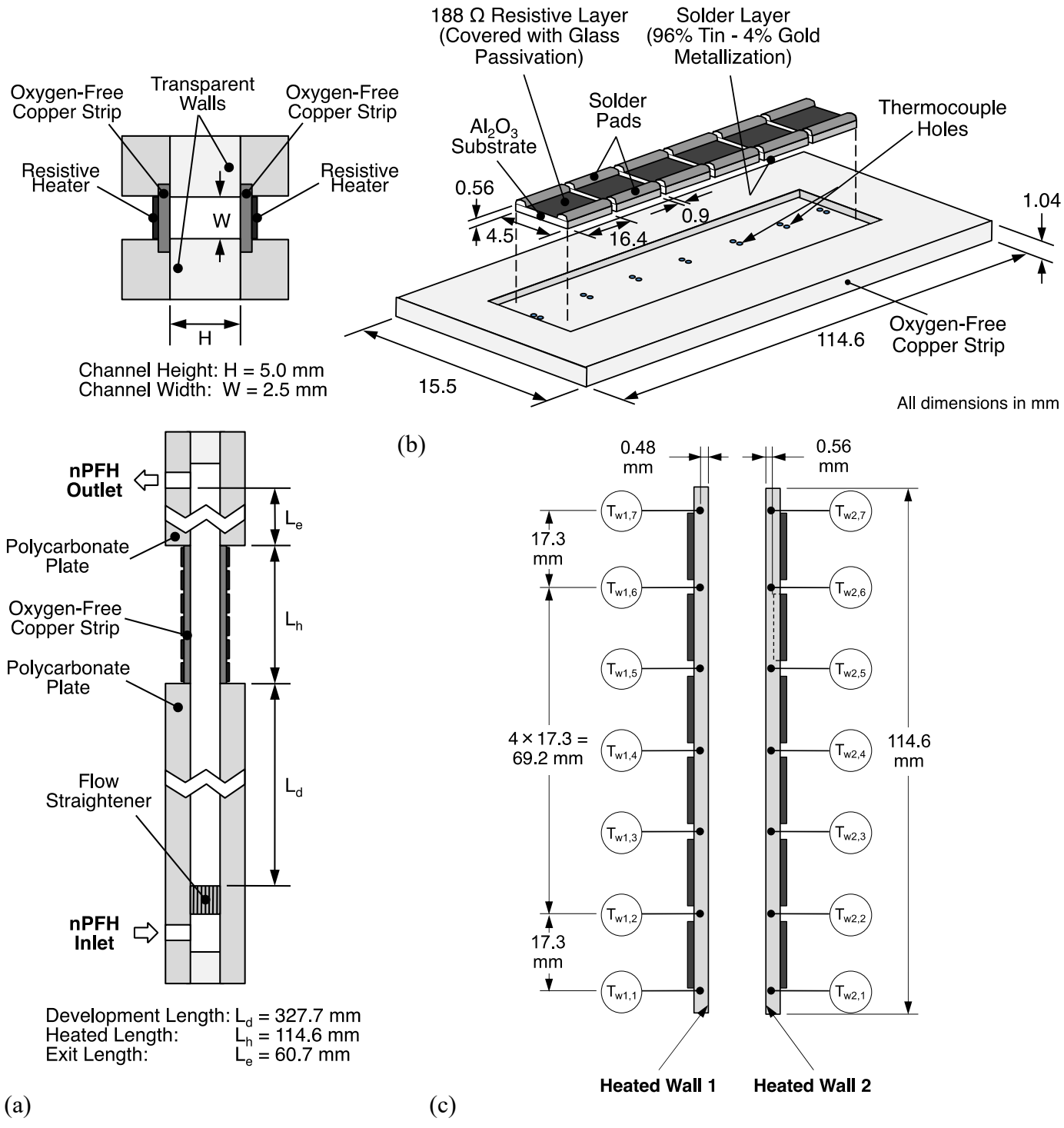

Fig. 8 Schematic representations of (a) overall construction of Flow Boiling Module (FBM), (b) construction of heating strips, and (c) designation of heated walls and local wall temperatures.

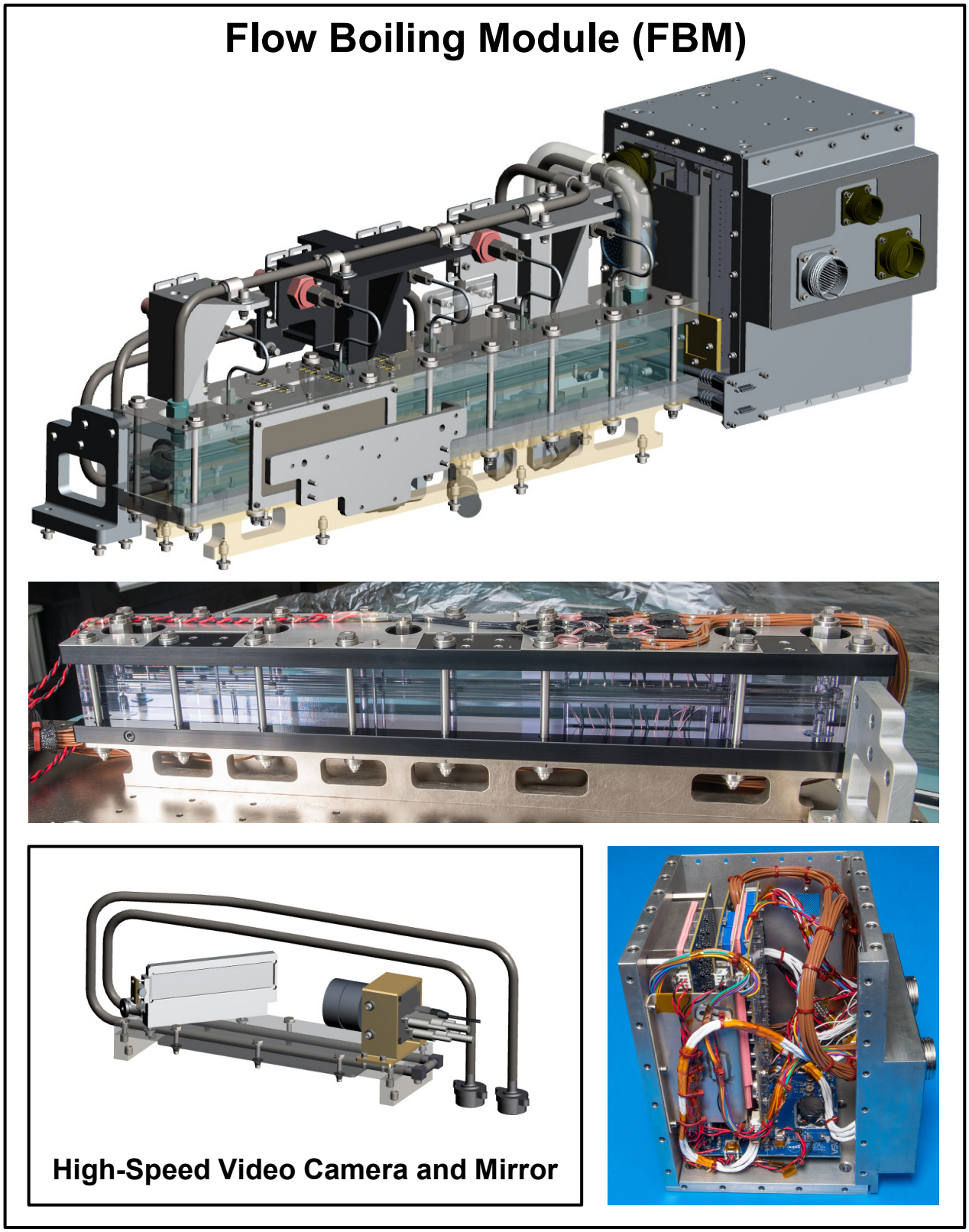

Fig. 9 CAD renderings and photographs of Flow Boiling Module.

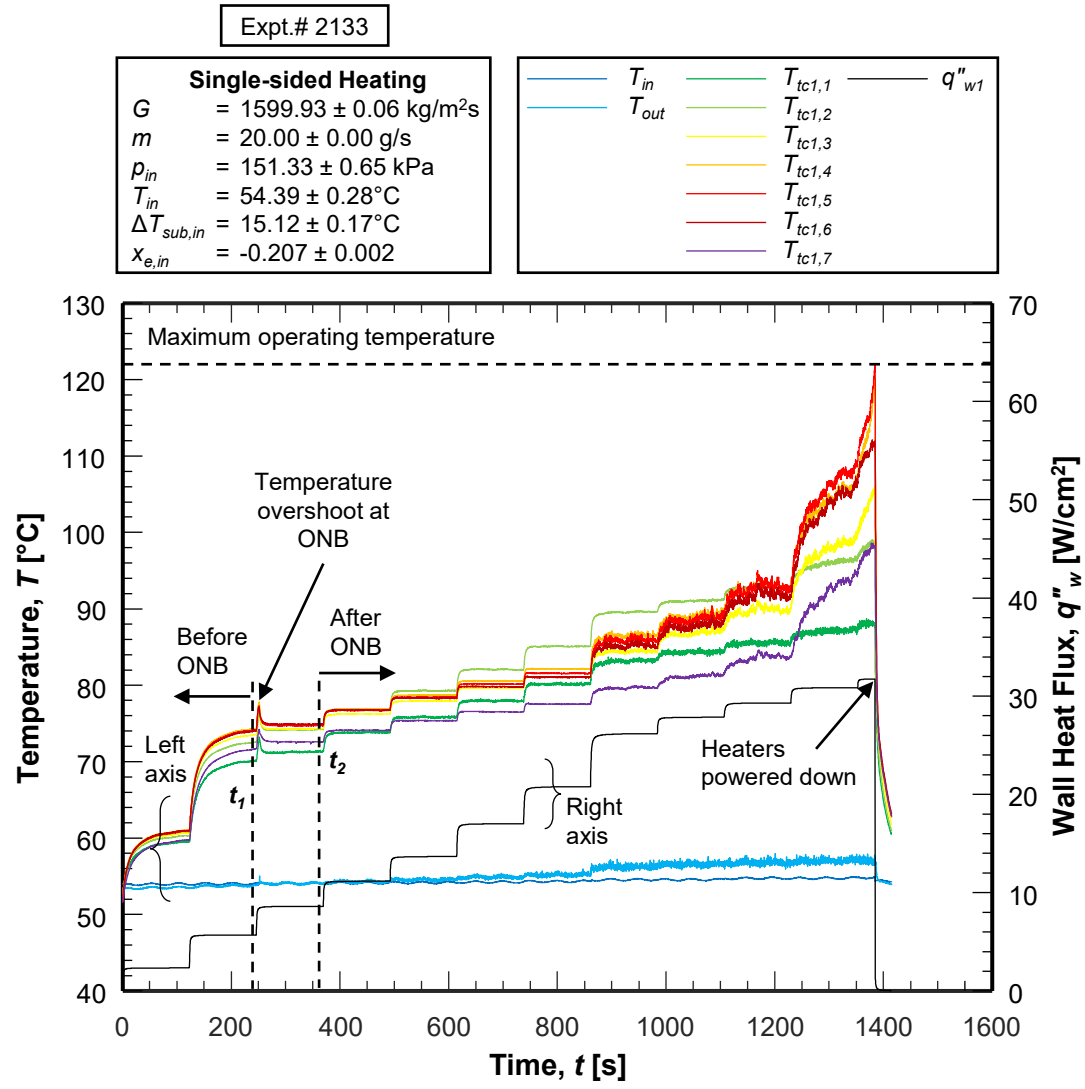

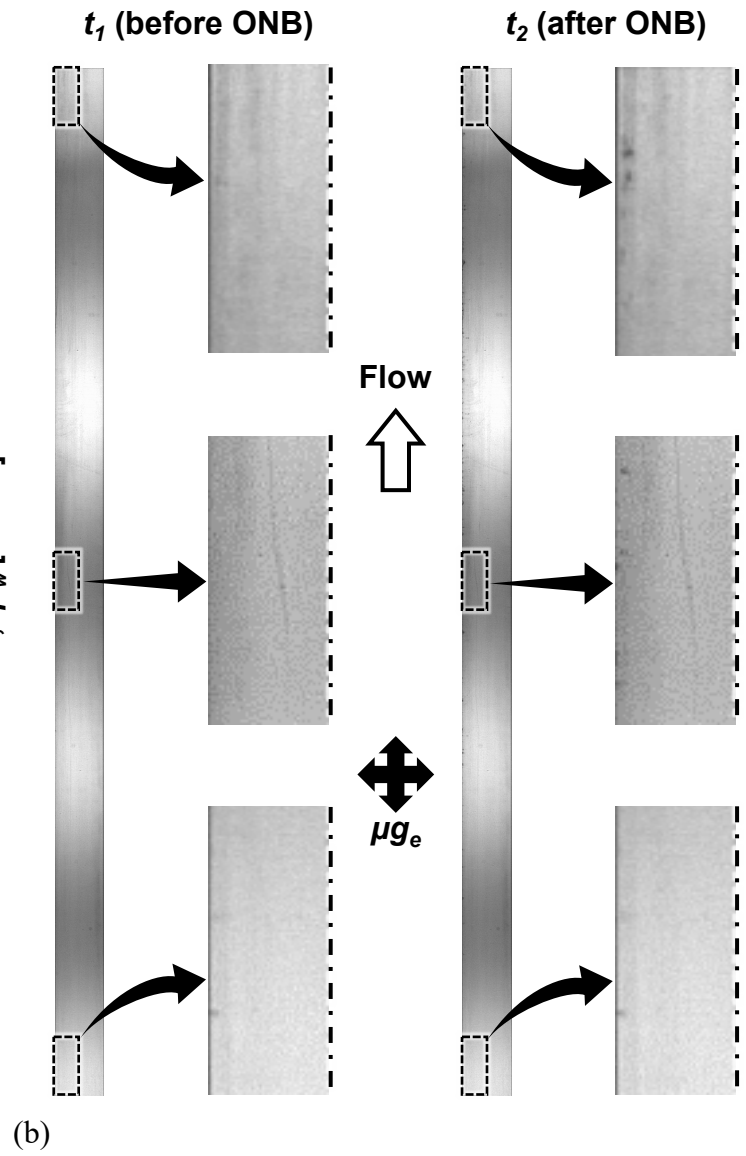

Fig. 10 (a) Temporal variations of fluid inlet, fluid outlet, and heating-strip temperatures for heat flux increments from a minimum to CHF for a representative set of operating conditions. (b) Flow visualization at time instants t_1 and t_2 (heat flux increments preceding and succeeding ONB, respectively).

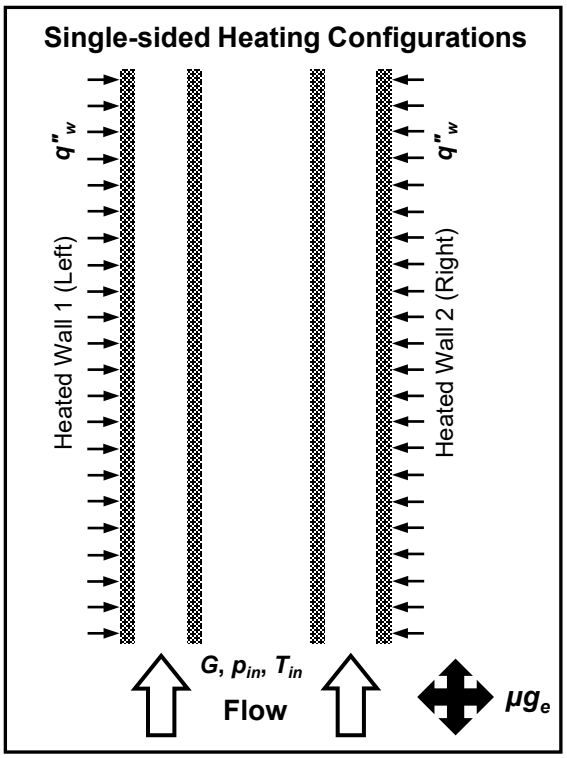

Fig. 11 Schematic representation of single-sided heating configurations.

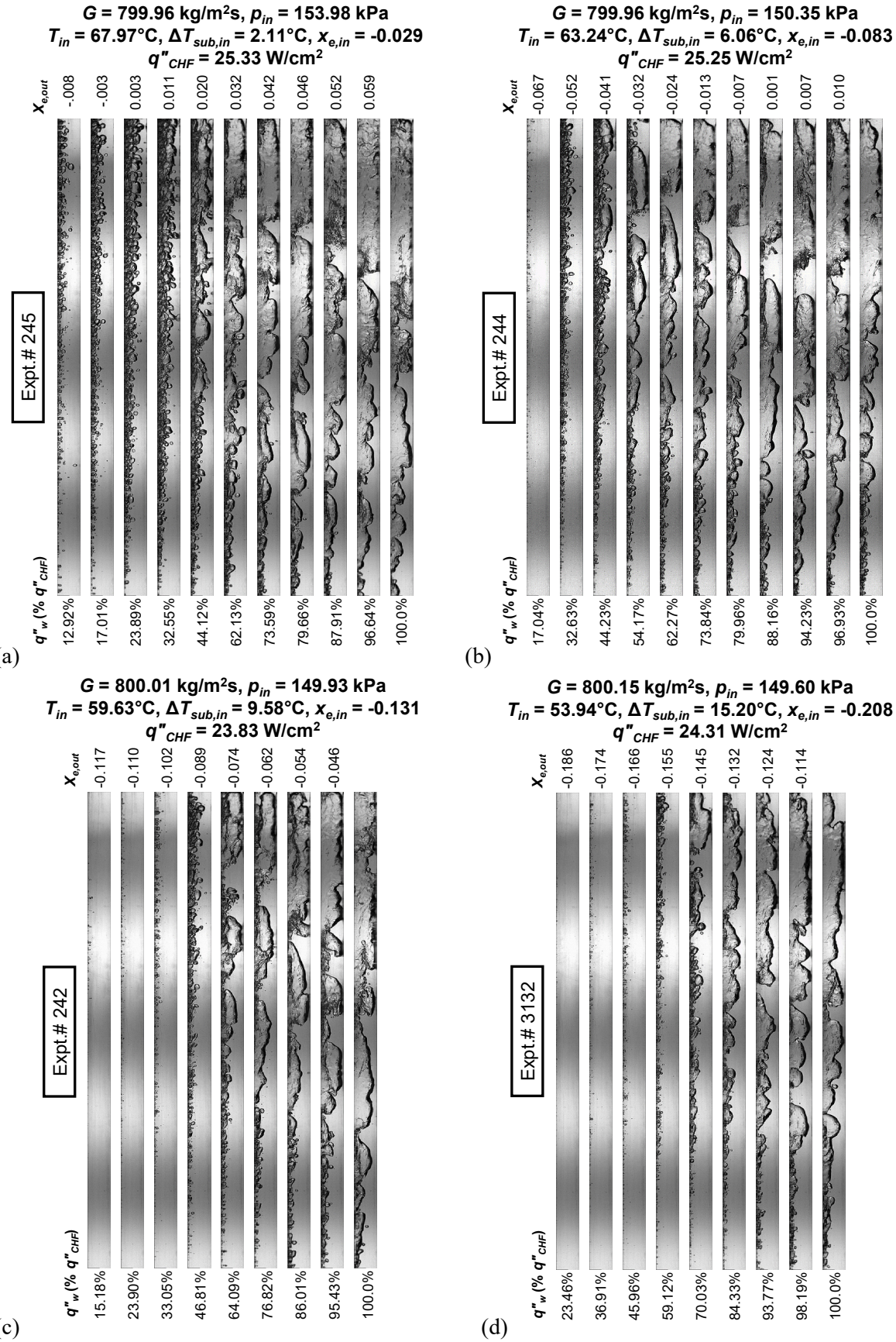

Fig. 12 Flow patterns along the boiling curve until CHF for different inlet subcoolings of $\Delta T_{sub,in}$ = (a) 2.11°C, (b) 6.06°C, (c) 9.58°C, (d) 15.20°C, (e) 19.84°C, (f) 29.76°C, and (g) 39.28°C. Mass velocity is maintained constant at $G \approx 800.70$ kg/m²s and inlet pressure at $p_{in} \approx 150.52$ kPa.

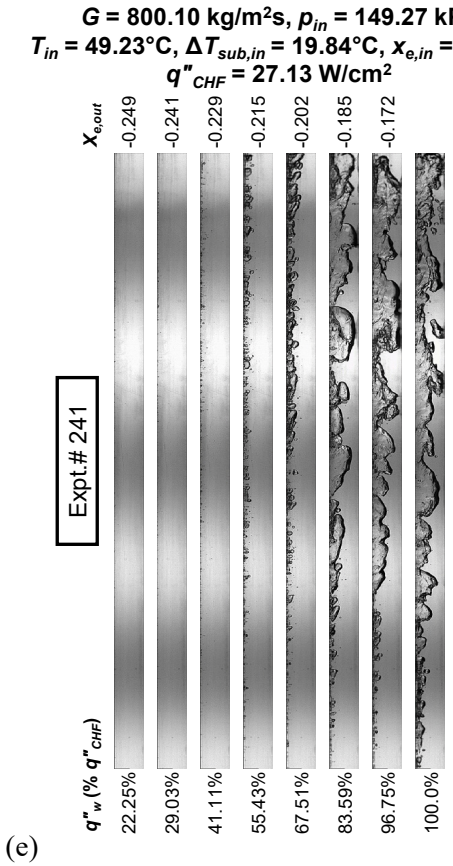

(e)

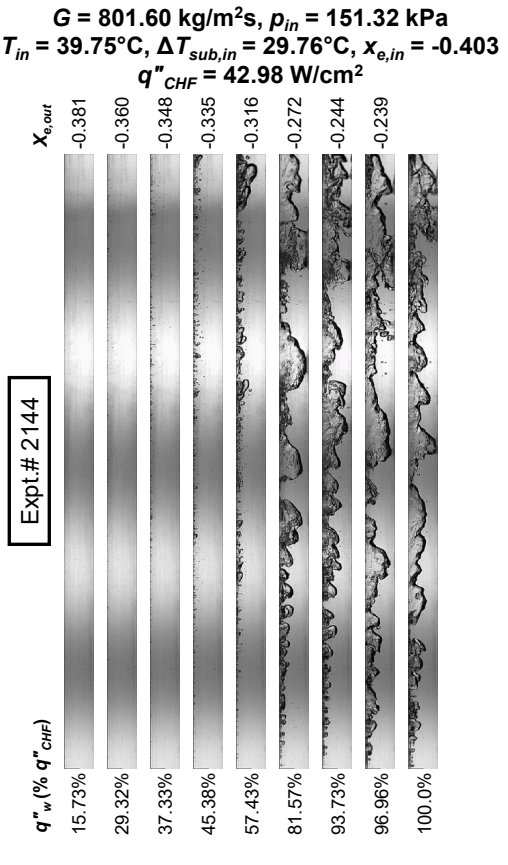

(f)

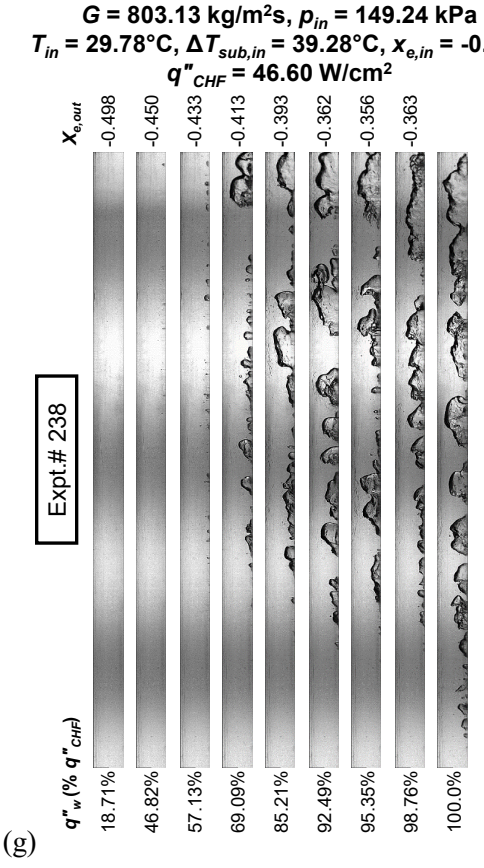

(g)

Fig. 12 (continued)

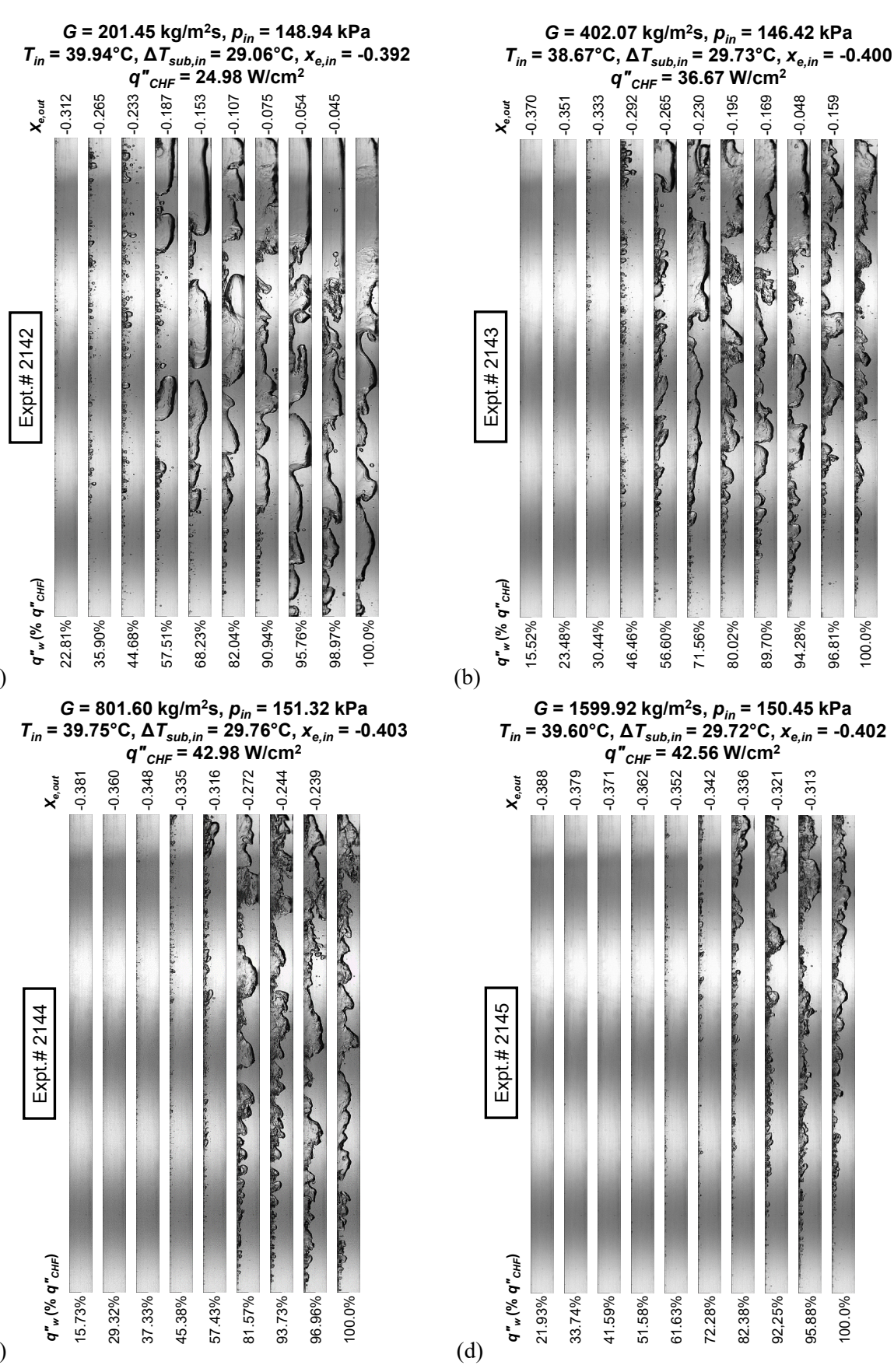

Fig. 13 Flow patterns along the boiling curve until CHF for different mass velocities of G = (a) 201.45, (b) 402.07, (c) 801.60, (d) 1599.92, and (e) 2400.00 kg/m²s. Inlet subcooling is maintained constant at $\Delta T_{sub,in} \approx 29.34$°C and inlet pressure at $p_{in} \approx$ 148.99 kPa.

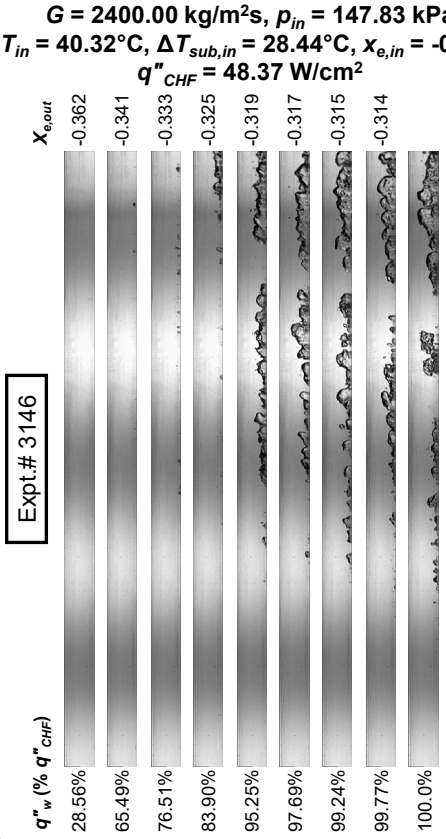

(e)

Fig. 13 (continued)

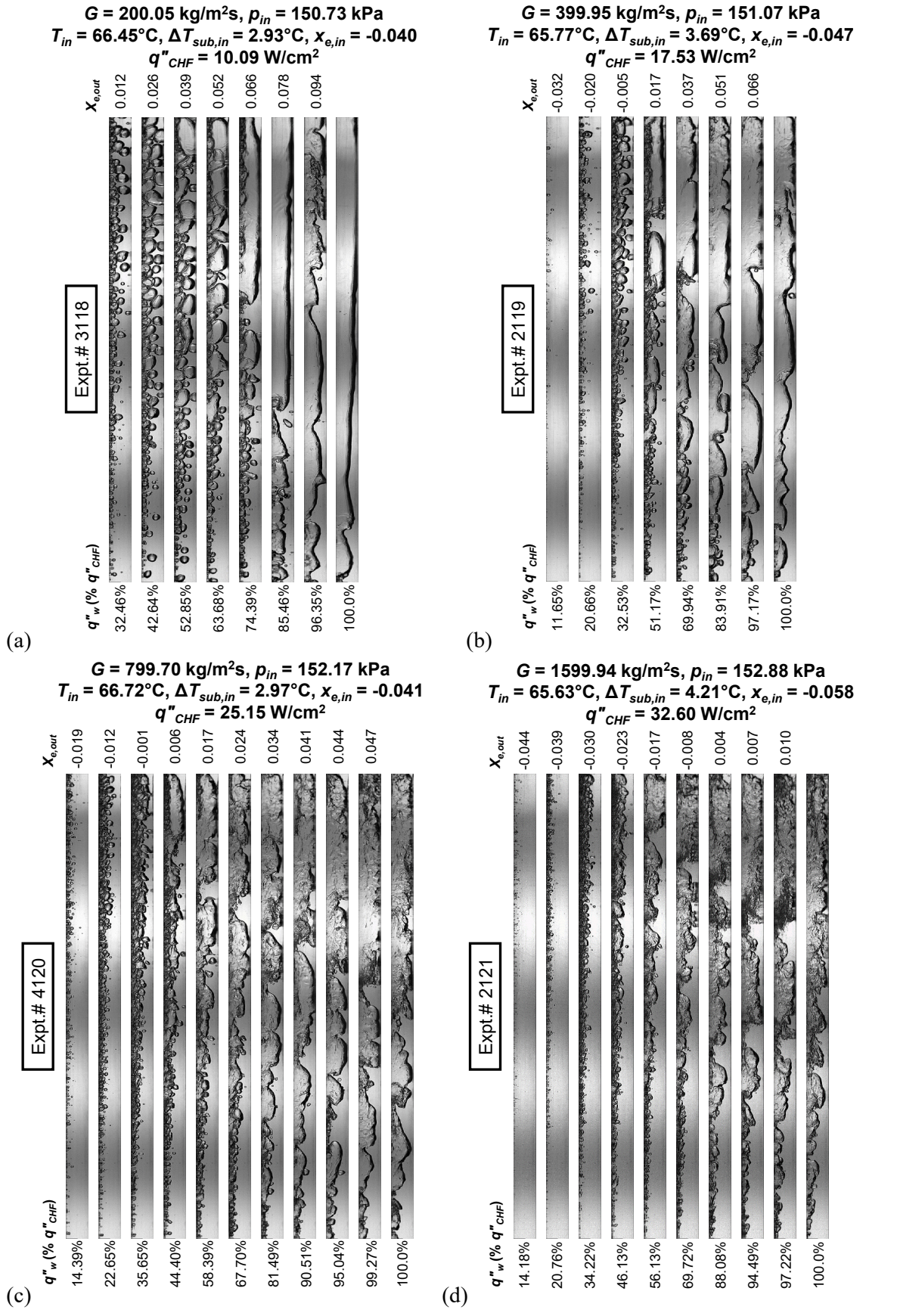

Fig. 14 Flow patterns along the boiling curve until CHF for different mass velocities of G = (a) 200.05, (b) 399.95, (c) 799.70, (d) 1599.94, and (e) 2400.00 kg/m²s. Inlet subcooling is maintained constant at $\Delta T_{sub,in} \approx 3.67$°C and inlet pressure at $p_{in} \approx$ 151.73 kPa.

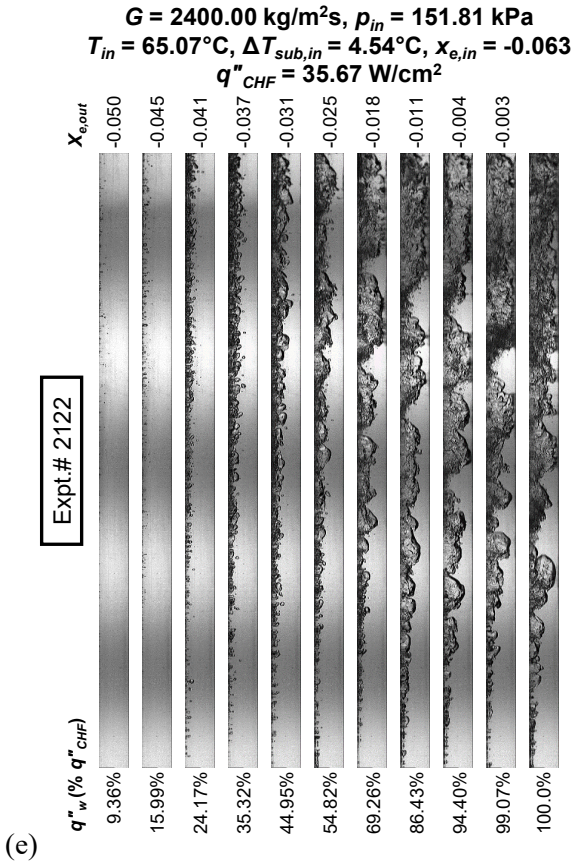

(e)

Fig. 14 (continued)

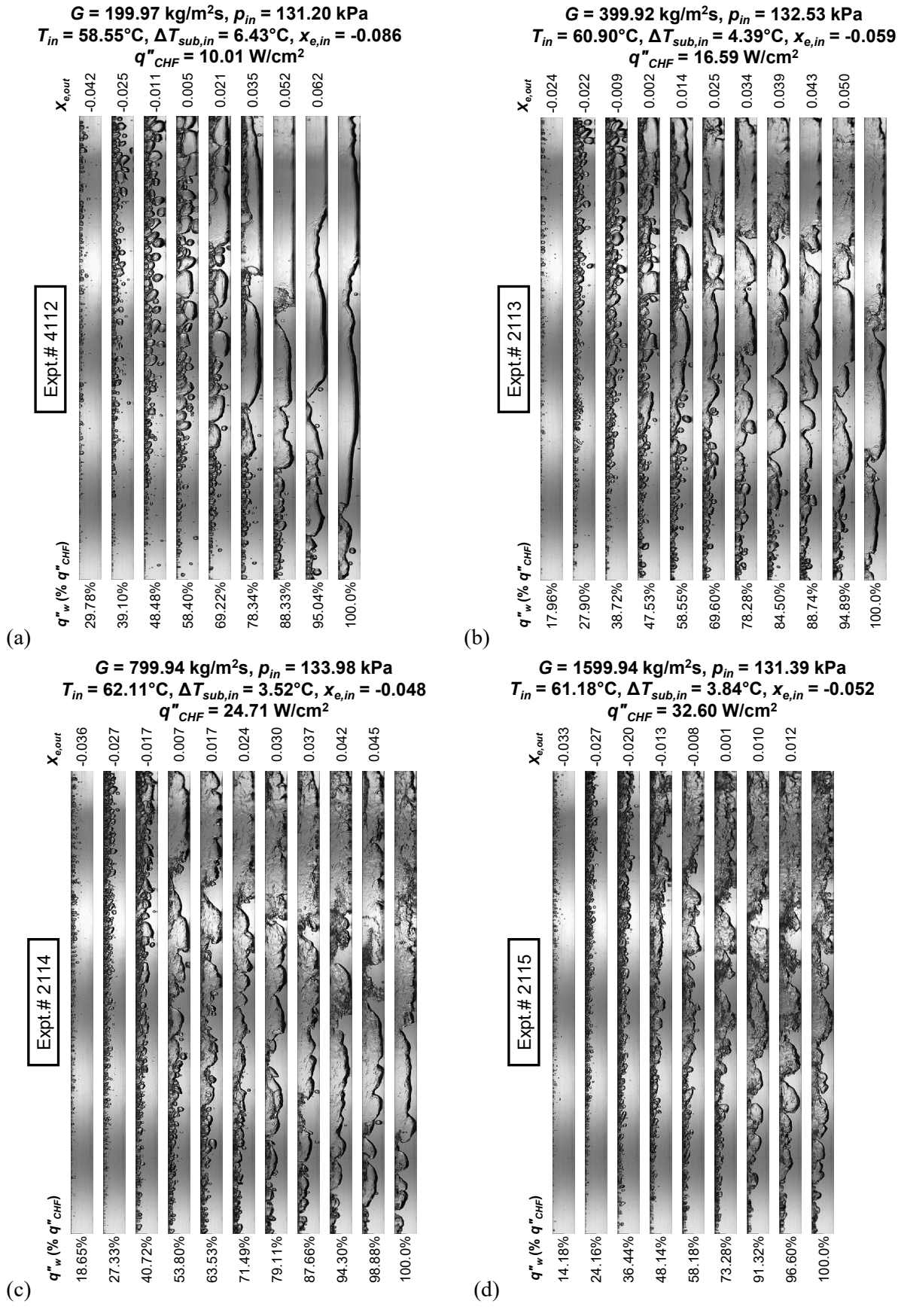

Fig. 15 Flow patterns along the boiling curve until CHF for different mass velocities of G = (a) 199.97, (b) 399.92, (c) 799.94, (d) 1599.94, and (e) 2399.99 kg/m^{2}s. Inlet subcooling is maintained constant at $\Delta T_{sub,in} \approx 4.48$°C and inlet pressure at $p_{in} \approx$ 131.91 kPa.

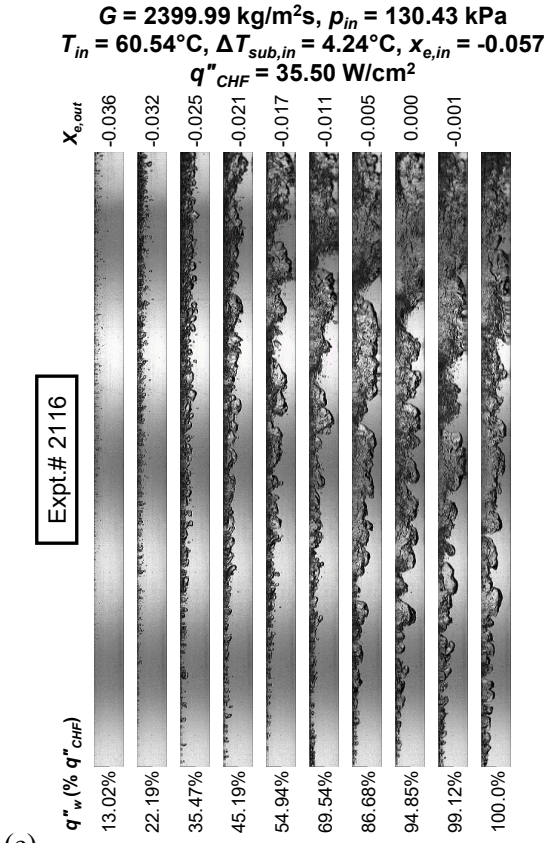

(e)

Fig. 15 (continued)

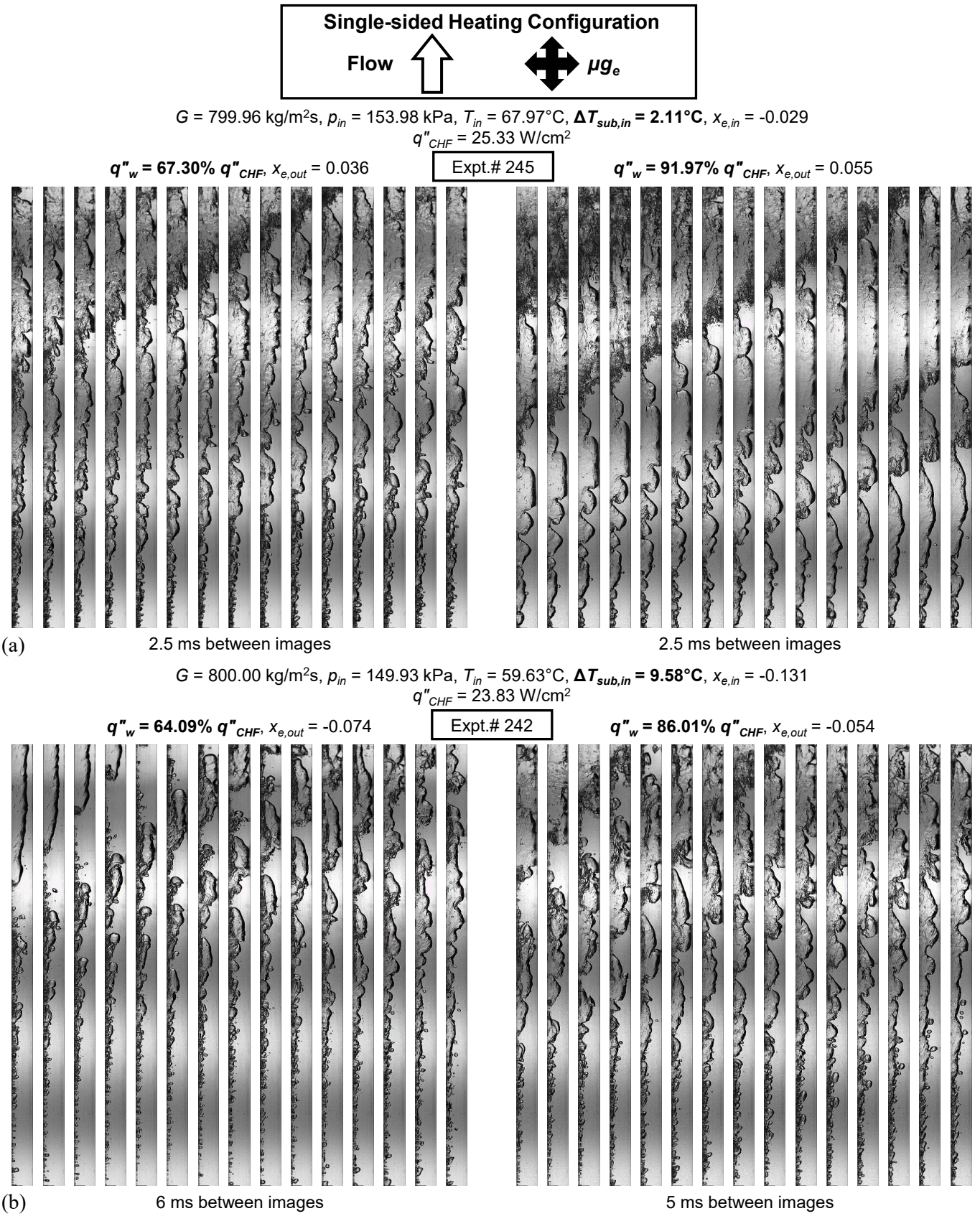

Fig. 16 Flow visualization image sequences for inlet subcoolings of $\Delta T_{sub,in}$ = (a) 2.11°C, (b) 9.58°C, and (c) 34.62°C, at fixed mass velocity and inlet pressure with single-sided heating. Time interval between successive images is mentioned below each sequence.

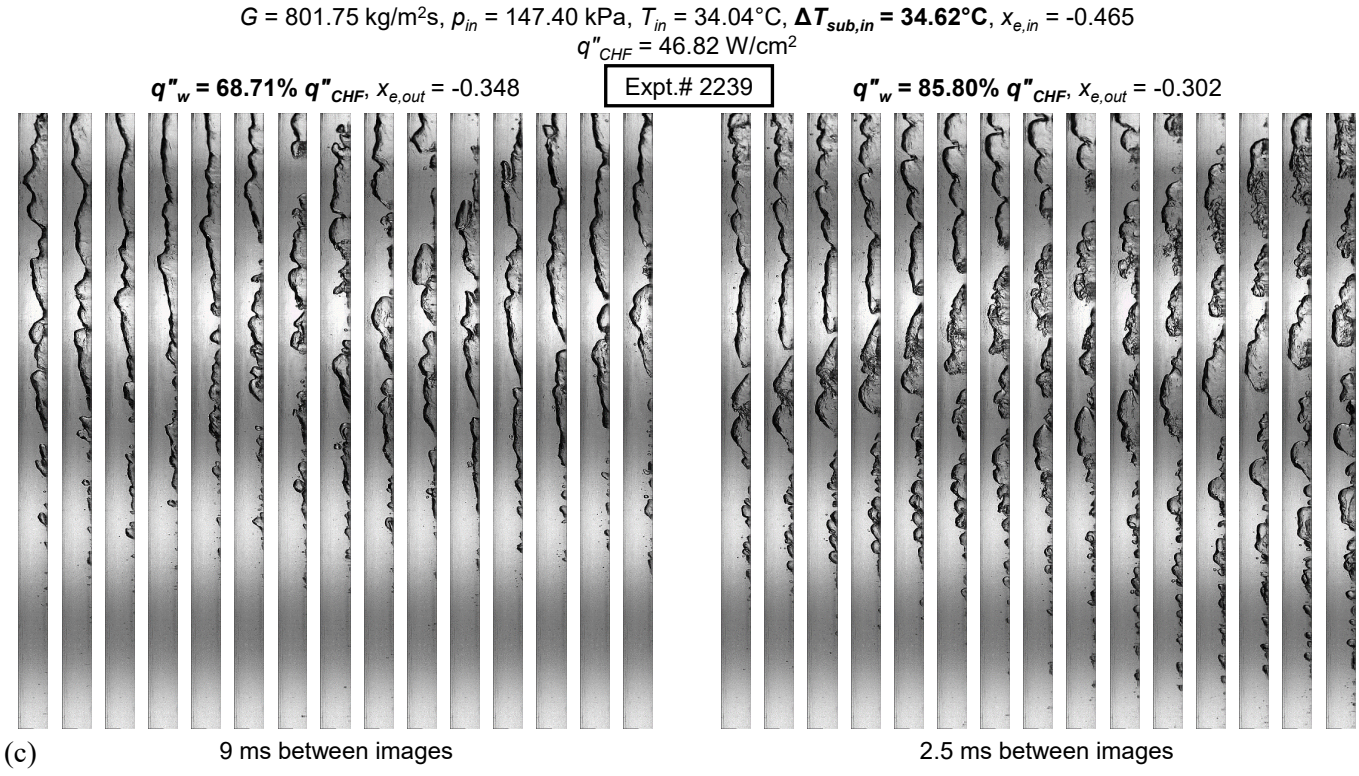

Fig. 16 (continued)

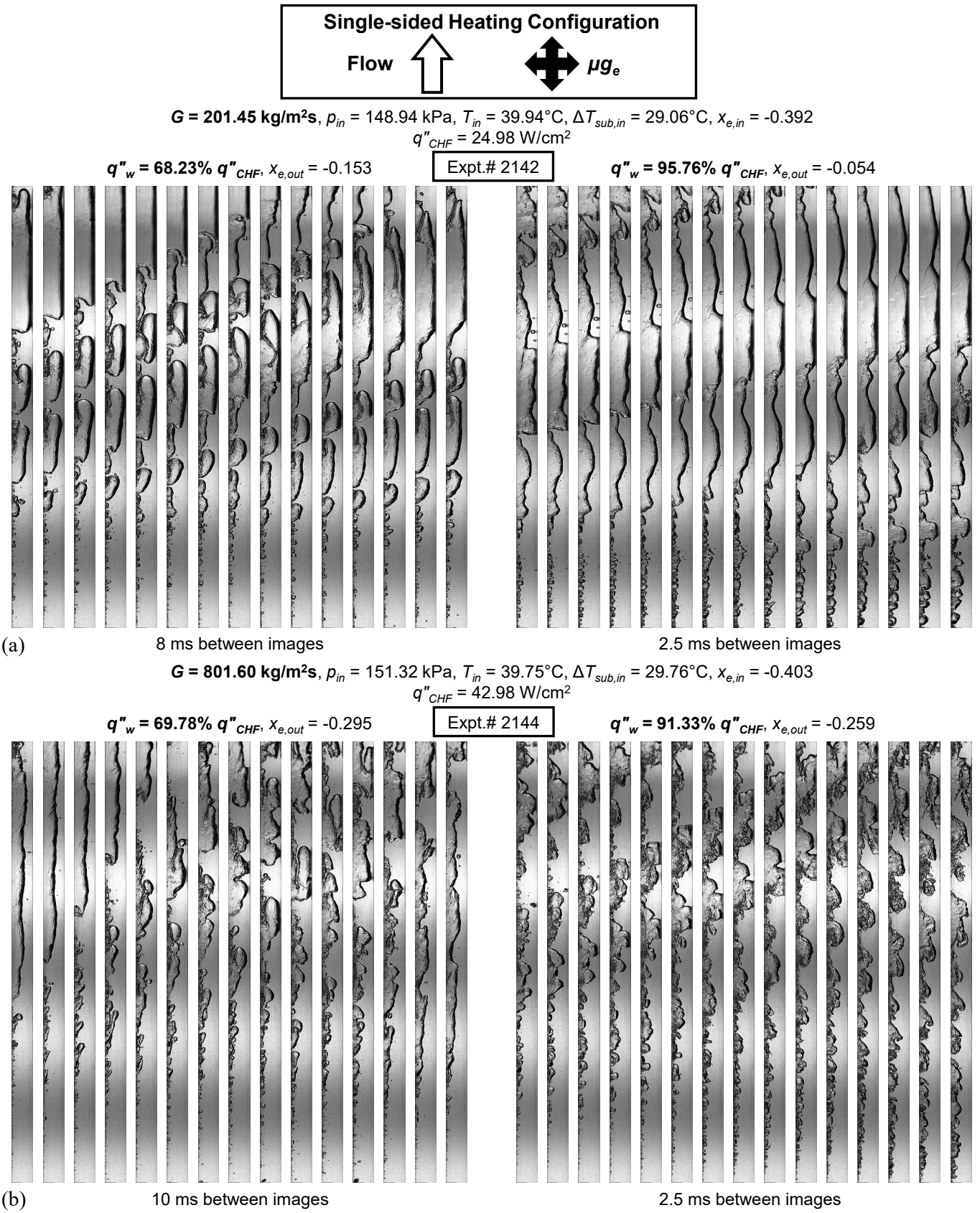

Fig. 17 Flow visualization image sequences for mass velocities of G = (a) 201.45, (b) 801.60, and (c) 2399.97 kg/m²s, at fixed inlet subcooling and inlet pressure with single-sided heating. Time interval between successive images is mentioned below each sequence.

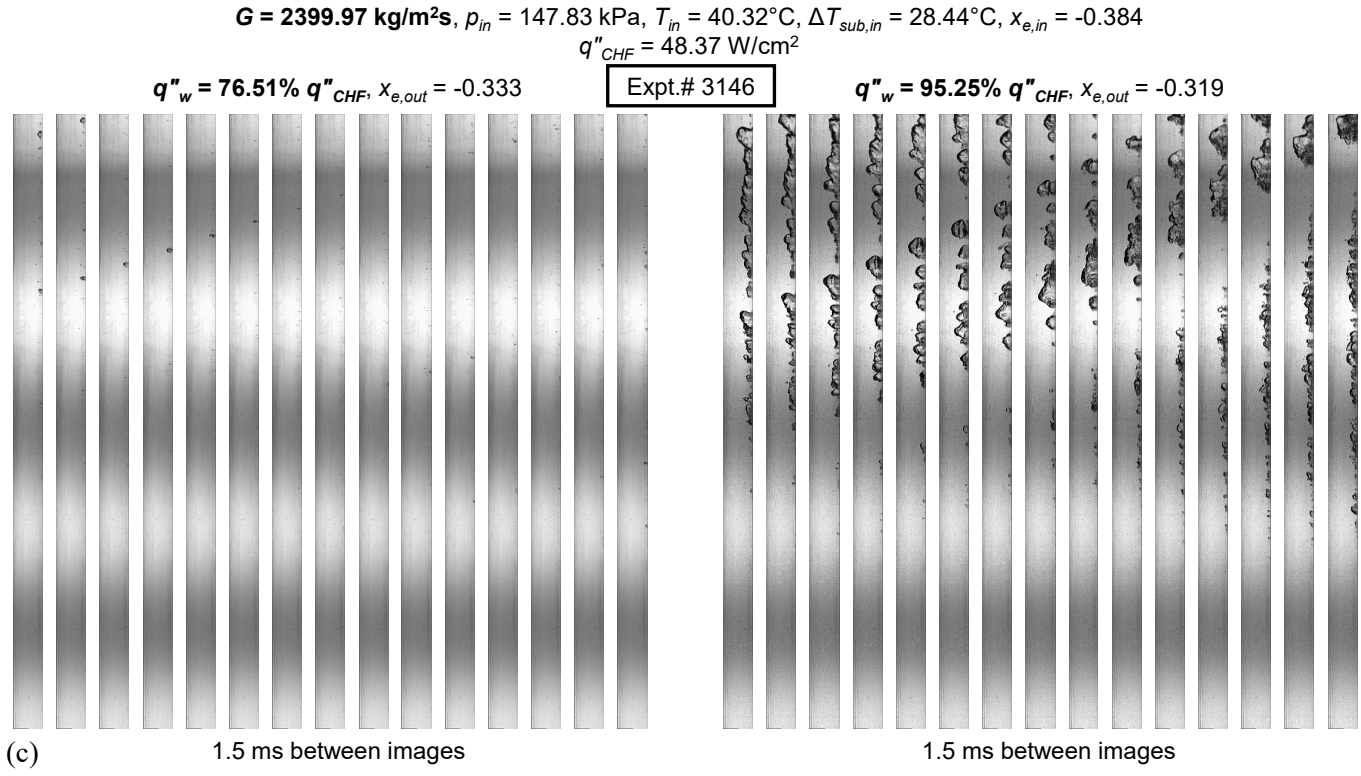

Fig. 17 (continued)

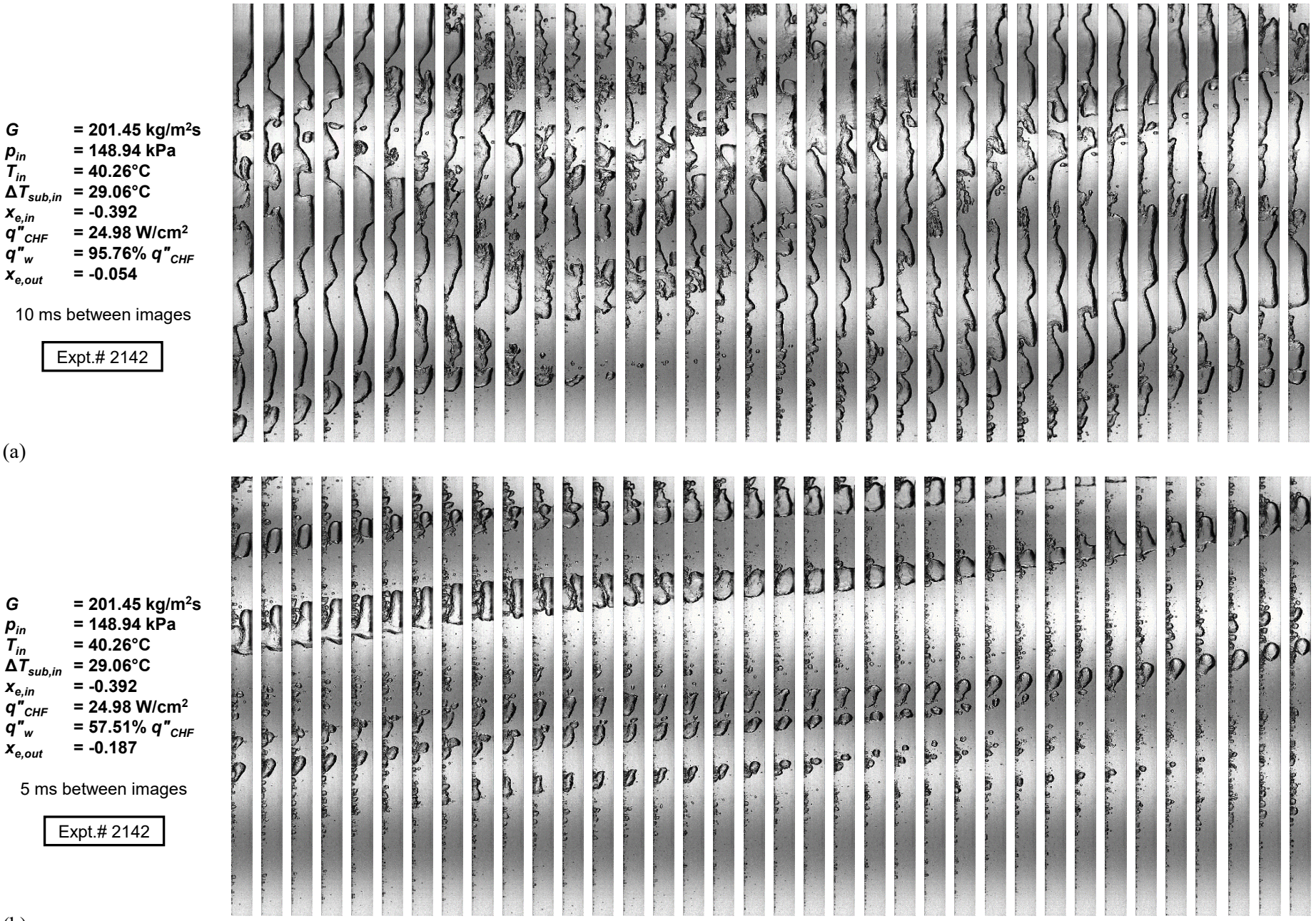

Fig. 18 Flow visualization image sequences for highly subcooled inlet with single-sided heating at mass velocity and heat flux combinations of (a) $G = 201.45$ kg/m^{2}s and $q''_w = 95.76\%\ q''_{CHF}$, (b) $G = 201.45$ kg/m^{2}s and $q''_w = 57.51\%\ q''_{CHF}$, and (c) $G = 1599.92$ kg/m^{2}s and $q''_w = 95.88\%\ q''_{CHF}$. Time interval between successive images is mentioned.

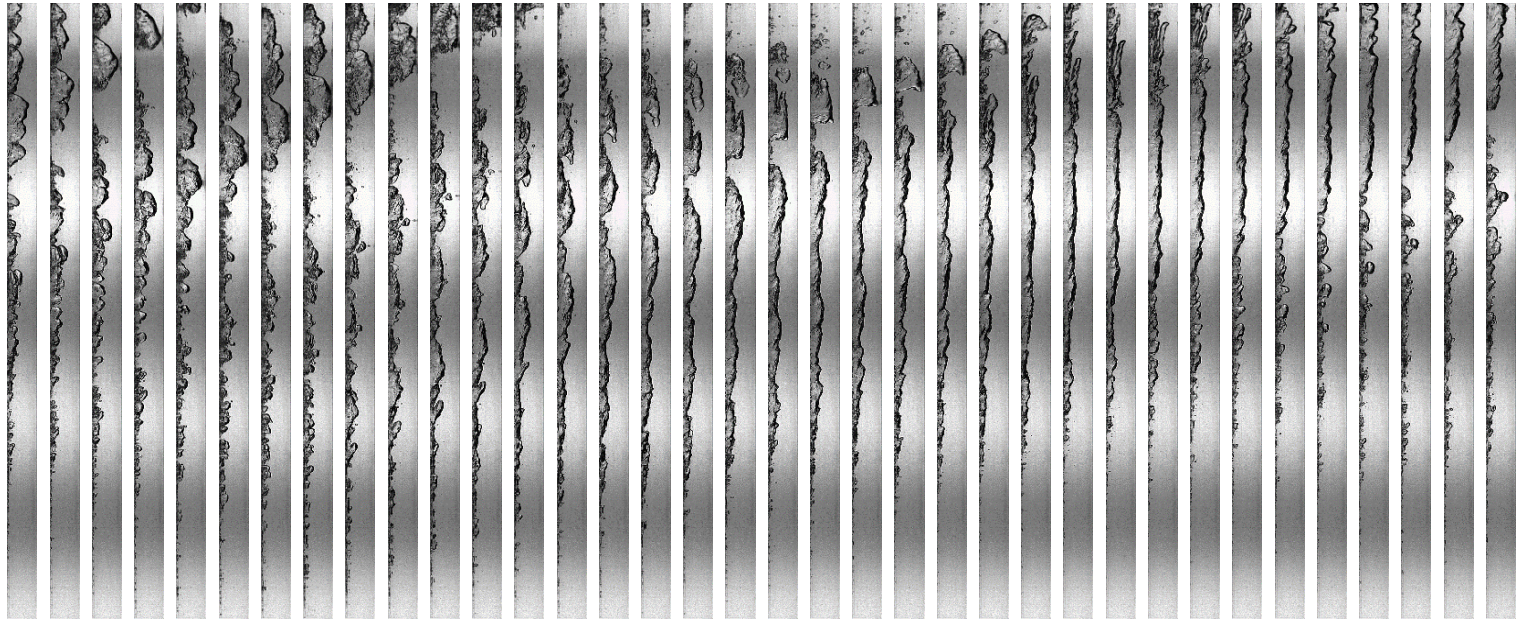

(c)

Fig. 18 (continued)

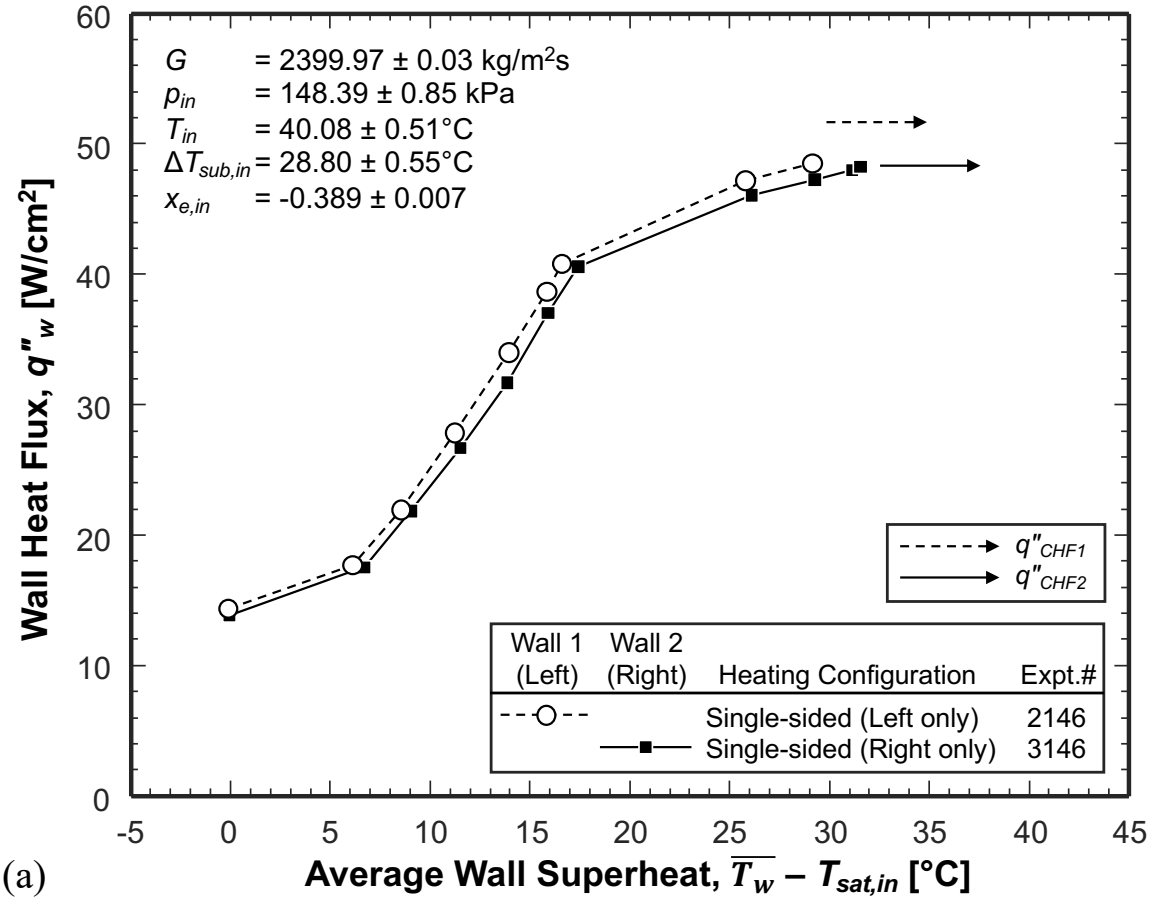

(a)

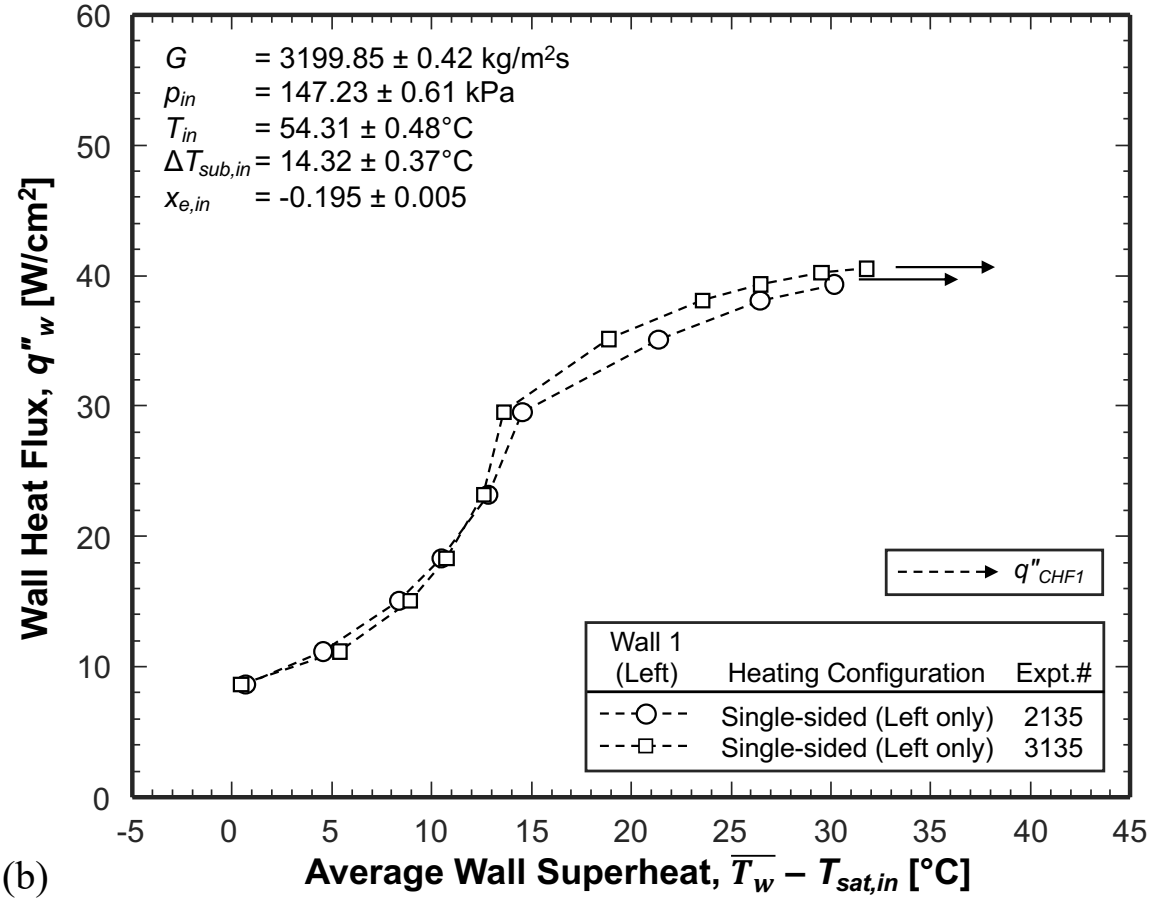

(b)

Fig. 19 Boiling curves illustrating (a) the symmetry in boiling heat transfer at the two walls for single-sided heating at identical operating conditions and (b) repeatability of experiments.

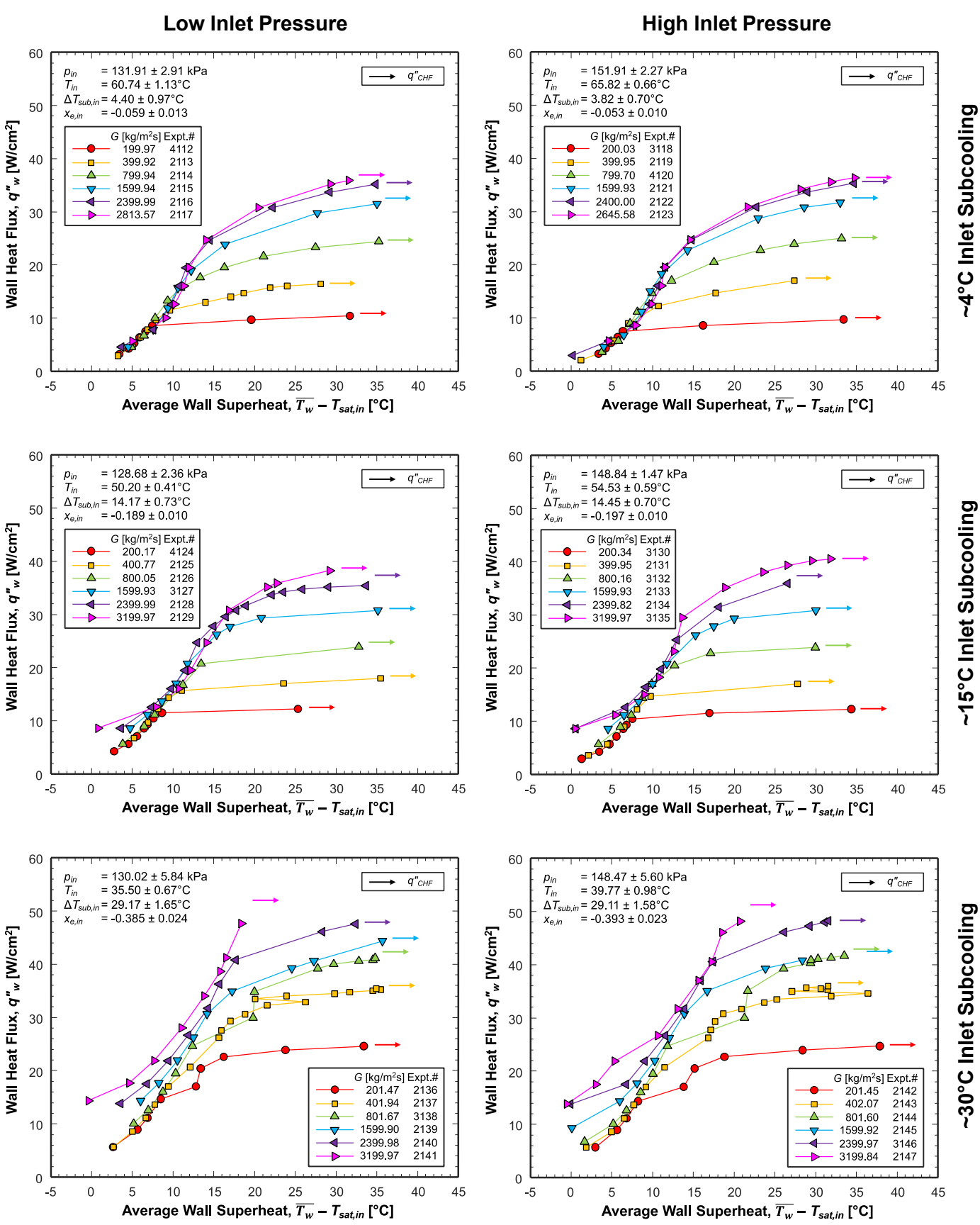

Fig. 20 Boiling curves illustrating mass velocity effects for different combinations of inlet pressures (low and high) and inlet subcoolings (4°C, 15°C, and 30°C).

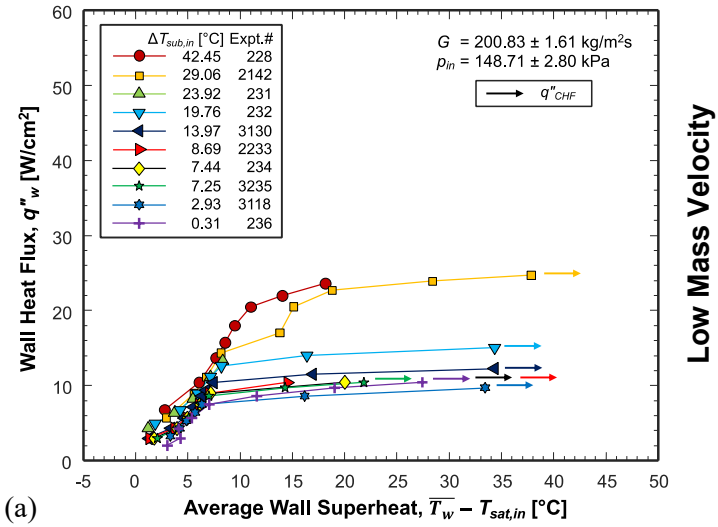

(a)

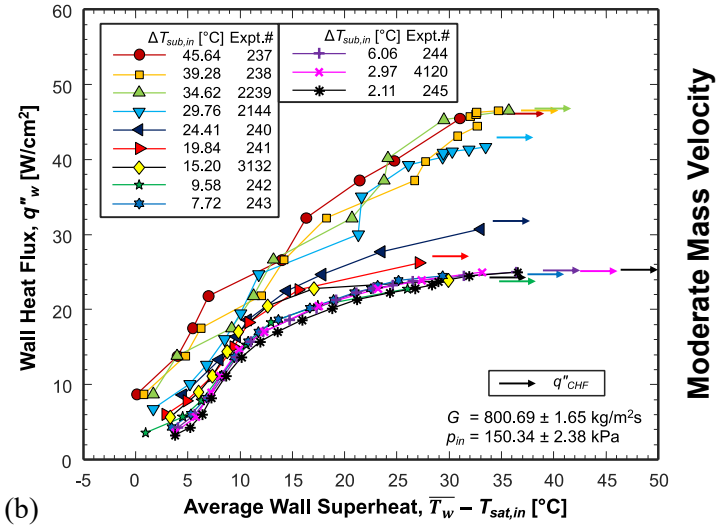

(b)

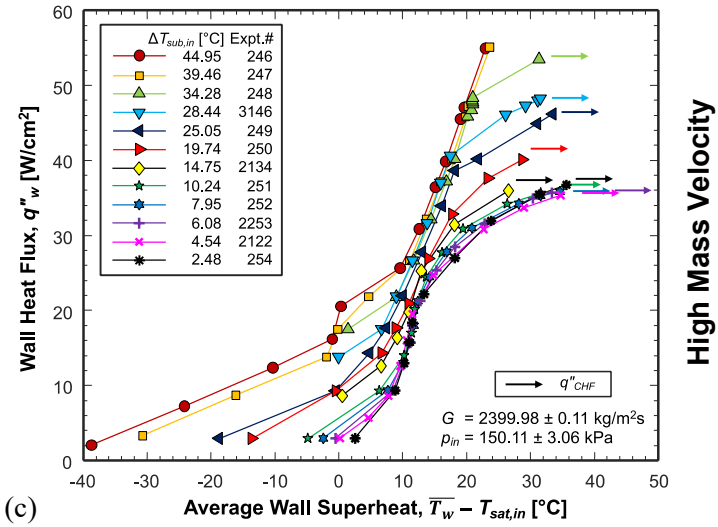

(c)

Fig. 21 Boiling curves illustrating inlet subcooling effects for different mass velocities of G = (a) 200.83, (b) 800.69, and (c) 2399.98 kg/m^{2}s.

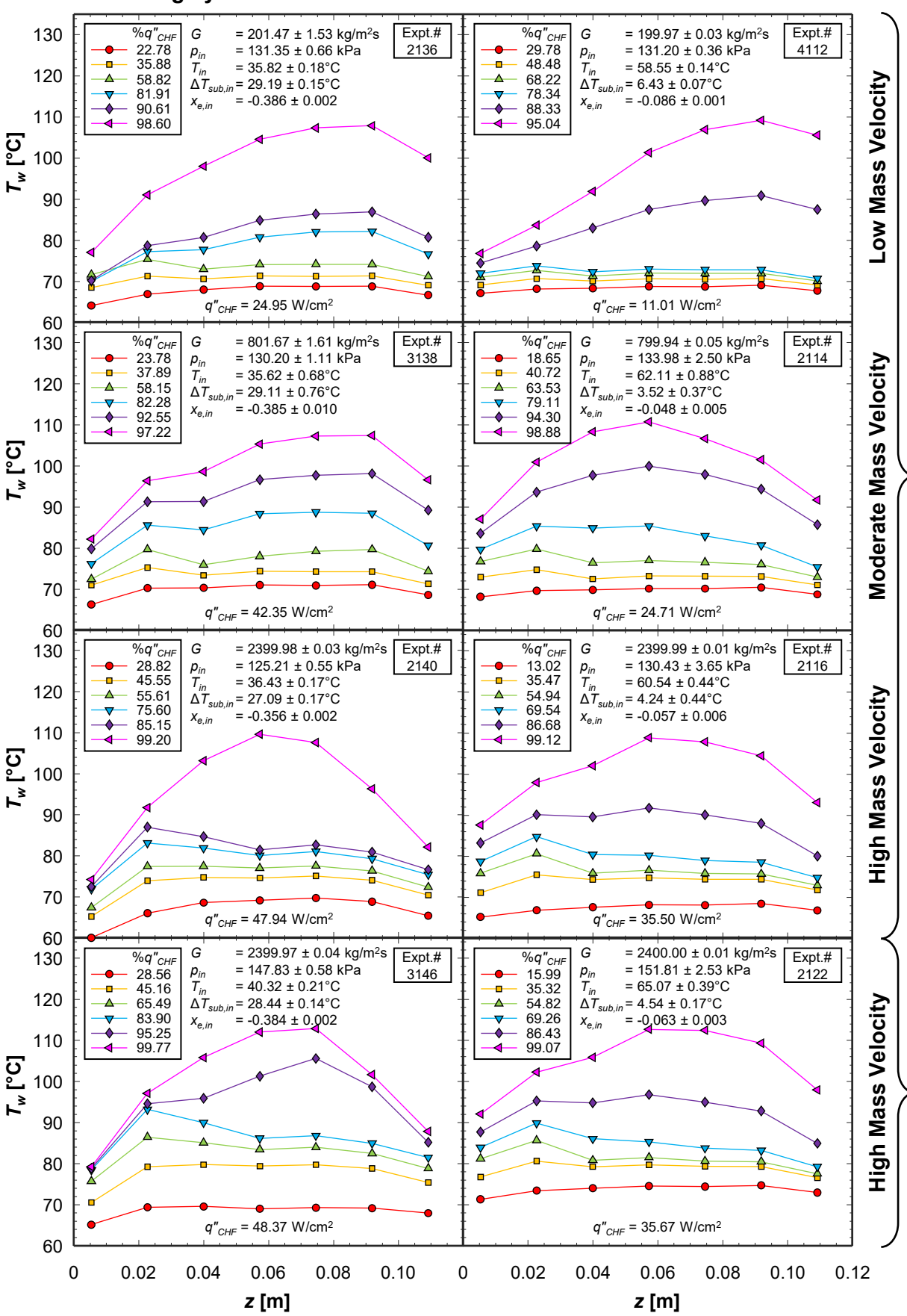

Fig. 22 Streamwise profiles of local wall temperature for different heat fluxes at a variety of operating conditions with single-sided heating.

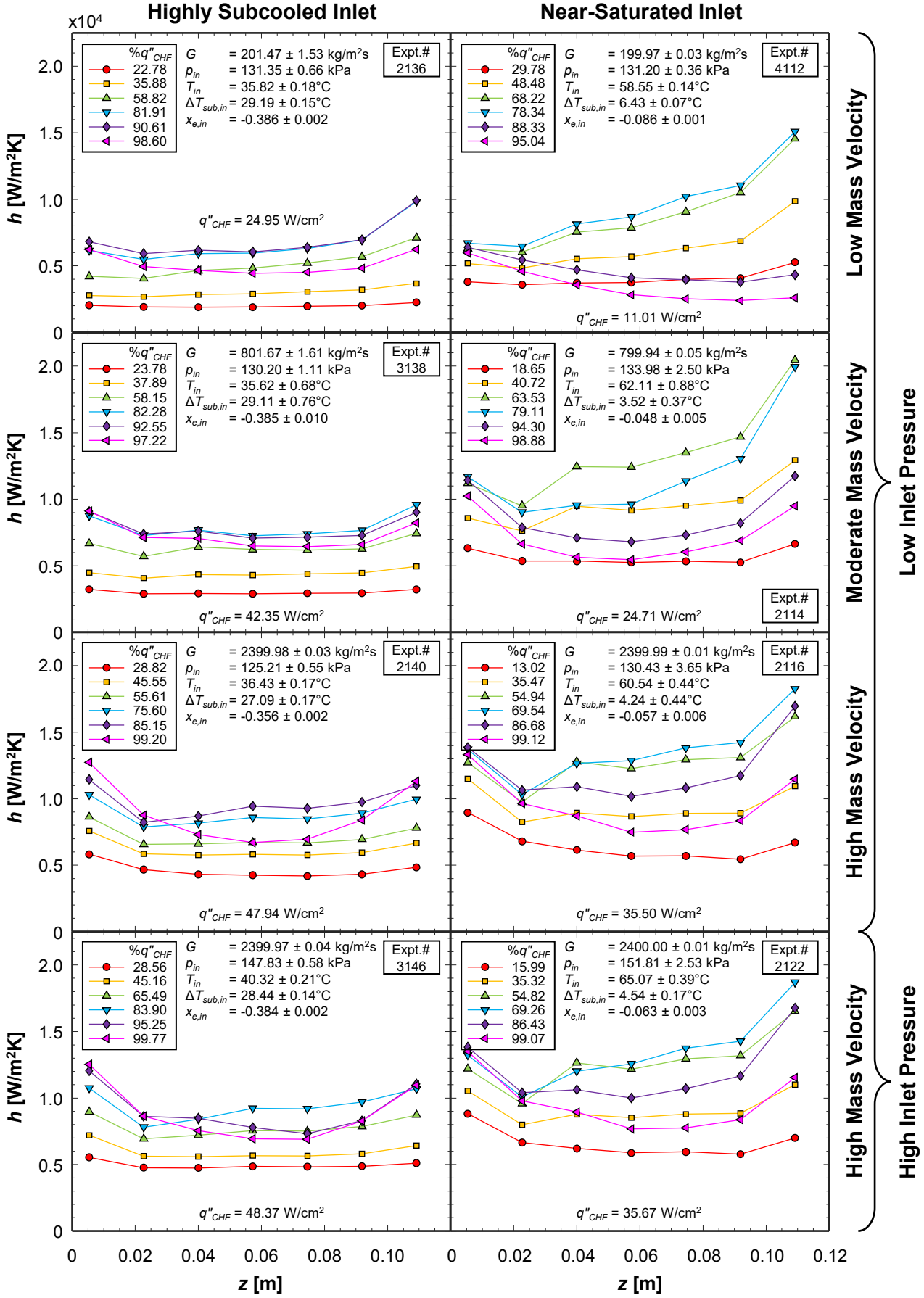

Fig. 23 Streamwise profiles of local heat transfer coefficient for different heat fluxes at a variety of operating conditions with single-sided heating.

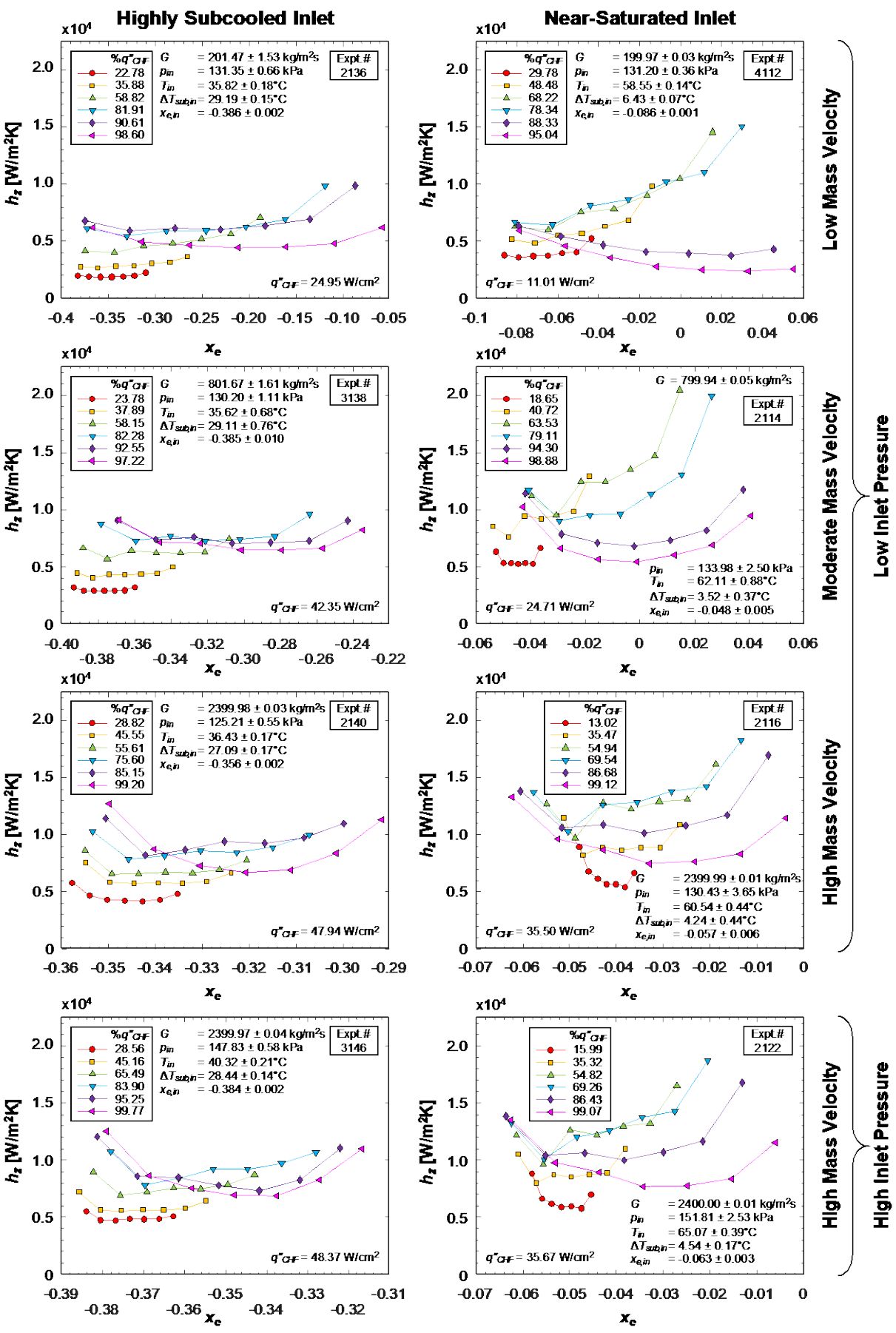

Fig. 24 Variations of local heat transfer coefficient with local thermodynamic equilibrium quality for different heat fluxes at a variety of operating conditions with single-sided heating.

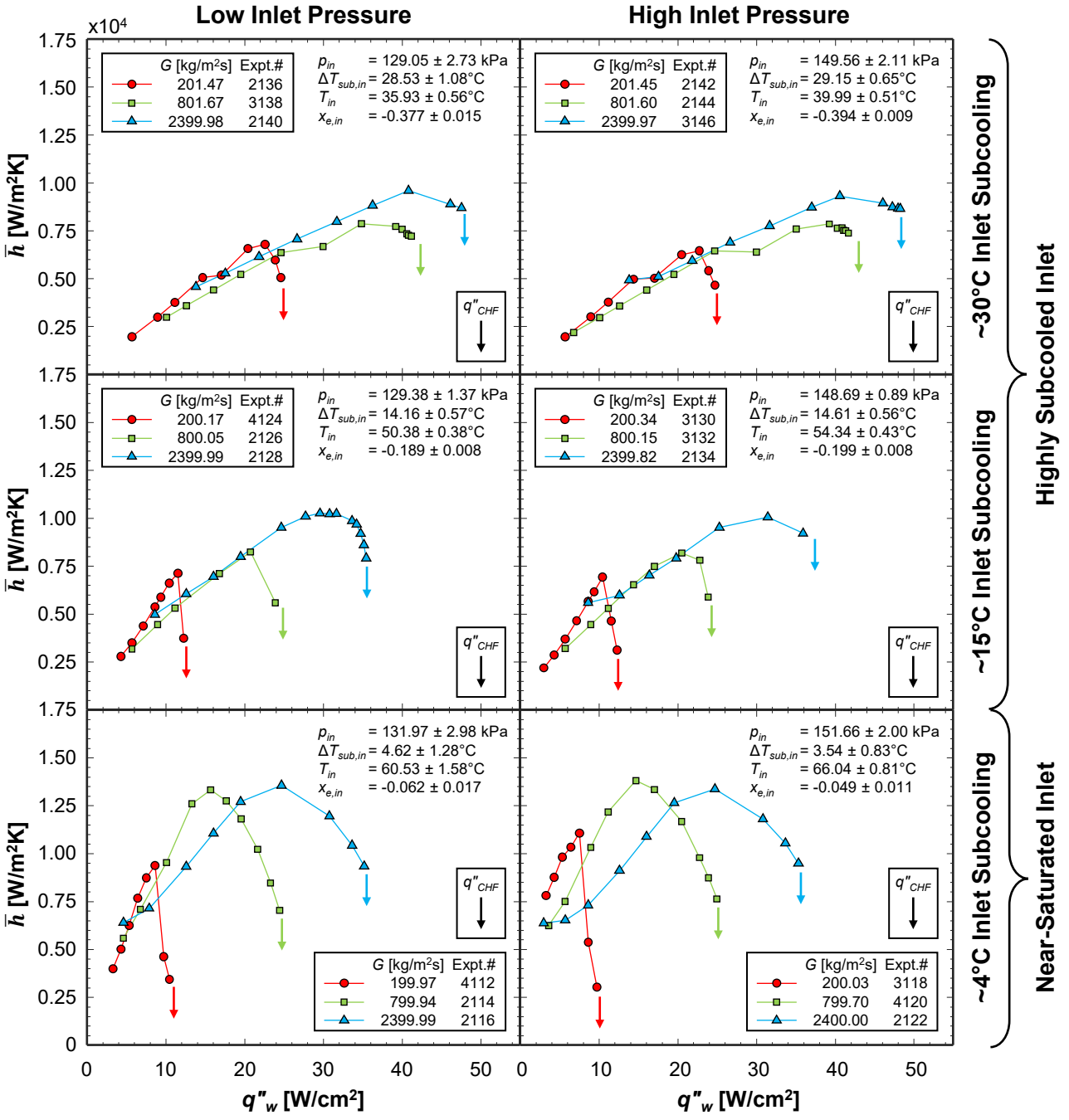

Fig. 25 Variations of average heat transfer coefficient with wall heat flux for three mass velocities at six different inlet conditions (three inlet subcoolings × two inlet pressures).